DEVELOPMENT OF MULTISCALE AND MULTIDIMENSIONAL LIGHT SHEET MICROSCOPY FOR IMAGE-BASED MODELLING OF ORGANOGENESIS

By

Tanveer Teranikar

Submitted in partial fulfillment of the requirements.

for the degree of Doctor of Philosophy at

The University of Texas at Arlington

December 2023

Supervising Professor, Dr. Juhyun Lee

Dr. Cheng-Jen Chuong,

Dr. Khosrow Behbehani,

Dr. Baohong Yuan

ABSTRACT

Behavioral analysis of individual cells, in the form of structural phenotypes arising in response to mechanical stimuli or genomic alterations as small molecule intermediates of disease, are instrumental for understanding organogenesis. In this regard, dynamic cell tracking or temporal changes in cell shape, area and size are vital for modelling tissue interactions. However, optical diffraction limits imposed by lenses, hinders high resolution volume reconstruction of microscale biological processes and subcellular organelles. Thereby, isotropic intensity is restricted to limited focal volumes, reducing imaging distance to less than 1 mm for high magnification.

To combat this, Light Sheet Microscopes (LSM) have emerged as powerful optical sectioning tools, owing to millisecond camera frame rates and individual cell localization for imaging distances beyond 1 mm. However, current LSM resolution and imaging distance are highly dependent on the numerical aperture (NA)/magnification of the objective lens. In AIM 1, we achieved near isotropic, micron-scale 3D resolution across tunable imaging distance (up to 7mm) using a very low magnification (2x), to decouple fundamental relationship of lens NA on resolution and imaging distance. Using a 1x macro detection lens with 2x optical zoom, we refocused 120 micron long optical section across 6500 micrometer distance, in synchrony with modulation of active camera pixels. Further, a 3d pixel resolution algorithm was used to enhance voxel resolution ~3x in lateral perspective and ~5x in axial perspective. Consequently, we quantified 2.5 micrometer resolution in XY plane and 3.65 microns in XZ plane, from native resolution of 8.2 +/ 0.8

micron in XY plane and axial resolution of 17.25 +/-1.75 micron in XZ plane. AS-sLSM was used to reconstruct micro-structures in optically cleared whole mice organs.

With regards to multi-dimensional imaging in live animal models, LSM in conjunction with optically transparent zebrafish, has advanced the frontiers of *in vivo* characterization of evolutionarily conserved developmental signaling pathways. Hence, we have developed a multidimensional (3D, 3D+time) LSM in AIM 2, capable of tunable imaging distance up to 1 millimeter, to characterize organogenesis in smaller animal models at cellular scale. Like AIM 1, we sought to remove dependance of lens NA on resolution and field-of-view for 3D imaging, and hence integrated oblique angle-based sample detection for 3D imaging to apply sub voxel, resolution enhancement algorithm. We successfully quantified isotropic 3D pixel resolution of 2 microns +/- 0.3 microns in the XY plane and 2.5 microns +/- 0.4 microns in the XZ plane using 4X magnification lens, for optical section of 500 micrometer propagation distance. For 4D imaging in AIM 2, traditional orthogonal sample detection was integrated with *in silico* volume reconstruction algorithm. We quantified XY resolution of 4.25 +/ 0.7 microns and YZ resolution of 9.75 +/ 1.1 microns using 4x magnification lens for optical section of 500-micron propagation length, using single side illumination for 4D mode. Using the 4D imaging pipeline, we reconstructed zebrafish myocardial nuclei (~5-15 microns) across distinct stages of heart maturation. In addition, a feature detector based on Difference of Gaussian (DoG) filter integrated with watershed algorithm, was implemented to localize individual nuclei.

AIM 3 is a continuation of AIM 2, wherein we have applied our multi-dimensional LSM to quantify regional anisotropy in zebrafish ventricular nuclei mechanical deformation and morphogenesis. Hessian Difference of Gaussian (HDoG) feature detector from AIM 2 was used to localize and quantify 159 ± 13, 222 ± 17, 260 ± 13, and 284 ± 10 nuclei across 48-120 hours post birth stages respectively. Furthermore, we observed nuclei surface areas ranging from 29 +/- 9 um^2 – 47.45 +/-10 um^2 for spherical nuclei near inflow, in contrast to larger rod-shaped nuclei ranging from 28 +/- 15 um^2 – 57.25 +/- 25 um^2 in the equatorial region near ventricular inflow across 48 – 120 hours post birth. In addition, we quantified dynamic mechanical deformation experienced by individual nuclei across the cardiac cycle, by tracking segmented nuclei centers of mass to calculate area ratio. In this regard, we did not observe any significant differences in deformation across different ventricular regions across 48-120 hours post birth, between the inflow, equatorial and apex regions. Lastly, three-dimensionsional ventricular lumen segmented by HDoG feature detector was used to train a neural net based on semantic segmentation, to automate zebrafish ventricular volume quantification.

Consequently, our studies demonstrate the potential of LSM as a user-friendly, multidimensional (3D,3D+time) imaging toolbox, for *in vivo* reconstruction of cellular phenotypes, across diverse spectrum of preclinical biological specimens.

ACKNOWLEDGEMENTS

"Success is not final; failure is not fatal: It is the courage to continue that counts." – Winston Churchill.

At the culmination of this academic endeavor, I am humbled and deeply grateful to acknowledge the invaluable contributions and unwavering support of numerous individuals who have guided, encouraged, and inspired me throughout this journey.

I am profoundly indebted to my supervising professor, Dr Juhyun Lee for his visionary guidance that provided the compass for this academic odyssey. Dr Lee not only instilled a sense of purpose but also illuminated the path forward, infusing every phase of this research with clarity and direction. I will always be thankful for his faith in me.

The collaborative spirit and dedication of my fellow lab members have been the bedrock of this research endeavor. I extend my deepest gratitude to each member of the Lee lab group for their tireless efforts and shared enthusiasm in navigating the challenges and triumphs of our collective pursuit. I want to thank my senior lab members Dr. Victoria Messerschmidt, Dr. Zachary Bailey, and Dr. Nabid Salehin, whose expertise, camaraderie, and willingness to share insights greatly enriched the tapestry of ideas within our laboratory. Special thanks to Jessica Lim, Toluwani Ijaseun, Cynthia Dominguez and Amina Agbonoga for helping me with organ preparation and optical tissue clearing. Their collective contributions and support significantly shaped the trajectory of Chapter 1. Further, I extend my sincere gratitude to Dr. Reto Fiolka and Dr. Bo-Jui Chang at UT Southwestern for conceptualization and design of the Axially Sweeping Light Sheet

Microscope hardware and firmware. Chapter 1 would have been very difficult, if not impossible without Dr Fiolka and Dr Chang's technical mentorship. Phuc Nguyen collaborated with me in the design and 3D printing of custom sample holders and rigid parts that enable sample mounting across Chapters 1-3, and I owe him my deepest gratitude for his time and enthusiasm. Further, I am indebted to Adam Germaine and Dr. Young Tae-Kim for letting me use their 3D printing facilities. In addition, I must extend my heartfelt thanks to Dr. Salehin, Kristofer Pas, Cameron Villareal and Dr. Cheng- Jen Chuong for their intellect, guidance, and commitment in our shared pursuit of zebrafish biomechanical quantification in Chapter 3. Moreover, Bohan Zhang and Shi-Yuh Pan have been instrumental in laying the groundwork for U-net and neural net protocols, thereby expanding the scope of our lab research.

Lastly, I owe immense gratitude to my mother, grandparents, girlfriend and close friends for their support and patience during the very demanding PhD timelines, as they have been my constant source of comfort and motivation. I am also very grateful to my committee members Dr. Cheng Jen-Chuong, Dr. Khosrow Behbehani and Dr. Baohong Yuan for their meticulous attention to detail and guidance through this document's review process. Their collective insights have greatly enriched the quality of research presented in the thesis.

TABLE OF CONTENTS

Abstract ……i

Acknowledgements ……iv

Chapter 1: ……1

1.1 Introduction ……1

1.2 Specific Aims ……4

1.3 Organization of thesis ……8

Chapter 2: ……9

2.1 Introduction ……10

2.2 Light Sheet Microscope specifications ……11

2.3 Methods ……12

2.3.1 Axially sweeping light sheet microscope construction ……12

2.3.2 Rolling shutter camera pixel gating……15

2.3.3 Sub voxel off-axis volumetric reconstruction ……16

2.3.4 Tissue clearing protocol for autofluorescence imaging ……21

2.3.5 Resolution quantification and statistical analysis ……24

2.4 Results ……25

2.4.1 Instrument characterization for conventional light sheet microscopy and axially sweeping light sheet modes ……25

2.4.2 Tunable Pixel resolution enhancement across tunable millimeter field-of-view ……28

2.4.3 Volume reconstruction of benzyl benzoate cleared whole mouse kidney using axially sweeping light sheet mode ……30

2.4.4 Volume reconstruction of benzyl benzoate cleared whole mouse lung using axially sweeping light sheet mode ……31

2.5 Discussion ……34

2.5.1 Significance of study ……34

2.5.2 Limitations of study ……35

2.6 Supplementary Figures ……36

Chapter 3 : ……37

3.1 Methods ……38

3.1.1 Implementation of Single/dual illumination light sheet mode ……38

3.1.2 Voxel super resolution algorithm ……39

3.2 Results ……40

3.2.1 Instrument implementation for single and dual illumination light sheet modes ……40

3.2.2 Instrument characterization for single and dual illumination light sheet modes ……42

3.2.3 Pixel improvement using Sub voxel light sheet algorithm 45

3.3 Discussion 46

3.3.1 Significance of study 56

3.4 Supplementary Figures 47

Chapter 4 : 48

4.1Introduction 49

4.2Methods 51

4.2.1 Preparation of zebrafish for imaging 51

4.2.2 Image processing pipeline 52

4.3 Results 57

4.3.1 Anisotropic illumination correction by integrating dehazing algorithm and background subtraction 57

4.3.2 Application of isotropic structuring elements to resolve edge features 59

4.3.3 Evaluation parameter of image restoration 59

4.4 Discussion 61

4.4.1 Significance 61

4.4.2 Conclusion and limitations of study 65

4.5 Supplementary figures 66

Chapter 5: ……68

5.1 Introduction ……69

5.2 Methods ……72

5.2.1 Multidimensional Light sheet microscope implementation ……72

5.2.2 Preparation of zebrafish for assessing cardiac function ……73

5.2.3 Image processing framework ……75

5.2.4 Cell tracking framework ……76

5.2.5 Statistical treatment ……76

5.3 Results ……78

5.3.1 Application of Hessian Difference of Gaussian to segment cardiomyocyte nuclei ……78

5.3.2 Nuclei counting to assess embryonic zebrafish heart maturation and segmentation accuracy evaluation ……80

5.4 Discussion ……82

5.4.1 Significance of study ……82

5.5 Supplementary figures ……84

Chapter 6: ……87

6.1 Introduction ……88

6.2 Methods ……90

6.2.1 Preparation of zebrafish for imaging ……90

6.2.2 Implementation of multidimensional light sheet setup ……91

6.2.3 Contractility methodology ……91

6.2.4 Statistical testing ……93

6.2.5 Neural net architecture ……94

6.3 Results ……95

6.3.1 Isolating individual cardiomyocyte nuclei in dynamic zebrafish ventricular volumes ……95

6.3.2 Quantification of local deformation via tracking cardiomyocyte nuclei ……97

6.3.3 Quantification of zebrafish ventricular nuclei morphogenesis across distinct developmental stages ……98

6.3.4 Application of hessian feature detector as ground truth segmentation pipeline for neural net training ……100

6.4 Discussion ……103

6.5 Supplementary Figures ……104

Chapter 7 ……105

7.1Conclusions ……106

7.2 Potential research topics for future studies ……109

References ……110

LIST OF FIGURES

Figure 2.1 Light sheet beam profile characteristics ……11

Figure 2.2 Axially sweeping microscope schematic. ……14

Figure 2.3 Axially sweeping microscope construction. ……16

Figure 2.4 Maximum Likelihood Estimation pixel resolution improvement pipeline ……17

Figure 2.5 Non-rolling shutter field-of-view pixel resolution ……25

Figure 2.6 Rolling shutter field-of-view pixel resolution ……27

Figure 2.7 Axially sweeping Sub voxel light sheet mode resolution ……28

Figure 2.8 Volume reconstruction of benzyl benzoate cleared auto fluorescent mouse kidney…31

Figure 2.9 Volume reconstruction of micro structures in benzyl benzoate cleated auto fluorescent mouse lungs ……33

Figure 2.10 Volume reconstruction of macro structures in benzyl benzoate cleared auto fluorescent mouse lungs ……33

Figure S1 Orthogonal perspectives of benzyl benzoate cleated auto fluorescent mouse kidney ..36

Figure 3.1 Single/dual side illumination Light sheet microscope ……41

Figure 3.2 Single side illumination light sheet spatial resolution ……42

Figure 3.3 Dual illumination light sheet spatial resolution ……44

Figure Sub voxel light sheet spatial resolution vs dual illumination light sheet mode ……45

Figure S3.1 Subvoxel light sheet model using different lens NA ……47

Figure 4.1 Image processing algorithm ……52

Figure 4.2 Image enhancement results for attenuated light sheet images ……58

Figure 4.3 Image restoration evaluation ……60

Figure S4.1 Restoring contrast uniformity in zebrafish trunk vasculature ……66

Figure S4.2 Peak signal-to-noise ratio evaluation ……67

Figure 5.1 Hessian Difference of Gaussian scale space feature detection in combination with watershed algorithm ……79

Figure 5.2 Segmentation accuracy evaluation ……81

Figure S5.1 Volume overlay of raw nuclei with segmented nuclei volumes ……84

Figure S5.2 Visualizing zebrafish ventricular myocardial nuclei deformation across the cardiac cycle ……85

Figure S5.3 Nuclei counting across embryonic zebrafish heart maturation stages ……86

Figure 6.1 Snapshot of MATLAB 4D nuclei tracking algorithm ……93

Figure 6.2 Applying scale space feature detector for isolating fused nuclei morphology ……96

Figure 6.3 Area ratio index calculated by tracking 4D nuclei motion ……97

Figure 6.4 Nuclei surface area quantification ……99

Figure 6.5 Automated three-dimensional volume segmentation using U-net ……100

Figure 6.6 Neural net segmentation accuracy evaluation ……102

Figure S6.1 Visualizing spatiotemporal dynamics of myocardial cardiomyocyte nuclei ……104

CHAPTER 1

1.1 INTRODUCTION

Traditional wide-field microscopes illuminating entire samples are adversely affected by out-of-focus light scatter, thereby hindering analysis of thick biological specimens[1], [2]. Moreover, commercial upright or inverted microscopes are inherently unable to acquire 3D/3D + time volumes and require retrofitting with proprietary optics or machine learning algorithms to perform optical sectioning[3]–[6].

Owing to the recent advent of electro-mechanics, user configurable optical sectioning microscopy (OSM) analogous to physical tissue sections, has enabled non- invasive reconstruction of dynamic volumes with high fidelity[7], [8]. In this regard, Light sheet microscopy (LSM) has emerged a very prominent OSM due to numerous desirable qualities; intrinsic autofluorescence rejection due to orthographic 1D planar illumination, non – ionizing nature, non-invasive genotypic or phenotypic biomarker screening and ability to image a plethora of animal models[9]–[13].

More importantly, LSM is capable of multi-dimensional (4D, 3D + time) and multi-scale reconstruction of cells and whole organs[7], [14]–[19]. This is due to ability to image with large working distance (millimeter) lenses and ability to tune sectioning thickness from less than one micron to several microns(>15um)[3]. Notably, LSM does not suffer from poor framerates, photobleaching or limitations with respect to sample perspectives, as observed for live imaging in very popular confocal microscopy or other OSM.

Furthermore, LSM is compatible with varying fluorescent labelling techniques in optically cleared whole organs for *in toto* imaging or *in vivo* transgenic animal models such as zebrafish (Danio rero)[9], [10], [20]–[22].

However, currently LSM resolution depends on the excitation objective lens (OL) numerical aperture (NA). Hence, a puzzling conundrum of choosing an appropriate NA without sacrificing spatial resolution and imaging field-of-view (FOV) is often encountered[2], [3], [17], [18], [23]. Using very high NA excitation optics provides near single micron optical sectioning capability. However, higher NA tends to reduce the imaging FOV to only couple of microns (<500 microns)[3].

Recently, remote refocusing based axially sweeping light sheet microscopy (ASLSM), provides promising avenues for decoupling dependance of NA on resolution, by axially displaced light sheet focus using mechanical remote focusing actuators[17]. A rolling shutter (RS) camera pixel approach is utilized, by modulating an offset in activation of camera pixel sensor array to capture the refocused light section. Thereby enabling arbitrary FOV modulation, while maintaining micron scale resolution. However, current AS-LSM is also reliant on high NA detection optics for single micron resolution[11], [17], thereby intrinsically suffering from low penetration depth and limiting modulation of light sheet thickness. Therefore, deep tissue imaging of cellular scale biological phenomena in centimeter scale mice organs or porcine tissue, remains a challenging task for RS-based ASLSM.

To address these unmet limitations, this thesis illustrates the development of a new generation of AS-LSM utilizing maximum likelihood estimation (MLE) based sub voxel LSM (SLSM)[24], [25]. SLSM enables *in silico* resolution enhancement via tilted optical sectioning at nanoscale incremental steps. The algorithm models a super – resolved image estimate from multiple, spatially correlated sub stacks that have resolution consistent with system point spread function (PSF)[3], [24]. Sub- stacks are obtained by periodic resampling of raw oblique scanned stack containing three-dimensional sub-voxel shifts, at voxel sizes (3D pixel) one-third of the light sheet thickness[24]. Using axially sweeping, sub voxel LSM (AS-sLSM), we have achieved cellular resolution across tunable 6.5-millimeter field-of-view, using very low magnification (2x) lens.

With respect to high penetration depth (>1-1.5mm) multidimensional imaging, LSM has enabled *in vivo* characterization of image-based signaling pathway modelling and tissue morphogenesis, in smaller animal models such as zebrafish, with high fidelity[8], [10]. In this regard, zebrafish are rapidly emerging as popular translational models for studying developmental disease progression[10]. This is due to genetic tractability with mammals and versatile gene editing tools, enabling the creation of stable zebrafish generations[9], [26]–[28]. More importantly, zebrafish offer unique advantages like high breeding capacity and embryonic transparency, allowing for high-resolution, real-time imaging using LSM[10]. In this regard, we have successfully developed an *in vivo, 4*D (3D+time) light sheet microscope, capable of individual cell tracking at milli-second camera frame rates, for imaging field-of-view up to one millimeter[7], [14], [15].

1.2 SPECIFIC AIMS

AIM 1. Development and application of 3D light sheet microscope capable of millimeter-centimeter imaging field-of-view and micron scale spatial resolution

STUDY 1.1 We have developed a novel LSM by integrating axially sweeping LSM and sub voxel LSM, to enable arbitrary field-of-view modulation and native pixel resolution enhancement. In this study, we used a 0.2 NA/2X detection with 493 nm wavelength excitation, to quantify theoretical lateral resolution of 2.2 micrometer and axial resolution of 3 micrometers, in addition to theoretical light sheet propagation distance of 120 micrometers. We achieved practical resolution of 8.2 micron and 17.25 micron in XY and YZ planes respectively by imaging 1 micrometer beads, across 120 micrometers distance. Using axially sweeping LSM we extended light section propagation distance ~50x from original 120 micron to 6.5-millimeter, with no significant loss in pixel resolution between both original and extended field-of-view. Further, after integration of sub voxel algorithm with remote refocus light sheet microscopy, we were able to achieve statistically significant reduction of ~3x in lateral resolution and ~5x in axial resolution. Consequently, we achieved near isotropic pixel resolution of 2.5 micron in XY plane and 3.65 microns in XZ plane, using a very low NA detection objective. Furthermore, AS-sLSM was used to reconstruct autofluorescence of optically cleared benzyl benzoate mice kidneys and lungs at cellular scale.

AIM 2. Development of 3D/3D+time light sheet pipeline capable of localizing and tracking individual cells in embryonic zebrafish

STUDY 2.1 In this section, we performed quantitative testing of pixel resolution for light sheet modalities capable of cellular scale image analysis for small animal specimens (600 micron-3mm), such as single side illumination LSM, dual illumination LSM and sub voxel LSM (non-axially sweeping). Using 0.1 NA/4X detection lens with 493 nm excitation wavelength, we quantified theoretical lateral resolution of 1.6 micrometer and axial resolution of 6 micrometers, in addition to light section propagation confocal region of 500 micrometers. We obtained practical resolution of 4.25 micron and 9.75 micron in XY and YZ planes respectively using single side illumination LSM, by imaging 1 micrometer beads across 500-micron distance. Our results indicate statistically significant reduction of ~1.3x in axial resolution of dual illumination LSM with respect to single sided illumination, but no significant reduction in lateral resolution was observed between both. After performing sub voxel procedure using 4x objective, we were able to achieve statistically significant reduction of ~2x in native pixel XY resolution to achieve 2 microns in XY plane, and ~3.5x enhancement to achieve 2.5 microns in YZ pixel resolution. More importantly, we observed no significant difference between lateral and axial resolution across entire 500 micrometer confocal region after implementing sub voxel algorithm indicating isotropic volumetric resolution. We also compared the pixel resolution of 500 micrometer FOV achieved using 4x after pixel improvement, with sub voxel resolution across 4500 micrometer FOV in AIM 1 achieved using 2x detection objective. Our investigation did not find significant

difference in lateral resolution of 4x objective with 2x objective between both FOV's, thereby decoupling the effect of NA/magnification on resolution and FOV. However, we did observe significant difference in axial resolution between 500 micron and 4500-micron FOV achieved using 4x and 2x detection objective respectively, after pixel enhancement.

STUDY 2.2 Despite pixel resolution enhancement via sub voxel LSM, tissue birefringence produced anisotropic contrast causing haze/attenuation within imaging FOV. Hence, we have applied the dehazing algorithm based on dark channel prior (DCP) in conjunction with morphological image operations to restore isotropic contrast across region-of-interest. No significant changes in structural integrity of dehazed image and raw image were observed, using metrics such as structural similarity index and peak signal to noise ratio. 4 days post fertilization Tg(fli1:gfp) zebrafish expressing fli1 promoter-driven green fluorescent protein (GFP), was reconstructed in comparison to confocal microscope 3D reconstruction to visualize vascular endothelial and endocardial cells.

STUDY 2.3 In this study, we established 4D LSM imaging pipeline to track dynamic 3D cells, with milli-meter penetration depth detection lens and 300–600-micron FOV modulation. Single side setup without sub-voxel pixel enhancement was used to reconstruct 3D time lapses of ventricular myocardial nuclei in transgenic zebrafish line Tg(cmlc:GFPnuc). The transgenic line expresses cardiac myosin light chain promoter driven GFP in myocardium. Due to non-gated optical sectioning, *in silico* 4D synchronization algorithm was applied for rearranging ventricular volumes from systole to diastole. Furthermore, an automated feature detector was implemented based on hessian

difference of gaussian (HDoG) in combination with watershed algorithm, to localize individual myocardial nuclei. No significant reduction in nuclei count was observed between segmented nuclei and manually counted nuclei. Utilizing the segmented nuclei, we successfully quantified significant changes in ventricular myocardial nuclei count and 3D nuclei area changes across the cardiac cycle, from 2 – 5 days post birth.

AIM 3: Application of 4D LSM imaging pipeline, for cell counting and mechanotransducive cardiovascular phenotypes in embryonic zebrafish.

STUDY 3.1 This study is a continuation of AIM 2, where we utilize previously established 4D LSM imaging pipeline capable of cellular resolution at millisecond frame rates, to quantify cardiovascular phenotypes in zebrafish preclinical model. Using a transgenic (cmlc:GFPnuc) zebrafish line with green fluorescent protein expressed in myocardial cardiomyocyte nuclei, we were able to show significant differences in surface areas of nuclei distributed across varying parts of the ventricular morphology. Further, we applied HDoG feature detector to localize and track nuclei across time axis, to quantify ventricular myocardial mechanical deformation across entire cardiac cycle. In addition, the feature detector was used to segment ventricular lumen of transgenic (cmlc:GFP) zebrafish, to train a neural net (nnU-net) and thereby implement an automated semantic segmentation pipeline. Using multidimensional volumes produced by neural net, we successfully quantified zebrafish ventricular volume across the cardiac cycle. Consequently, we were able to validate embryonic zebrafish in conjunction with multidimensional LSM, as a preclinical toolkit for investigating dynamic cell contractility, volume, or surface areas.

1.3 ORGANIZATION OF THESIS

The thesis is a combination of six peer-reviewed manuscripts [3], [4], [7], [10], [14], [15], one conference publication [29] and one non peer-reviewed manuscript (Biorxiv) [16]. Chapter 1 is an introduction to the objectives achieved in this thesis, while going through specific aims. Chapter 2 comprises of Aim 1, covering the resolution quantification, electro-mechanical and optical schematics, in addition to the application of Axially sweeping Sub voxel Light Sheet Microscopy. Chapters 3,4 & 5 comprise of Aim 2, covering the resolution quantification, electro-mechanical and optical schematics, in addition to the application of various modes of LSM such as single/dual side illumination, Sub voxel LSM and multidimensional LSM based on non-gated volumetric acquisition. Moreover, Chapter 4 highlights the application of a dehazing algorithm based on dark channel prior, for isotropic contrast enhancement across three-dimensional volumes analogous to dual illumination LSM. On the other hand, Chapter 5 highlights the application of a scale space feature detector for localization of individual cellular volumes, and thereby enable multidimensional cell tracking or volume quantification. Chapter 6 validates our multidimensional, volume acquisition and tracking pipeline, using transgenic zebrafish with green fluorescent protein expressed in ventricular myocardium and nuclei for quantifying developmental biomechanics and cellular phenotypes.

CHAPTER 2

DEVELOPMENT/APPLICATION OF A 3D LIGHT SHEET MICROSCOPY CAPABLE OF CELLULAR RESOLUTIONACROSS USER-TUNABLE FIELD-OF-VIEW OF 6.5 mm

2.1 INTRODUCTION

LSM is subject to fundamental limitations imposed by the numerical aperture (NA) and objective lens working distance (WD)[1], [19], [30]. Microscopists often face a dilemma in choosing NA for acquisition/detection OL depending on object size and WD[17], [18]. A high excitation NA significantly reduces effective WD of the optical system, thereby limiting light sheet penetration. On the other hand, a low excitation NA produces a thicker light section with longer WD, affecting the signal-to-noise ratio (SNR) of microstructures. Hence, it is a perplexing task to choose an appropriate lens NA[3].

Imaging large vertebrate models such as mice, has traditionally required millimeter-centimeter WD would benefit from low-excitation NA OL[3], [24]. Hence, corresponding image volumes are accompanied with loss in resolution due to low magnification. To combat this, we have developed a LSM variant to modulate the light sheet confocal parameters without compromising spatial resolution and optical section penetration[17]. The AS-sLSM optical geometry includes orthogonal illumination and detection optical geometry, like traditional LSM [3]. An aberration-free remote focus mechanism is used to axially translate the light sheet along the sample depth[31]. This allows you to freely adjust the available field of view (FOV) without moving the excitation OL. In conjunction, sample is acquired at pre-determined offset angle with respect to perpendicular camera position at nanometer voxel sizes, to enable pixel resolution enhancement based on maximum likelihood estimation (MLE)[3], [24]. The off axis scanned raw volume is split into multiple sub-stacks, that are treated as low-resolution (LR) volumes containing

redundant information due to significant image overlap produced by oblique scan[24]. Using MLE, LR stacks are modelled as probability distributions with subtle spatial correlations and furthermore, a cost function based on image degradation operators is minimized to produce a high-resolution estimate from LR image volumes[24]. We hypothesized integration of sub voxel LSM and AS-LSM can be used fully remove dependance of resolution and confocal region on NA.

2.2 LIGHT SHEET MICROSCOPY SPECIFICATIONS[3]

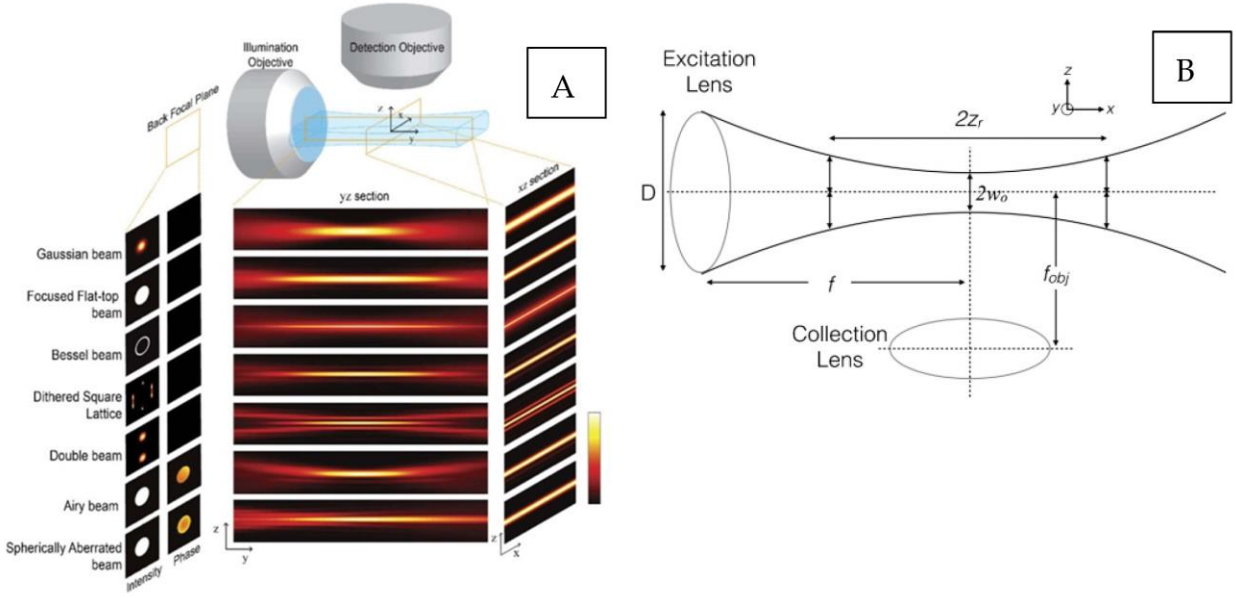

Figure 2.1. LSM beam profile characteristics. (**A**) LSM single lobe and multilobe top-view and side-view intensity distributions (**B**) Gaussian light sheet hyperbolic beam profile, D = lens diameter, Zr = Rayleigh length, w0 = beam waist, f = focal length of objective lens.

Selective planar illumination microscopy yields an intensity distribution that progressively decreases, following a Gaussian peak. In contrast, multi-lobe planar microscopy encompasses additional intensity distributions alongside the primary Gaussian peak. These extra "side-lobes" do not exhibit a consistent decrease and exhibit substantial magnitude when compared to Gaussian "side-lobes." Hence, imaging FOV for a collection OL can be described in terms of the confocal region, b = 2 ∗ Zr =$(2\pi(wo)2)/\lambda$, where Zr = Rayleigh length, λ = wavelength and w0 is the beam waist. The confocal region signifies near-homogenous illumination. Axial resolution can be defined as Raxial = $2wo$ = 2 (nλ)/(2πNA), thereby relating light sheet thickness to sectioning capability. Increasing the FOV requires thicker light sheets; however, this reduces the axial resolution due to the low NA. For light sheet lateral resolution, Gaussian peak full width half maximum (FWHM) is quantified as Rlateral = $0.61\lambda/$(nxNA) where NA is numerical aperture and n is the refractive index of surrounding medium.

2.3 MATERIALS AND METHODS

2.3.1 AXIALLY SWEEPING LIGHT SHEET MICROSCOPE CONSTRUCTION [3]

Laser beam from diode is collimated through beam expander (BE). Gaussian light sheet (LS) is formed by passing beam through pinhole (PH). The LS is focused into a 1D line profile and relayed to the linear focus actuator (LFA) through an air objective (OL1) (RMS4X, OLYMPUS) and optical isolation system consisting of a half wave plate, polarizing beam splitter and quarter wave plate to reduce attenuation. A closed – loop, voice

coil actuator (LFA 2010, Equip Solutions) is used to offset the beam waist at the detection focus and is interfaced to NI FPGA(PCIE-7852R), though voltage amplifier (SCA 814, Equip Solutions), to ensure synchronization between camera readout and axially sweeping illumination. In addition, optical sectioning at varying sample depths was achieved by interfacing a voice coil stage (VCS-10, Equip Solutions) to NI FPGA, through a SCA 814 amplifier. Bidirectional black arrow denotes axial sweeping near detection objective focus (OL3). A very long working distance/low NA (0.1) objective (OL2) (TL2X-SAP, THORLABS) was used to produce optical sections with theoretical thickness (axial resolution) of 3 micrometer for consistent distance (excitation FOV) of 120 micrometers. A macro view lens (MVX10 2X, OLYMPUS) was integrated in the detection arm to acquire detection field-of-view of 6.5 millimeters, with theoretical lateral resolution of 2.3 micrometer (1 camera pixel = 6.5 micron; camera pixel size after 2x magnification = 3.25 micron; field-of-view = total camera pixels x pixel size = 2048 x 3.25 micron = ~6600 microns)

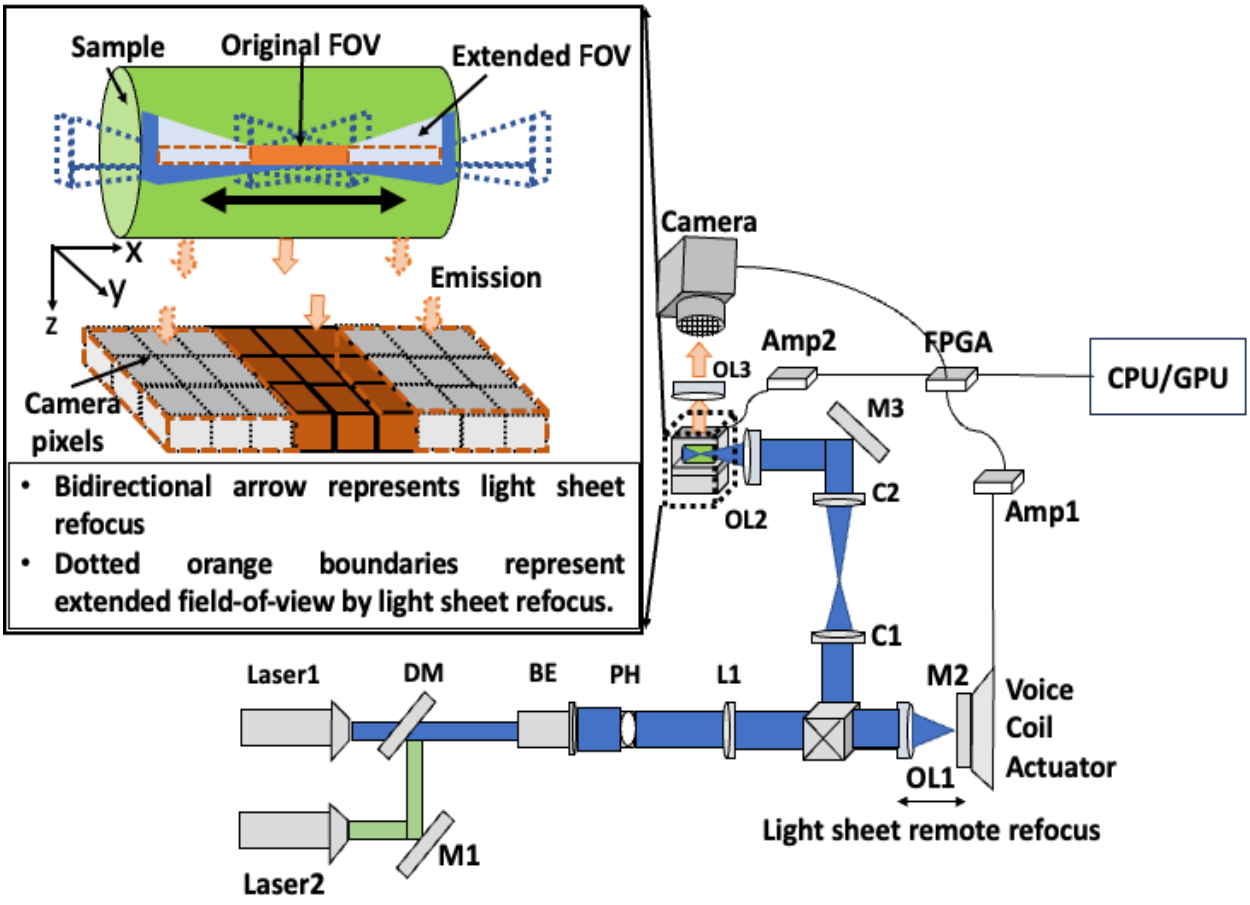

Figure 2.2. Axially sweeping microscope schematic. DM=dichroic mirror, BE=beam expander, BS = beam splitter, PH=pinhole, L=cylindrical lens, OL1=remote refocus objective lens, OL2 = excitation lens , OL3 = detection lens, C=convex lens, M=mirror, Amp=voltage amplifier, FOV=Field-of-view

2.3.2 ROLLING SHUTTER CAMERA PIXEL GATING [3]

A single sided illumination (493 nm) AS-LSM **(Figure 2.3A)**, was integrated with a commercial MVX10 upright macro view Olympus microscope **(Figure 2.3B).** A linear focus actuator (LFA 2010, Equipment solutions, CA) **(Figure 2.3C)** capable of up to nanometer positioning resolution and millisecond response time, was used for producing axial sweeping of line focus. A field programmable gate array (FPGA, PCIe-67852R, National instruments) was used for synchronization of 'rolling' camera pixel readout (active camera pixels) with the light sheet confocal sweep. The LFA actuator position was configured by a servo linear control amplifier (SCA 814, Equipment solutions, CA) through a high-density DB 15 style male connector, and the FPGA **(Figure 2.3D).** A custom rolling shutter code written by Coleman technologies and licensed under Howard Hughes Medical Institute; Janelia Farm research campus was used for performing synchronization of active camera pixels within focus 1D line focus. Briefly, a predefined array of camera pixels was triggered at the start of a sawtooth or triangle waveform, for unidirectional or bidirectional line focus sweeping respectively, and a flyback mechanism was implemented for resetting the remote focus actuator. A sCMOS camera (ORCA flash 4.0, Hamamatsu, Japan), recorded a stack of 2D frames along the longitudinal direction at discrete steps ranging from 1.5-5 micrometers. The number of active camera pixels was calibrated based on the twice the theoretical Rayleigh length.

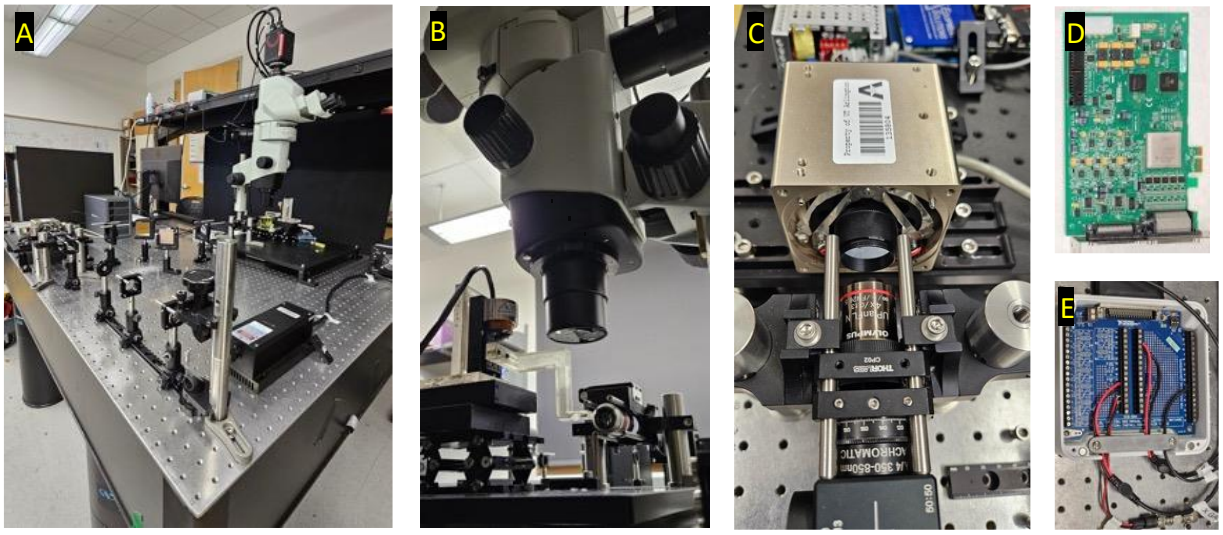

Figure 2.3. Axially sweeping microscope construction. (**A**) Single side illumination setup, (**B**) MVX10 macro view inverted microscope used for detection in perpendicular with respect to excitation plane. **(C)** Voice coil actuator used for remote refocusing of light sheet section**, (D)** FPGA and (E) FPGA Breakout board were interfaced with peripheral components such as CMOS camera, sample translation stage and remote refocusing actuator to synchronize volumetric scan.

2.3.3 SUB VOXEL OFF-AXIS VOLUMETRIC RECONSTRUCTION [3], [4]

A tilted ABS scanning stage was 3d printed, to image sample obliquely as opposed to traditional orthogonal scanning method. Oblique scanning of the sample with a tilted angle should satisfy two conditions: (1) the velocity of the scanning stage should be slower than the framerate of sCMOS camera multiplied by desired voxel depth, and (2) the thickness of the light-sheet is greater than the desired voxel resolution. Volumetric reconstruction of raw images after tilted scan will have redundant information, since each successive optical section contains object overlap from the previous section due to the oblique angle. Hence,

the non-axially scanned raw image stack was split into multiple sub-stacks (P_k), with each sub-stack having slightly different voxel information and treated as low-resolution 3D images **(Figure 2.4A)**. Using maximum likelihood estimation (MLE), we modelled sub-stacks as probability distributions with subtle spatial correlations and reconstruct a final output image that encompasses significantly improved resolution while maintaining large FOV **(Figure 2.4B).** As a result, the MLE strategy intrinsically improves the pixel density due to increased 3D pixel/voxel density. The MLE algorithm is based on minimizing the cost function $\hat{I} = ArgMin[\sum_{k-1}^{n} \rho(P_k, D_k O_k S_k)]$ where P_k represents the kth estimate, resulting in high resolution $\hat{I}$, while D_k and O_k represent the undersampling and blur degradation operators respectively[24] **(Figure 2.4C).** Hence, the MLE-based approach can intrinsically handle object motion, warping, or other factors affecting conventional RS strategy.

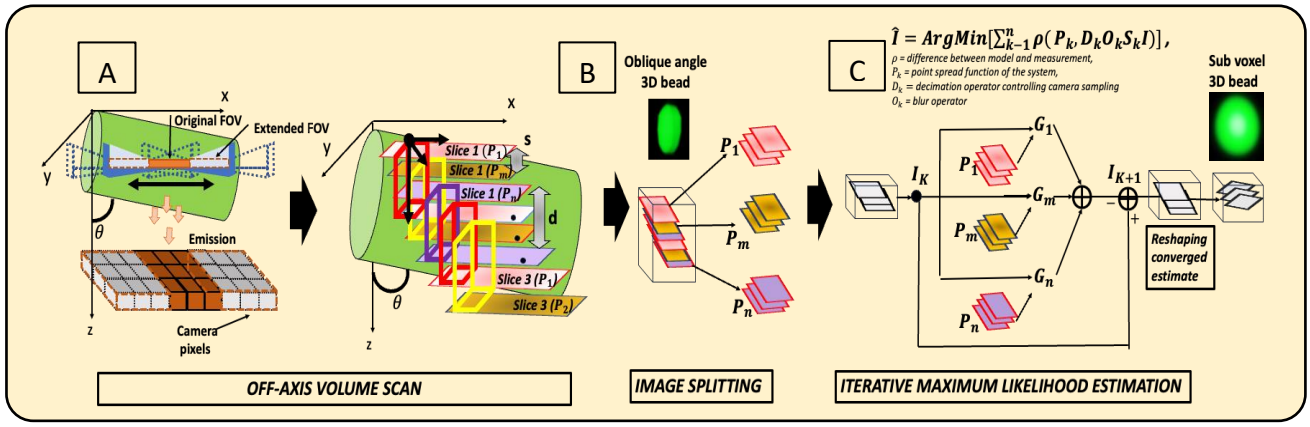

Figure 2.4. Maximum Likelihood Estimation pixel resolution improvement pipeline

IMAGE EXTRACTION

By using the SLSM system with specific scanning vector *s* and optical sectioning depth *I*, we obtain a sequence of large-FOV, LR images denoted by *P*. Further, *P* contains *m* slices each having dimensions of Dim_{lr-x}, Dim_{lr-y}, and pixel sizes of *reslr-x*, *reslr-y*. As *s* is non-orthogonal to either the *x*- or *y*-axes, each *s* yields known unit shifts of s_x and s_y in the lateral direction and of s_z in the axial direction. The raw dataset *P* is then subdivided into multiple groups of LR 3-D images *Pk*, where $k = 1, 2, 3 \ldots n$. To achieve lossless sampling in the axial direction, we set the *z* step size (*reslr-z*) in each *Pk* as one third of *I*. Then, each frame in *P* is extracted and reassigned to *Pk* according to the relation.

$$P_k(z) = P\left(\frac{(z-1)\times l}{3\times s_z} + k\right), \quad \text{-(1)}$$

where $z = 1, 2, 3 \ldots$, Dim_{lr-Z} represents the *z* position in a given *Pk*. Dim_{lr-Z} denotes the total slice number in each *Pk* and can be calculated from

$$Dim_{lr-z} = \frac{m\times 3\times s_z}{l}. \quad \text{-(2)}$$

The generated *Pk,* with dimensions *Dimlr-x* × *Dimlr-y* × *Dimlr-z* and voxel size *reslr-x* × *reslr-y* × *reslr-z*, are equivalent to a series of measurements that simply accept the native resolution from the system optics but contain sub-voxel spatial correlations with each other. The total number of *Pk* (i.e., *n*) is determined by, under a given nonaxial scanning vector

and step size, the number of steps necessary to generate a shift across an entire LR voxel. In our configuration, as the entire voxel scan is always accomplished by finishing a one-voxel-sized shift in the lateral direction, the number of Pk images is then calculated from

$$n = \frac{reslr_x}{s_x}. \quad \text{-(3)}$$

ITERATIVE SVR COMPUTATION

We define the HR image to be solved as I, which has the following dimensions on each axis:

$$Dim_{\mathrm{hr}-x} = Dim_{lr-x} \times e_x,\ Dim_{\mathrm{hr}-y} = Dim_{lr-y} \times e_y,\ Dim_{\mathrm{hr}-z} = Dim_{lr-z} \times e_z.$$

Here, ex, ey, and ez are resolution enhancement factors that indicate the extent of the scale-up in the lateral and axial directions. Their product, defined as *e*total is kept approximately the same as the number of LR images (Pk), to minimize both the under- and over-determined problems. Then, one of the LR images, e.g., $P1$, is interpolated to fill the HR grid, creating an initial estimate of HR $I1$ for iterative optimization

$$I_1 = \mathrm{interpolate}(P_1, [Dim_{hr-x}, Dim_{hr-y}, Dim_{hr-z}]).$$

The core aspect of the SVR procedure is the search for a HR estimate I that is consistent with many LR measurements $P\boldsymbol{k}$ after a sequential sub-voxel shift Sk, optical blurring Ok, and digital sampling Dk are applied.

(1) The 3-D shift operation, where

$$s_{k,(x,y,z)} = \frac{(k-1) \times s_{(x,y,z)}}{res_{(x,y,z)}/e_{(x,y,z)}} \quad . \qquad \text{-(4)}$$

(2) The 3-D convolution operation O_k, which is performed using a measured PSF kernel that is simply the 3-D image of a sub-resolution point source, or a generated PSF kernel that has a Gaussian-like distribution with the sigma value in each axis defined as

$$Sigma_{x,y,z} = \frac{ext_{x,y,z} \times e_{x,y,z}}{4 \times res_{lr-x,y,z}}. \qquad \text{-(5)}$$

Here, $ext_{x,y,z}$ indicates the estimated extent of the sub-voxel point source in each direction.

(3) The 3-D decimation operation D_k, which is implemented by choosing the voxels in each degraded model with coordinates

$$[e_x \times (x-1)+1, e_y \times (y-1)+1, e_x \times (z-1)+1]. \qquad \text{-(6)}$$

These n groups of degraded I_1 are compared with the corresponding P_k through calculation of the sum of their difference in a HR grid, with

$$\sum_{k=1}^{n} S_k^T O_k^T D_k^T sign\left(D_k O_k S_k \hat{I}_n - \underline{P}_k\right), \qquad \text{-(7)}$$

where S^T, O^T, and D^T represent the opposite shift, padding interpolation, and deconvolution operation, respectively, and correspond to the transpose of S, O, and D. Then, the second estimate $I2$ can be obtained by implementing the steepest descent formula.

VOXEL REALIGNMENT

Compared with the real sample structure, the solved HR *ISVR* still exhibits slight deformation caused by the nonaxial scanning. To eliminate this inaccuracy, we re-align each slice of *ISVR* in the *x*-*y* plane to offset the lateral signal drift. For the j^{th} (j = 1, 2,3..., Dim_{hr-z}) slice, the number of pixels shifted on the *x*- and *y*-axes is given by

$$deform_x(j) = \frac{(j-1) \times res_{lr-z}/e_z \times s_x/s_z}{res_{lr-x}/e_x}, \quad \text{-(7)}$$

$$deform_y(j) = \frac{(j-1) \times res_{lr-z}/e_z \times s_y/s_z}{res_{lr-y}/e_y}. \quad \text{-(8)}$$

After voxel realignment is applied, we obtain the final output *Ifinal*, thereby reconstructing the object with greatly increased SBP and accurate signal distribution.

2.3.4 TISSUE CLEARING PROTOCOL FOR AUTOFLUORESCENCE IMAGING

Our tissue clearing protocol includes 5 steps: fixation, permeabilization/decolorization, delipidation, dehydration, and RI matching[32]. Fixation requires 1x phosphate buffered saline (PBS) and paraformaldehyde (PFA). Permeabilization/decolorization uses CHAPS, N-methyldiethanolamine (NMDEA), Quadrol, and Ammonium. Delipidation uses Tert-Butanol (tB) in combination with Quadrol while dehydration uses tB, polyethylene glycol

(PEG), and Quadrol. RI matching is tested with PEGASOS (PEG associated solvent system) and BABB (benzyl benzoate/benzyl alcohol) to compare optical transparency.

Fixation

The mouse organs are received in conical tubes filled with 1x PBS. The organs are immediately placed in fresh 1x PBS and gently shaken at 4℃ (Thermo Fisher Vari-Mix Platform Rocker) for 30 minutes. The samples are replaced with fresh 1x PBS and shaken for an additional 1 hour. The samples are then immersed in 4% PFA for 30 minutes and replaced with fresh 4% PFA for 24 hours. Again, replaced with fresh 1x PBS every hour twice. Then, they are immersed in fresh 1x PBS again and kept in 4℃ until they are ready to be cleared.

Passive immersion

After fixation, each sample is rotated at 37℃ at ~100 rpm (Thermo Fisher MaxQ 4450). The first stage is decolorization in CHAPS/NMDEA for 24 hours. This is done to increase the permeability of the organ prior to further depigmentation. Non-heavily colorized organs (lungs, pancreas, and brain) are decolorized for an additional 24 hours while heavily colorized organs (heart, kidneys, liver, spleen, and tongue) are decolorized for another 72 hours in 25% Quadrol. Heavily colorized organs are also immersed in 5% ammonium solution for 6 hours afterward for further heme reduction. Delipidation is done in tB with 3% Quadrol. There are 3 dilution stages: 30% tB, 50% tB, and 70% tB. Each step is performed for 8 hours. Dehydration is performed for 24 hours with tB-PEG, a combination

of 70% tB, 30% PEG, and 3% Quadrol. The RI matching step is performed in either PEGASOS or BABB for 24 hours.

Stage	Chemical	Duration (1 mm slices)	Duration (Whole Organs)	Temperature & Speed
Fixation	PBS & PFA	PBS (30 min) PBS (1 hr) PFA (30 min) PFA (24 hr) PBS (1 hr) PBS (1 hr)		4°C & ~15 rpm
Decolorization	CHAPS/NMDEA 25% Quadrol Ammonium	CHAPS/NMDEA (12 hr) Quadrol (12 hr)	CHAPS/NMDEA (24 hr) Quadrol (48 hr NHC & 96 hr HC) Ammonium (6 hr HC)	37°C & 100 rpm
Delipidation	Tert-Butanol (tB)	30% (2 hr) 50% (4 hr) 70% (4 hr)	30% (8 hr) 50% (8 hr) 70% (4 hr) 70% (4 hr)	
Dehydration	tB-PEG	24 hr	48 hr	
RI Matching	PEGASOS or BABB	12 hr	24 hr	

Table 2.1. Benzyl Benzoate (BABB) tissue clearing protocol timeline.

2.3.5 RESOLUTION QUANTIFICATION AND STATISTICAL ANALYSIS

1-5 micron green fluorescent microspheres (Cospheric,USA) were embedded in agarose gel to match refractive index with surrounding water medium (RI of agarose & water ~ 1.33). Sub-diffraction beads were used for resolution quantification to test practical resolution vs theoretical resolution results. 3D bead cross sectional profiles were acquired by sample acquisition of 1.5 micrometer step size (voxel size), and the Full Width Half Maximum (FWHM) was calculated for gaussian intensity profiles of beads for both XY and YZ planes. 10 beads were selected at random using different modes of the microscope (mode 1 – 10 beads, mode n = 10 beads etc). Due to non-compliance with normality, Paired t- test assuming unequal variances (independent t-test) was performed to check significant differences in lateral and axial resolution respectively. All different modes of the microscope used same 0.2 NA/2X magnification detection lens. P-value (significance) was set at 0.05. Mean, median and standard deviation of resolution characteristics have been calculated and plotted as box and whiskers plots.

2.4 RESULTS

2.4.1 INSTRUMENT CHARACTERIZATION FOR CONVENTIONAL LIGHT SHEET MICROSCOPY (LSM) AND AXIALLY SWEEPING LSM MODES

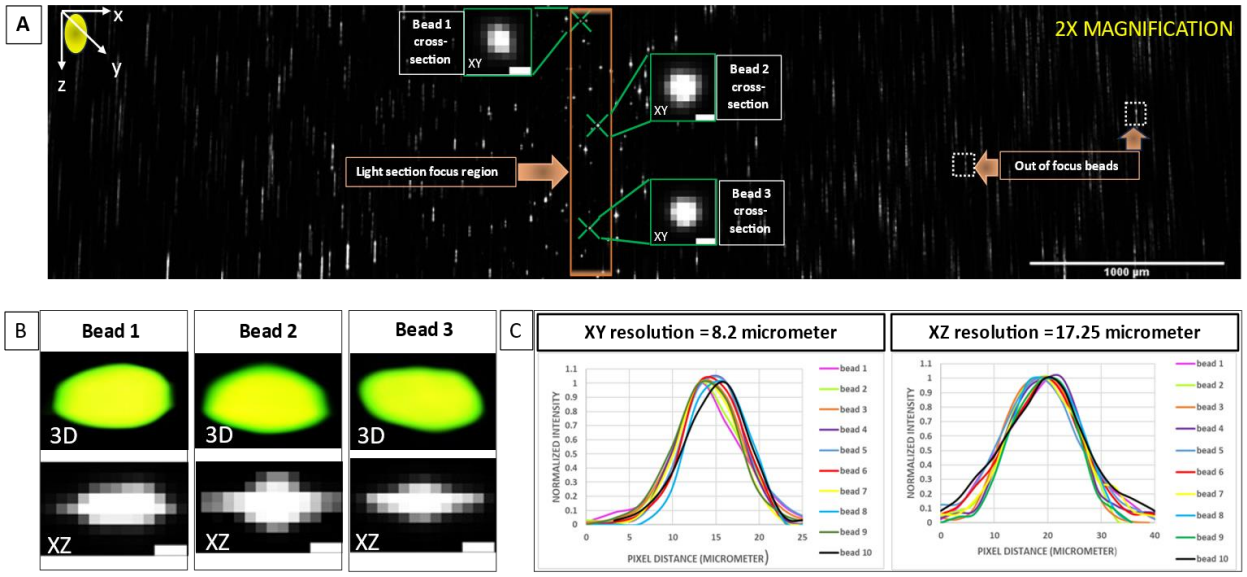

Figure 2.5. Non-Rolling Shutter Field-of-View pixel resolution. (A) Axial perspective (XZ) of raw 120 micrometer excitation Field-Of-View (focused region in solid orange window), produced by 5 cm working distance objective lens in an agarose slab of 6500 x 1500 micrometers (XZ) containing fluorescent microspheres. 6.5 mm detection FOV is captured using 2x magnification objective with working distance of 6.5 cm. (B) Volumetric reconstruction of individual beads highlighted in zoomed in regions along with their axial intensity profile (C) Gaussian intensity profile distribution used for calculating full width half maximum of lateral and axial perspectives of micron beads. Scale bar for XY zoomed in regions and YZ = 9 micron

In order to characterize ground truth voxel resolution (3d pixel), we imaged a agarose slab of 6.5 mm x 1.5 mm using a 5 cm working distance lens, to produce optical section of 3 micron theoretical thickness (axial resolution). We were able to image millimeter field-of-view using a 6.5 working distance detection lens thereby enabling multi-scale imaging. Sample was translated at 1.5-micron steps for ~4200 slices, and reconstructed **(Figure 2.5A) to** visualize 3D stack of micron beads embedded in agarose **(Figure 2.5A).** We quantified the propagation distance of the light sheet to be 120 microns **(Figure 2.5A-rectangle with solid orange border**), equivalent to theoretical excitation FOV of 120 micron produced by 5 cm working distance objective. Further, we reconstructed lateral and axial perspectives for n = 10 beads across the excitation FOV **(Figure 2.5B)** and calculated Full width half maximum of gaussian intensity profile for respective views **(Figure 2.5C).** We observe lateral resolution of 8.2 +/ 0.8 micron and axial resolution of 17.25 +/-1.75 micron **(Figure 2.6D)** for 2x magnification. Hence, we sought to extend this resolution across tunable millimeter (<7 millimeter) FOV and swept the light sheet focus ~50 x using a voice coil actuator to cover 6.5 mm **(Figure 2.6A).** In theory, n = 40 camera pixels at the center of the camera pixel grid were modulated on and off in synchrony with the sweeping beam waist. The number of active camera pixels depends on the theoretical excitation FOV, as in this case 1 pixel = 6.5 um^2/2x magnification = 3.25 um. Thereby, 40 pixels x 3.25 um yields theoretical resolution of 120 um. After visualizing the XY and YZ beam Full width half maximum **(Figure 2.6 B -C),** we quantified lateral resolution of 8.45 +/- 0.9 um and axial resolution of 17.9 +/- 2 micron cross entire 6.5-millimeter FOV. More

importantly, no significant difference was observed after statistical testing was performed **(Figure 2.6D)**

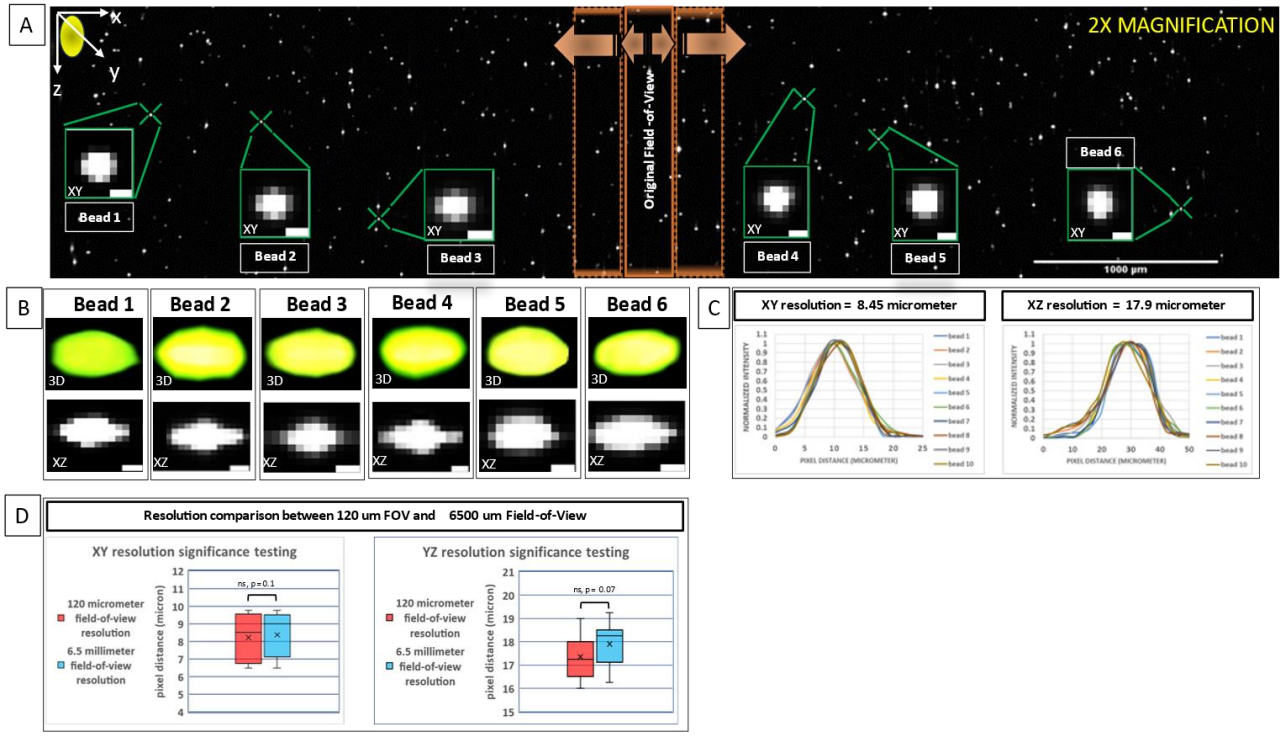

Figure 2.6. Rolling Shutter Field-of-View pixel resolution. (A) Axial perspective of raw 120 micrometer excitation Field-Of-View, (solid orange window at center), axially displaced across agarose slab of 6500 X 1500 micrometers (XZ). Rolling shutter pixel gating was implemented to stitch displaced light sheet foci (dotted orange windows) across entire camera pixel sensor array (B) Volumetric reconstruction of individual beads highlighted in zoomed in regions along with their axial intensity profile (C) Gaussian intensity profile distribution used for calculating FWHM for lateral and axial perspectives of fluorescent beads. (D) Statistical testing performed for resolution characterization between axially swept and non-axially swept agarose volume (n =10 beads, alpha value = 0.05). Mean value denoted by x and median denoted by solid horizontal line.

2.4.2. TUNABLE PIXEL RESOLUTION ENHANCEMENT ACROSS TUNABLE MILLIMETER FIELD-OF-VIEW

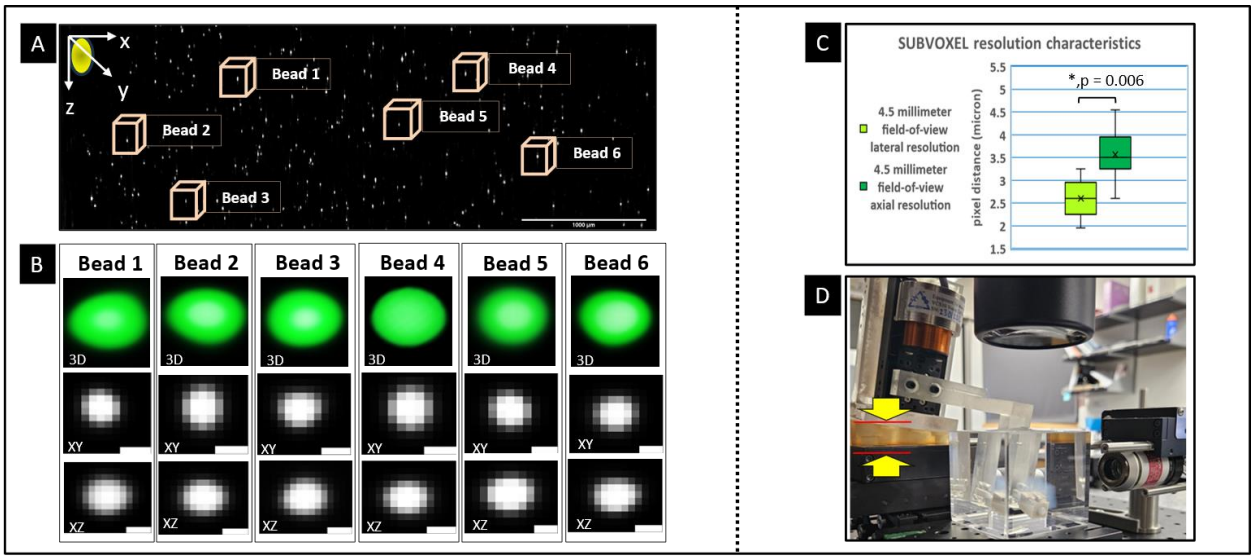

Figure 2.7. Axially sweeping sub voxel light sheet mode pixel resolution. (A) Axial perspective (XZ) of 4500 micrometer excitation Field-Of-View (FOV), acquired by sweeping a 120-micron long (~30 pixels) optical section across 1400 pixels (1 pixel = 3.25 micron) (B) Volumetric reconstruction of beads post voxel resolution enhancement. (scale bar for A = 100 um, B ~2.5 um) (C) T test performed to validate isotropic nature of XY and YZ resolution (n = 10, alpha value = 0.05) (D) Sub voxel off- axis detection, as opposed to orthogonal sample scan**.** Scale bar for XY zoomed in regions and YZ = 3 micron.

Using axially sweeping LSM mode, we were able to achieve XY resolution of 8.45 +/- 0.9 um and YZ resolution of 17.9 +/- 2 micron cross entire 6.5-millimeter FOV using a 2x detection lens in conjunction with a 1.8 cm working distance remote refocus objective **(Figure 2.2).** In this, we observe that modulation of light sheet remote refocus distance is limited by the remote refocus objective lens working distance and detection magnification.

Consequently, reducing detection lens magnification will yield higher FOV up to cm scale, but will be accompanied with loss in lateral and axial resolution. Hence, to combat this we integrated sub voxel light sheet microscopy with axially sweeping light sheet microscopy. A 4500 x 2000 (XZ) micron thick agarose sample **(Figure 2.7A)** embedded with 1-micron fluorescent microspheres was acquired at a tilt angle of 10 degree with respect to orthogonal detection **(Figure 2.7D),** using axially sweeping LSM. The sample was acquired at voxel shifts of 1 micron, (one-third of theoretical axial resolution) and passed through a cost function utilizing the maximum likelihood estimation algorithm. Upon resolving sub-voxel beads **(Figure 2.7B),** we quantified the Full Width Half Maximum of XY and YZ gaussian intensity profiles, for n = 10 beads selected at random across the entire FOV **(Figure 2.7B).** Here we observe significant reduction in lateral pixel resolution of ~ 3x ($p<0.01$) and ~4.5x($p<0.01$) in axial resolution **(Figure 2.7C).** We quantified near isotropic lateral resolution of 2.45 +/- 0.8 micron and axial resolution of 3.65 +/ 0.9 micron across entire 4500 micrometer Field-of-view. However, we observed significant difference between lateral and axial resolution of sub voxel beads **(Figure 2.7C ($p = 0.03$ for alpha value threshold at 0.05),** and thereby were unable to achieve isotropic voxel (3D pixel) resolution. In this regard, we can conclude integration of sub voxel LSM and axially sweeping LSM truly decouples optical limitations imposed by lens magnification on resolution and FOV.

2.4.3 VOLUMETRIC RECONSTRUCTION OF BENZYL BENZOATE OPTICALLY CLEARED WHOLE MOUSE KIDNEY USING AXIALLY SWEEPING LSM

To validate multi-scale imaging capability of AS-LSM without loss in detail, we imaged autofluorescence of optically cleared whole mouse kidney. Mice kidneys were explanted, transcardially perfused with paraformaldehyde and PBS and post-fixed. Samples were passaged through a decolorization solution, gradient delipidating solution, and the BABB clearing medium to achieve transparency **(Figure 2.8A).** 3-millimeter-thick kidney volume was sampled at z step of 5 micron while sweeping light sheet focus across 6.5 mm FOV, to reconstruct 3D stack **(Figure 2.8B).** We were able to observe macro scale features such as RP (renal pelvis), RM (renal medulla) and RC (renal cortex), while also being able to reconstruct micro vasculature (RV) such as renal blood vessel walls without any loss in detail using a 2x magnification objective. Using polarization optics implemented in our light sheet setup, we altered refractive index between BABB refractive index matching medium and interstitial plasma/fluid etc. Consequently, we induced contrast between vessel walls and endogenous fluorescent micro vasculature for volumetric reconstruction. More importantly, this demonstrates the potential of RS-LSM to provide micron scale resolution for deep tissue imaging (millimeter-centimeter scale).

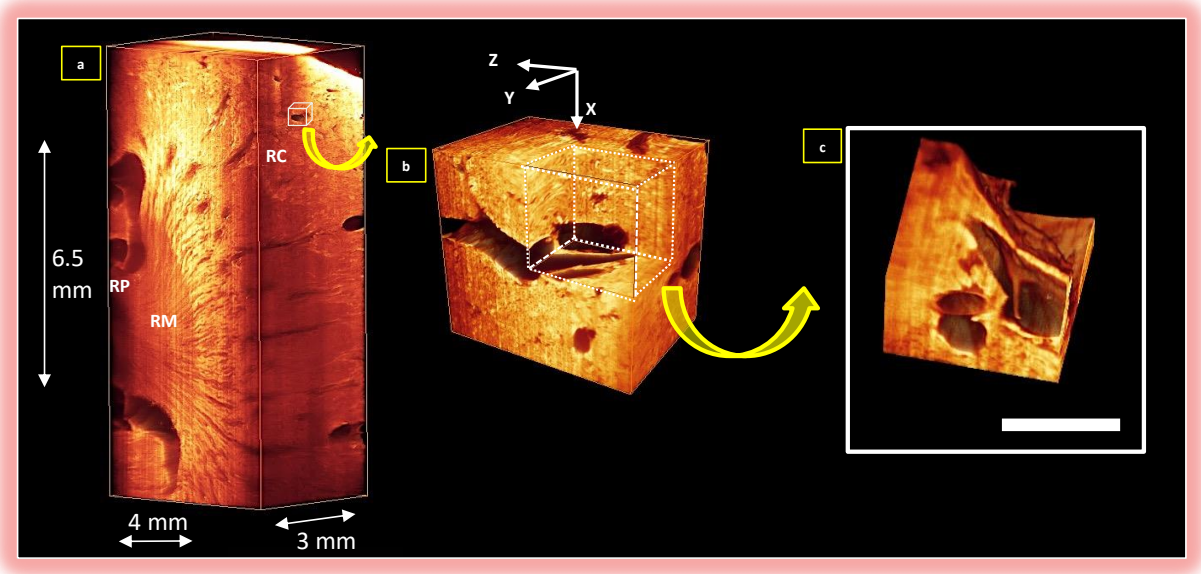

Figure 2.8 Volume reconstruction of Benzyl Benzoate cleared auto fluorescent kidney (A)3-millimeter-thick kidney volume was sampled at sectioning distance (voxel size) of 3 micron while sweeping light sheet focus across 6.5 mm. (B and C) Multi-scale imaging achieved using 2x detection lens, for resolving renal vessel and vasculature. (RP=renal pelvis, RM=renal medulla, RC=renal cortex, scale bar = 15 micron)

2.4.4 VOLUMETRIC RECONSTRUCTION OF BENZYL BENZOATE OPTICALLY CLEARED WHOLE MOUSE LUNGS USING AXIALLY SWEEP

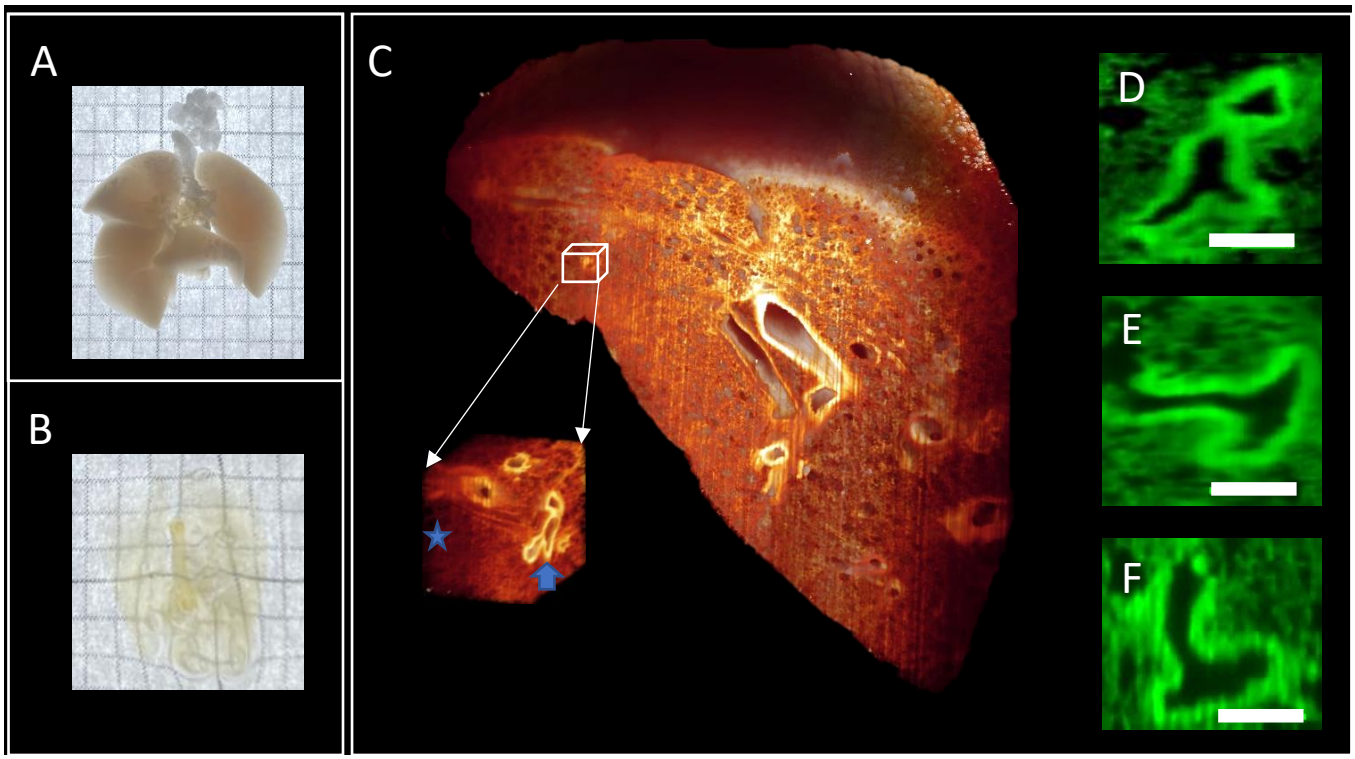

Figure 2.9 Volume reconstruction of microstructures in Benzyl Benzoate cleared auto fluorescent mouse lung (A) Mouse lungs post fixation (B) Mouse lungs after optical clearing using Benzyl benzoate (C) represents whole right lung reconstruction with zoomed in region of alveolar structure and vessels (D-F) represents front view, side view and top views respectively of zoomed in vessel structure in (C). (Square boxes in A & B = 1x1 mm, scale bar for D-F = 10 micron) (Blue star represents the alveolar autofluorescence, while blue arrow represents the vessel endothelium)

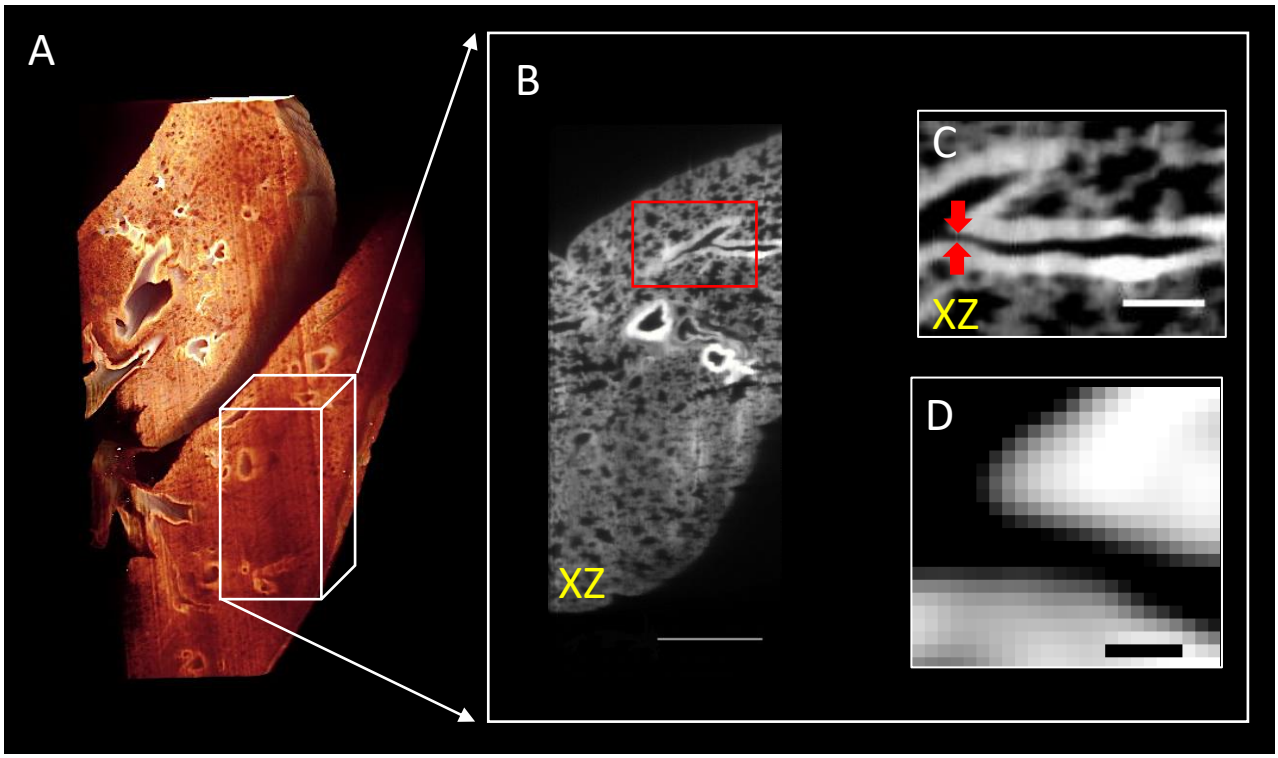

Figure 2.10 Volume reconstruction of macro structures in Benzyl Benzoate cleared auto fluorescent mouse lung (A) 1-millimeter-thick murine lung volume was sampled at sectioning distance (voxel size) of 3 micron while sweeping light sheet focus across 6.5 mm. (B and C) Multi-scale imaging achieved using 2x detection lens, for resolving lung airways (B) represent the axial reconstruction of murine right lung. (D) is zoomed in version of the vessel visualized in (C) (scale bar for B = 500-micron, C = 100-micron, D = 20 micron)

We reconstructed murine left and right whole lung, after optical clearing using benzyl benzoate. The lungs were sampled at 3 micrometer steps, requiring ~ n = 330 slices to reconstruct 1 mm thick volume. Consequently, we were able to visualize biological volumes across multiple scales from less than 15 micrometers **(vessel structure – Figure**

2.9) and beyond 500 micrometers **(lung airways - Figure 2.10),** using a very low magnification (2x) detection lens across 6.5 mm field-of-view. More importantly we did not have to resort to time and computation intensive image mosaicking. This is often required for large samples due to image acquisition with higher magnification lenses to maintain structural integrity of microstructures across the whole field-of-view.

2.5 DISCUSSION

2.5.1 SIGNIFICANCE

Resolution characteristics of LSM modality are determined by the excitation lens NA for axial resolution (optical section thickness), and detection lens NA for lateral resolution. Hence, the modality fundamentally suffers from tradeoff in optical performance, while performing deep tissue imaging due to low NA of long working distance objective lenses. In this regard, rolling shutter based axially sweeping LSM provides promise with respect to achieving cellular resolution across millimeter to centimeter scale imaging. However,

axially sweeping LSM modality intrinsically suffers from optical resolution limitations imposed by lens NA as well, forcing tradeoff between field-of-view enhancement and lens NA. Hence, we have integrated sub voxel LSM with axially sweeping LSM to dispose of optical diffraction limitations and enable modulation of optical resolution that is not proportional to the lens characteristics. We were successfully able to quantify XY resolution of 2.45 +/- 0.8 micron and axial resolution of 3.65 +/ 0.9 micron across entire

4500 micrometer Field-of-view. This was achieved by sweeping 120-micron long light section across 2048 camera pixels, using a 1.8 cm working distance, remote-refocusing objective lens (Figure 2.2). Moreover, we were able to achieve near theoretical resolution values of 2.45 +/- 0.8 micron [Theoretical resolution = $(0.61\lambda/(\text{refractive index x NA})$ = (0.61 x 0.493/1.3x0.25) = 2.2 micrometer] and axial resolution of 3.65 +/ 0.9 microns [Theoretical resolution = $(2*(\lambda \text{ x focal length})/(3.14 \text{ x NA}))$ = (150mm x 0.493/1.3x0.25) = 3 micrometer]. In the wake of novel in vitro modelling platforms such as optical tissue clearing, axially sweeping sub voxel LSM can be integrated to observe subcellular organelles or nanometer phenotypes that have traditionally restricted to very low working distance lenses. Consequently, enabling global area quantification in conjunction with local morphogenesis quantification.

2.5.2 LIMITATIONS

Current sub voxel based axially sweeping LSM is restricted to only multiscale imaging for static in vitro/in toto biological platforms. As synchronization of sweeping light sheet foci across the imaging FOV is in tandem with camera exposure time optical sectioning, it cannot be used for multi-dimensional imaging requiring rapid camera frame rates due to pixel exposure limitations. Hence, future improvements need to be made in this regard. Furthermore, imaging FOV enhancement is proportional to the working distance of the objective and hence imposes constraints on resolution that can be achieved. Moreover, currently axial sweeping LSM suffers from stripe effects due to single side illumination and future improvement consists of destriping using dual side illumination.

2.6 SUPPLEMENTARY FIGURES

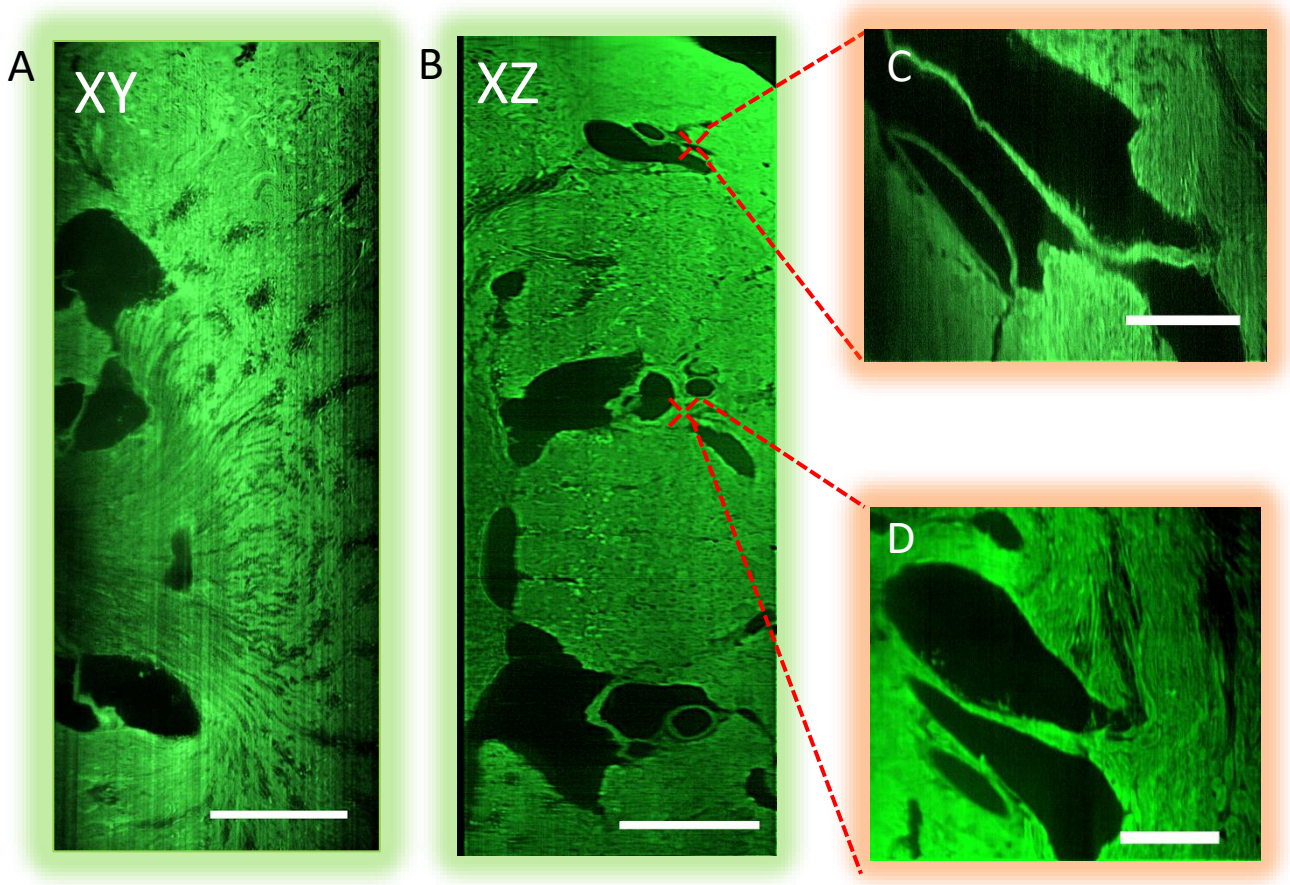

Figure S1. Orthogonal perspectives of Benzyl Benzoate cleared auto fluorescent mouse kidney (A) represents front view, while (B) represents the axial perspective of kidney volume . (C) & (D) represents zoomed in perspectives of kidney vessel structure along the axial perspective (scale bar for A & B = 500-micron, C & D = 30 micron)

CHAPTER 3

CDEVELOPMENT OF 3D LIGHT SHEET MICROSCOPE, CAPABLE OF CELLULAR RESOLUTION ACROSS TUNABLE FIELD – OF – VIEW UP TO 1 MILLIMETER

3.1 MATERIALS AND METHODS

3.1.1 LSFM SETUP [4]

Our tunable LSFM was setup to be able to use single side illumination, dual-side illumination, multi-view fusion, and oblique scanning for the VSR technique. To cover the entire width of the zebrafish, we calculated the confocal range from double of the Rayleigh length (z_R) which is

$$z_R = \frac{\pi w_0^2}{\lambda} \quad \text{-(9)}$$

where λ is the wavelength of our laser (473nm) to illuminate the green fluorescent protein in the transgenic zebrafish line; and w_0 is the beam waist, which is the thinnest focal point of the Gaussian beam.

The width of light-sheet $w(z)$ along the z-axis can be calculated as follows:

$$w(z) = w_0 \sqrt{1 + \left(\frac{\lambda \cdot z}{\pi \cdot w_0^2}\right)^2} \quad \text{-(10)}$$

We also adjusted the slit width to control the light-sheet thickness at the sides of the sample of $\sqrt{2}w(z)$, which is the thickness of the light-sheet under Rayleigh length.

3.1.2 VOXEL SUPER-RESOLUTION [4]

The technique of super-resolution by using oblique scanning follows the principle of the function of pixel super-resolution techniques in a 2D spatial domain. Super-resolved estimate $\underline{I}$ is most consistent with multiple measurements $\underline{P_k}$ after a series of degradation operators. Here, we solved $\underline{I}$ via minimizing the following cost function:

$$\hat{\underline{I}} = \underset{\underline{I}}{\text{ArgMin}}[\sum_{k=1}^{n} \rho(P_k, D_k O_k S_k \underline{I})], \quad \text{-(11)}$$

where ρ is the difference between the model and measurements. S_k is the geometric motion operator between HR (high-resolution) estimate $\underline{I}$ and k^{th} LR (low-resolution) $\underline{P_k}$, the point-spread-function of the oblique scanning LSFM system is modeled by the blur operator O, and D_k represents the decimation operator that models digital sampling of the camera. Theoretically, the computation estimates a unique HR image, which has maximum likelihood to the LR inputs after given degradations S_k, O_k, and D_k are applied. Practically, a steepest descent method is provided to iteratively approach a converged super-resolved solution at high efficiency,

$$\hat{\underline{I}}_m = \hat{\underline{I}}_{m-1} - \beta[\sum_{k=1}^{n} S_k^T O_k^T D_k^T sign(D_k O_k S_k \hat{\underline{I}}_{m-1} - \underline{P_k})], \quad \text{-(12)}$$

where S_k^T, O_k^T, D_k^T represent the transpose of S_k, O_k, D_k respectively. ***(refer Chapter 1 for complete description)***

3.2 RESULTS

3.2.1 IMPLEMENTATION OF LSFM [4]

Our tunable LSFM is composed of dual-side illumination pathways integrated with multi-dimensional image fusion (**Figure 3.1a**). In the illumination path, a cylindrical lens coupled with 4x objective lens (4X Plan Apochromat Plan N, Olympus, Tokyo, Japan) generated a collimated Gaussian light-sheet. From the calculation of Rayleigh length (half of the confocal range), we reduced the mechanical slit to 1.99 mm to generate a 15 mm confocal range to cover the circumferential length of 4 days post fertilization (dpf) zebrafish. To eliminate stripe effects, we added a galvanometer mirror and optimized the system with at a frequency of 2000 Hz (**Figure 3.1a)**. When the sample was scanned through the confocal range of the light sheet along the z-direction, the sCMOS camera (ORCA flash 4.0, Hamamatsu, Japan), located at the end of the detection path coupled with a tube lens, recorded a stack of 2-D plane images along different z depths. An attachable oblique scanning adapter could be easily added for applying the voxel super-resolution technique to provide high spatial resolution from a low power objective (**Figure 3.1b**).

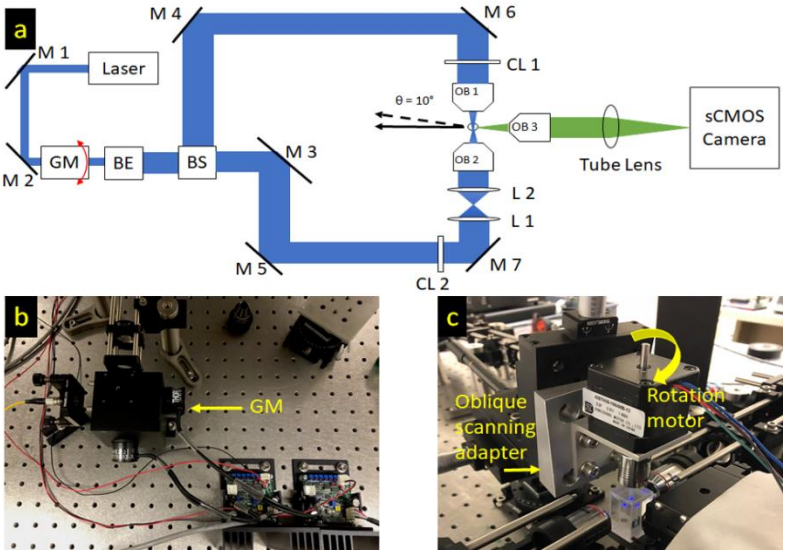

Figure 3.1. Schematic representation of the light sheet fluorescence microscopy system. (a) A 2-D top view of the LSFM system, with each component showing the transformation of beam shape. The scanning direction of the sample is indicated by the black arrow. The solid arrow represents the scanning direction for single-sided, dual-sided, and multi-view imaging. The dashed black line shows the oblique scanning angle used for super resolution. (b) Galvanometer mirror (GM) attached to the system before the beam expander.

3.2.2 INSTRUMENT CHARACTERIZATION FOR SINGLE SIDED AND DUAL SIDED ILLUMINATION MODES

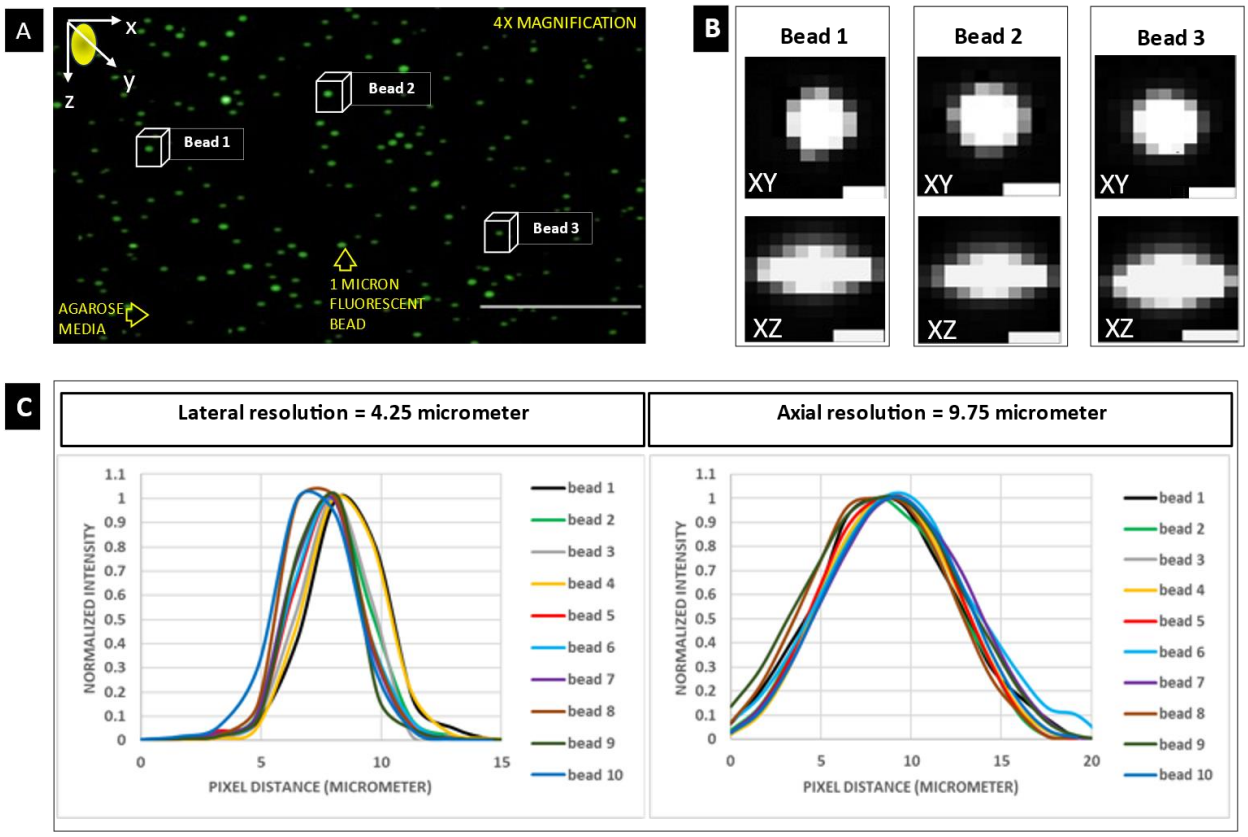

Figure 3.2 Single side illumination light sheet spatial characteristics. (A) 500 micrometer Field-of-view produced by 4x,0.13 NA lens. (B) Beads inspected at random across the FOV for resolution quantification. (C) Gaussian profiles for point spread functions.

We integrated varying light sheet modes into our 3D/3D+time imaging pipeline, namely single sided illumination, dual excitation, and sub voxel LSM. This study was based on characterizing spatial resolution of microscope for all these modes to validate instrumentation accuracy. Furthermore, we have focused this study solely on 3D image

acquisition. This is due to sub voxel pixel enhancement algorithm being incompatible with 4D synchronization algorithm, used to re-arrange non-gated adjacent time lapses synchronously described in later chapters. However, 3D spatial resolution can be used to characterize instrumentation accuracy for both static and multi-dimensional imaging modes.

Like chapter 2, we used 1 micrometer, green emission wavelength microspheres embedded in 0.5 % low melting point agarose, inside a FEP (fluorinated ethylene propylene) tube (Figure 3.1b) to characterize system resolution of the microscope. Using a 4x detection objective and 4x excitation objective (OLYMPUS PLN Plan Achromat 4X, 0.13 NA), we calculated theoretical XY resolution (lateral resolution = [wavelength x 0.61/refractive index x lens numerical aperture) of ~1.7 micrometer, as opposed to theoretical resolution of 1 micrometer for 0.25 NA excitation objective lens used in chapter 1. On the other hand, we calculated theoretical optical sectioning thickness of ~6 micron (axial resolution = [2x (wavelength x cylindrical lens focal length/3.14 x beam radius), resulting in beam propagation of approximately 500 micrometer ([2x3.13x(axial resolution)^2]/wavelength).

No remote refocus optics have been integrated in this setup resulting, due to which we modulate the confocal region by varying beam radius using a mechanical slit in the excitation optical train **(Figure 4.1).** For these specifications we obtained a XY resolution of 4.25 +/ 0.7 microns and YZ resolution of 9.75 +/ 1.1 microns for singe side excitation **(Figure 3.2c, Figure 3.3b),** in conjunction with XY resolution of 4 +/- 0.6 microns and YZ resolution of 7.1 +/- 0.7 micrometer for dual side excitation. We did not observe significant

difference in lateral resolution between both modes **(Figure 3.3b**, paired t test, n =10 beads, alpha value = 0.05), however observed significant reduction in the axial resolution by **(Figure 3.3 B)** ~2 micrometers (p = 0.001, paired t test, n = 10 beads, alpha value = 0.05) for dual side illumination. This is due to dual excitation optics, compensating for attenuation and other aberrations in the point spread function and can be visualized through orthogonal perspectives for both modes **(Figure 3.1a, Figure 3.3a).**

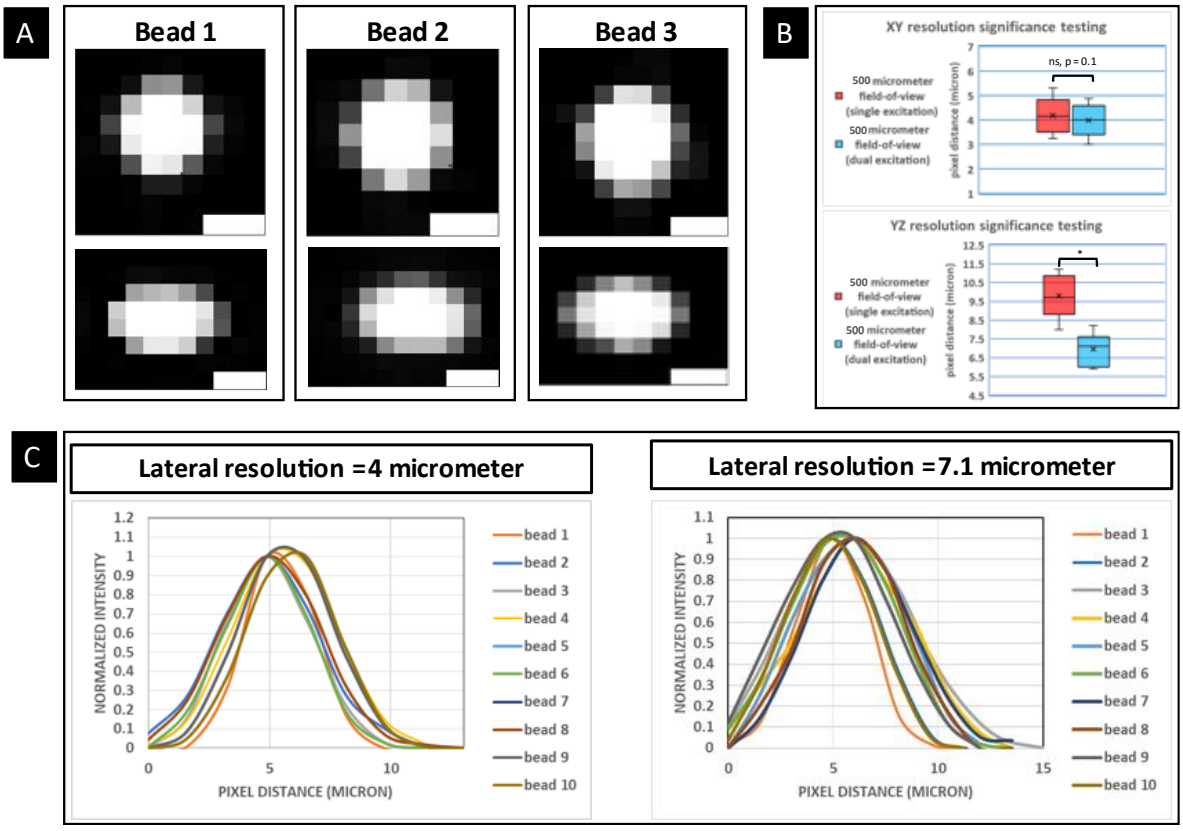

Figure 3.3 Dual illumination light sheet spatial characteristics. (A) Beads inspected at random across the FOV for resolution quantification. (B) Statistical testing significance for single- and dual illumination light sheet modes (C) Gaussian intensity profiles used to calculate full Width Half Maximum of beads

3.2.3 PIXEL IMPROVEMENT USING SUB VOXEL LIGHT SHEET MICROSCOPY

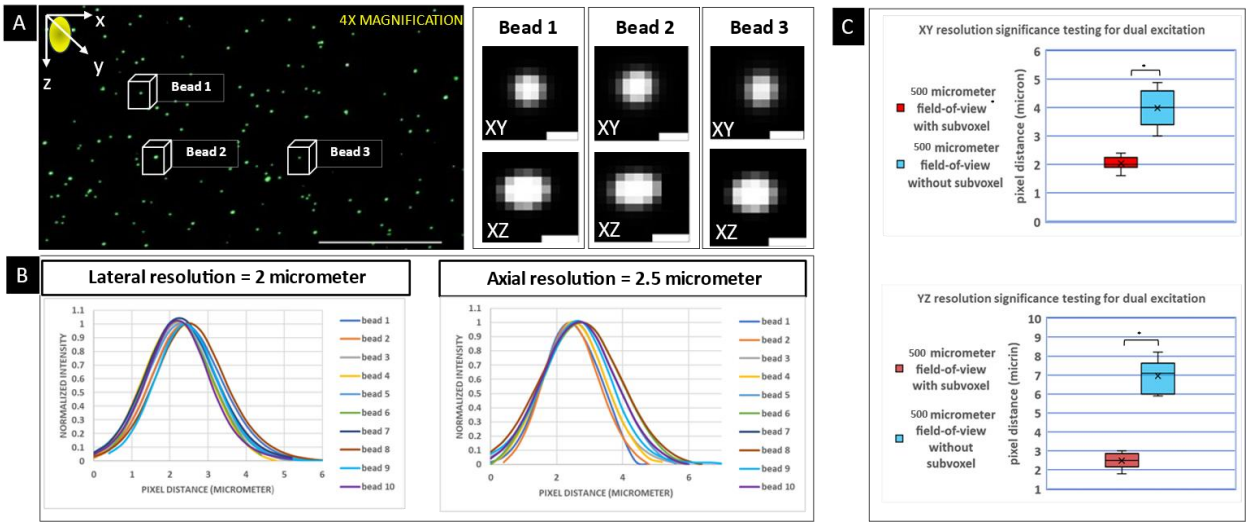

Figure 3.3 Dual illumination light sheet spatial characteristics. (A) Beads inspected at random across the FOV for resolution quantification. (B) Gaussian intensity profiles used to calculate full Width Half Maximum of beads (C) Statistical testing significance for sub voxel and dual illumination light sheet modes

Using the sub voxel, off detection axis sample stage integrated in the system **(Figure 3.1c)**, we sampled n = 10 beads at 0.85-1-micron z – steps (<1/3rd of axial thickness) across the 500 micrometer FOV, like single and dual illumination modes. Further, oblique angle beads were passed through maximum likelihood estimation cost function compensating for image blur and optical resolution degradation factors **(refer Methods).** The sub voxel algorithms models sub stacks containing overlapping information from the original raw 3D stack as separate probability distributions, which are then passed through the algorithm. Consequently, we were able to quantify full width half maximum of 2 microns +/- 0.3

microns in the XY plane and 2.5 microns +/- 0.4 microns in the XY plane **(Figure 3.3b)**. More importantly, we were able to achieve statistically significant reduction of 2x from dual side illumination **(Figure 3.3c)**, (paired t test, n = 10 beads, p value < 0.001 for alpha value at 0.05) and ~3x reduction in axial resolution compared to dual illumination **(Figure 3.3c).**

3.3 DISCUSSION

3.3.1 SIGNIFICANCE

We tested sub voxel light sheet microscopy across various lenses, ranging from 2x magnification (0.25 NA) **(Figure 2.7) (Figure S2.1)** to 4x (0.13 NA). In this study, we were able to achieve XY and YZ resolution of ~2 and 2.5 microns respectively with the 4X detection lens after sub voxel processing, compared to raw microscope resolution of 4 microns and 7.1 microns **(Figure 3.3)**. In this regard, we did not detect significant difference between the XY and XZ resolution of the processed bead **(Figure S2.1)** (paired t test, p = 0.3, n = 10 beads, paired t – test, alpha value = 0.05), with respect to the anisotropic nature of XY and XZ orthogonal profiles of raw microscope resolution **(Figure 3.3)**. Hence, we were able to validate isotropic 3D resolution across 500 micrometer field-of-view. Further, we have quantified XY and YZ resolution of 2.65 and 3.65 microns for 2X detection lens after sub voxel processing (refer chapter 2) **(Figure 2.7), (Figure S3.1)**, compared to raw microscope resolution of ~8 and 17 micron respectively in XY and XZ planes across 4500-micron field-of-view. When we compared the sub voxel beads for

different magnifications (2X and 4X), no significant difference was quantified in the XY resolution between the 2 magnifications across 500 micron and 4500-micron FOV respectively ($p = 0.1$, $n = 10$ beads, unpaired t test, alpha value = 0.05) (Figure S3.1). However, there was significant refuction in axial resolution (Figure S3.1). However, these results provide promising avenues to decouple physical dependance of resolution on lens NA characteristics and thereby enable nanometer resolution for medium NA lenses, while still maintaining medium to high field-of-views. (> 500 micron).

3.4 SUPPLEMENTARY FIGURES

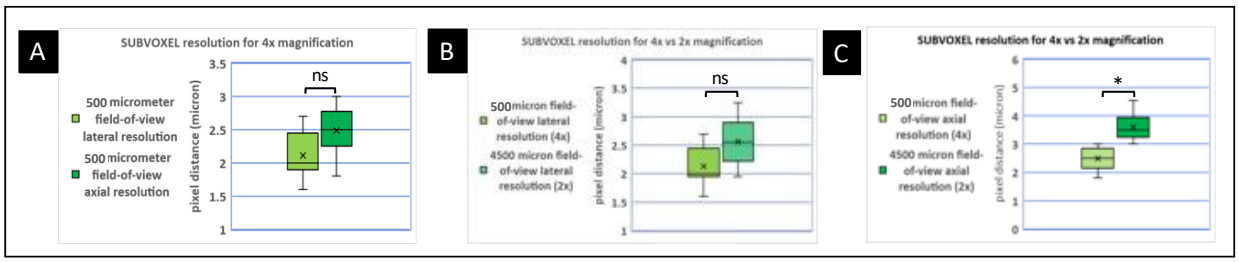

Figure S3.1 Dual illumination light sheet spatial characteristics. (A) Subvoxel XY and YZ resolution testing for 4x magnification (B) 4x magnification lateral resolution vs 2x magnification lateral resolution for sub voxel C) 4x magnification axial resolution vs 2x magnification axial resolution for sub voxel.

CHAPTER 4

CORRECTING ANISOTROPIC INTENSITY IN LIGHT SHEET IMAGES USING DEHAZING AND IMAGE MORPHOLOGY

4.1 INTRODUCTION

For understanding dynamic processes taking place at the cellular and molecular level, it is necessary to perform spatiotemporal volumetric analysis. Among non-invasive imaging modalities, light-sheet fluorescence microscopy (LSFM) is emerging as a powerful tool for studying developmental biology due to its highly advantageous capabilities such as short pixel dwell time while still being able to capture a high dynamic range[4]. However, LSFM images with Gaussian illumination may suffer from limitations in the form of stripe effects and non-homogenous fluorescence intensity due to photon refraction through a heterogeneous scattering medium[4]. Hardware solutions through dual-side and multidirectional selective plane illumination microscopy (mSPIM) have assisted to overcome these issues in conjunction with resonant mirrors[4]. The advent of tissue clearing techniques has also helped to minimize tissue scattering by removing light scattering endogenous pigments and lipid membranes that may otherwise affect the laminar light sheet and cause tissue opacity. In addition, the oblique scanning method facilitated a major advancement in image sub-voxel resolution using a low-power objective lens[3]. Although myriad solutions have been developed, it remains a challenge to obtain an impeccable distinction between the background and foreground due to interference from unfocused fluorescence in the axial direction. Primarily, refractive index mismatch within the tissue and mismatch between the tissue with the embedding medium, cause photon scatter outside the focal volume[4]. This leads to sample blurriness axially and laterally, hindering the accuracy of volumetric reconstruction, and is further exacerbated for a low

numerical aperture (NA) objective lens that has a smaller solid angle limiting photon capture. As a result, underwater imaging requires pre-processing to maintain spatial homogeneity in the reconstructed volume.

Anisotropic intensity correction through intensity distribution approximation, based on scattering propagation models, has been implemented using conventional techniques such as histogram modeling. Such methods effectively increase the intensity dynamic range of an attenuated image, but they are susceptible to saturating bright pixel neighborhoods where evanescent scattered light flux is on the order of 10–100 greater than the incident light field.

Biomedical applications require the critical object in the region of interest (ROI) to be aberration free and unaffected by the ambient medium. The dehazing method based on the dark channel prior (DCP) algorithm is an illumination correction model developed for correcting haze affected images captured in an outdoor environment[33], [34]. In this paper, we applied this method to LSFM images by assuming that the light propagation model is based on the underwater medium instead of air[35]–[37]. Previous studies have indicated that the scattering coefficient of mounting media (water) and atmospheric light propagation is a function of wavelength. For the underwater condition, scattering depends on the dissolved particulate cross-sectional area, whereas the composition of molecular gases determines scattering in the air[37]. Moreover, the dehazing method possesses a high sensitivity to noise as the algorithm corrects attenuation in the aberrated image induced by medium turbidity along the line-of-sight (LOS) propagation.

Translation of the mechanical stage along the depth-of-view (DOV) and lens aberration may result in phase delay or a focal point shift along the optical axis, influencing the diffraction-limited point spread function (PSF) resolution[38]. By assuming depth invariancy, we have attempted to apply the dehazing method to recover the asymmetricity of the PSF intensity distribution[4]. Using this method, we were able to resolve sub-pixel details along DOV (axial domain) and field-of-view (FOV) (lateral domain) without employing a high numerical aperture (NA) lens or using a speckle-based near field aperture projection of the PSF[4].

4.2 METHODS

4.2.1 PREPARATION OF ZEBRAFISH IMAGING [4]

The experiments were performed in compliance the approval from the UT Arlington Institutional Animal Care and Use Committee (IACUC) protocol (#A17.014). The transgenic lines, *Tg(flk:gfp)*, were raised at the UT Arlington Aquatic Animal Core Facility. The flk promoter-driven green fluorescent protein (GFP) from the *Tg(flk:gfp)* zebrafish line was expressed in vascular endothelial and endocardial cells. To maintain transparency of zebrafish embryos, the medium was supplemented with 0.0025% phenylthiourea (PTU) to suppress pigmentation at 20 hours post fertilization (hpf). At 4 dpf, live transgenic zebrafish embryos was anesthetized in 0.05% tricaine, and immersed in 37^{o}C, 0.5 %, low-melt agarose for imaging. Prior to agarose solidification, the embryos with low-melt

agarose were transferred to a fluorinated ethylene propylene (FEP) tube to match refractive index number (1.34) to water (1.33)

4.2.2 IMAGE PROCESSING PIPELINE [4]

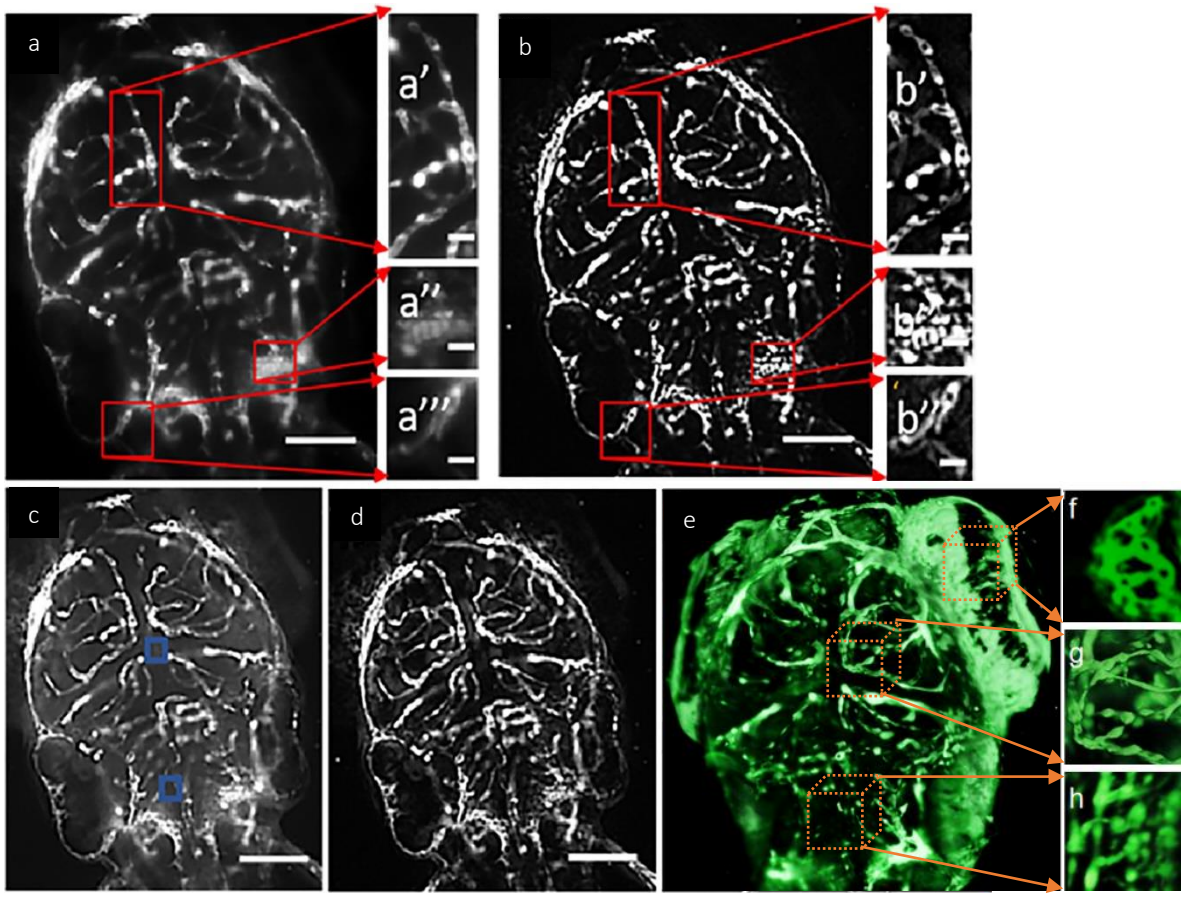

Figure 4.1 Image processing algorithm. (a) Original image with its zoomed in regions of middle mesencephalic central artery (a′), primordial hindbrain channel (a″), and posterior cerebral vein (a‴), respectively. (b) Processed 2D image with its magnified perspective views of highlighted blood vessels (b′, b″, and b‴). (c) After the processed dehazing technique, autofluorescence or tissue scattering has been amplified together with the fluorescent signal.

(d) After dehazing, background subtraction was applied to increase the fluorescent SNR of zebrafish vasculature. (e) Transgenic (fl1:GFP) zebrafish volume expressing green fluorescent protein in vascular endothelium, was reconstructed after image processing. (f-h) represent blood vessels in eyes, dorsal vasculature, and tail [scale bar = 200 μm for (a)–(e) and scale bar = 50 μm and (a′)–(a‴), (b′)–(b‴), (e′), and (e″)]. Blue square: local pixel patch showing autofluorescence.

Observing better lateral resolution as compared to axial resolution, the processing was applied to every individual image slice in the z-stack**.** The dehazing, deconvolution and morphological operations were performed using the imreducehaze (dehazing operation), deconvlucy (point spread function deconvolution) and imtophat and imbothat (morphological operations) functions respectively. We performed the background subtraction method in Fiji and used Amira to reconstruct the z- stack by specifying the voxel size parameters.

The dehazing method tends to amplify autofluorescence of tissue outside the focal plane and as a result hampers the intensity restoration **(Figure 4.1c)**. To avoid this artifact, we performed background subtraction on the dehazed image **(Figure 4.1d)**. Further, we deconvolved the background subtracted image using a dehazed point spread function **(Figure 4.1e, Figure 4.1(e'-e"))**. The deconvolution result is a function of the number of iterations and hence, can introduce random noise. We smoothened the image after deconvolution using a gaussian smoothening filter in MATLAB using the imgaussfilt function or alternatively an edge preserving bilateral smoothening filter in ImageJ ***(Plugins***

> ***Process > Bilateral Filter)***. Both methods produced similar results without any significant change. It is important to adjust the parameters of PSF dehazing and select PSF's along LOS propagation unaffected by spherical aberrations, such that it does not lead to PSF oversampling causing unwanted saturation. The final image **(Figure 4.1b, Figure 4.1(b'-b'"))** was obtained through an image arithmetic operation**:**

(background subtracted dehazed image) – [tophat(background subtracted dehazed image) + bottomhat(dehazed image deconvolved with dehazed point spread function)].

After reconstructing the z -stack by specifying the required voxel arguments, we were able to visualize 3d local morphology across different scales by adjusting the transparency of the volrenGreen color map and the histogram to saturate critical objects in the 3d FOV.

(1) **Dehazing**: The raw images were contrast-corrected using the dehazing method based on the dark channel prior (DCP) algorithm. Image formation achieved by the dehazing algorithm is based on the following model:

$$I(x) = (J(x).t(x) + A\big(1 - t(x)\big)), \quad \text{-(13)}$$

Where I(x) is the hazy image which is a 3D RGB vector of dimension (mxnxl); J(x) is the original scene of irradiance captured by the camera over LOS propagation which is a 3D RGB vector of dimension (mxnxl); A is the ambient light represented by 3D RGB vector of dimension (mxnxl); and t(x) is the light transmission that is unaffected by interference by the ambient surroundings whereby t(x) is a scalar in [0,1] where t(x) = 0 means hazy and t(x) = 1 means haze free image.

(2) Background subtraction: The sliding paraboloid background subtraction filter in Imagej based on the rolling ball averaging algorithm, was used to remove the effect of tissue autofluorescence and lateral light scatter. It is based on image subtraction of an averaged background value for each pixel from the original image by sliding a paraboloid estimated by 4 parabolae in 4 directions: x,y and two 45-degree directions. The recovered image contains gradient refractive index of overlapping tissue represented as an unsigned integer in the 2d image vector. These overlapping spatial variations represented as intensity variations in local pixel neighborhoods can be effectively corrected using background subtraction as it assumes that each pixel intensity on the XY spatial image plane can be imagined as a third dimension with respect to the intensity values of other pixels in the local neighborhood. This is analogous to using non-flat structural elements for the mentioned morphological operations.

(3) **Gaussian blurring filter**: The deconvolution process may result in over-emphasized intensity peaks or unwanted noise amplification. To reduce this effect, we applied the following Gaussian smoothing function:

$$G(x,y) = \frac{1}{2\pi\sigma^2} e^{-\frac{x^2+y^2}{2\sigma 2}} \quad \text{-(14)}$$

where x and y represent the 2D pixel coordinates along x and y image axes respectively; and σ (sigma) is the standard deviation for a 2D isotropic Gaussian convolution kernel. We specifically used the Gaussian smoothing filter, as other filters that replace the pixel values with the weighted average of neighboring pixel

values may pass intensity values that may be beyond the passband (ringing oscillations). This is also because convolution with a smoothing kernel in the spatial image domain is analogous to multiplication in the frequency domain with a low pass frequency filter. Since the value of sigma (σ) determines the degree of smoothing, we used a smaller σ value to maintain a tighter roll-off for the Gaussian function and to avoid excess blurring.

(4) **Morphological transformation**: For greyscale image f and structuring element B:

Image dilation:

$$\delta_B f_{(x,y)} = \max\{f(x-s, y-t) + B(s,t) | (\mathrm{x}-\mathrm{s}), (\mathrm{y}-\mathrm{t}) \in D_f, (s,t) \in D_B \quad \text{-(15)}$$

Image erosion:

$$\epsilon_B f_{(x,y)} = \min\{f(x+s, y+t) - B(s,t) | (x+s), (y+t) \in D_f, (s,t) \in D_B \quad \text{-(16)}$$

where (x,y) and (s,t) are the coordinate sets for greyscale image f and structuring element B, respectively; and D_f and D_B are the respective domains.

The image opening and closing operations are defined as follows:

Image opening: $\gamma_{(B)}(f) = \delta_B(\epsilon_B(f))$

Image closing: $\emptyset_{(B)}(f) = \epsilon_B(\delta_B(f))$

The top hat transform is based on image subtraction of the original image by the opened image. This morphological operation was utilized to restore contrast in uneven illumination along the line of sight (LOS) propagation in this case. Image opening can be defined as image erosion followed by image dilation. The bottom

hat transform was used to emphasize poorly illuminated depth details, and the bottom-hat image was obtained by dilating the image and eroding it. The top hat transform was employed to maintain the size of larger objects and remove smaller discontinuities, whereas the bottom hat transform was used to fill-in smaller regions. For images that were relatively unaffected by any intensity aberrations, we used the opening operation as an alternative to the top hat operation and closing operation instead of bottom hat filtering.

4.3 RESULTS

4.3.1 ANISOTROPIC ILLUMINATION CORRECTION BY INTEGRATING DEHAZING ALGORITHM AND BACKGROUND SUBTRACTION

Even after using a FEP (Fluorinated Ethylene Propylene) tube to match the refractive indices of water and agarose, different regions of the reconstructed zebrafish anatomy suffered from attenuation of light (**Figure 4.2a**). To restore uniform radiance across the attenuated image, we performed dehazing based on the dark channel prior (DCP) algorithm. The dehazing operation restores object radiance at zero the viewing distance while taking into consideration atmospheric light as well as the transmission distance. Hence, it corrects zero intensity crossings of overlapping translucent objects without any loss of information or addition of spurious noise **(Figure 4.2b**).

However, dehazing based on DCP does not consider endogenous fluorescence in the focal plane due to forward scatter due to refractive index mismatch. Therefore, the dehazing method is prone to restoring unrequired background autofluorescence **(Figure S4.2b)**. To

improve our result, we performed background subtraction of the dehazed image using a rolling ball averaging algorithm to isolate the fluorophore tagged vasculature in the image FOV and remove out of focus objects in the image plane (**Figure 4.2b,4.3d).**

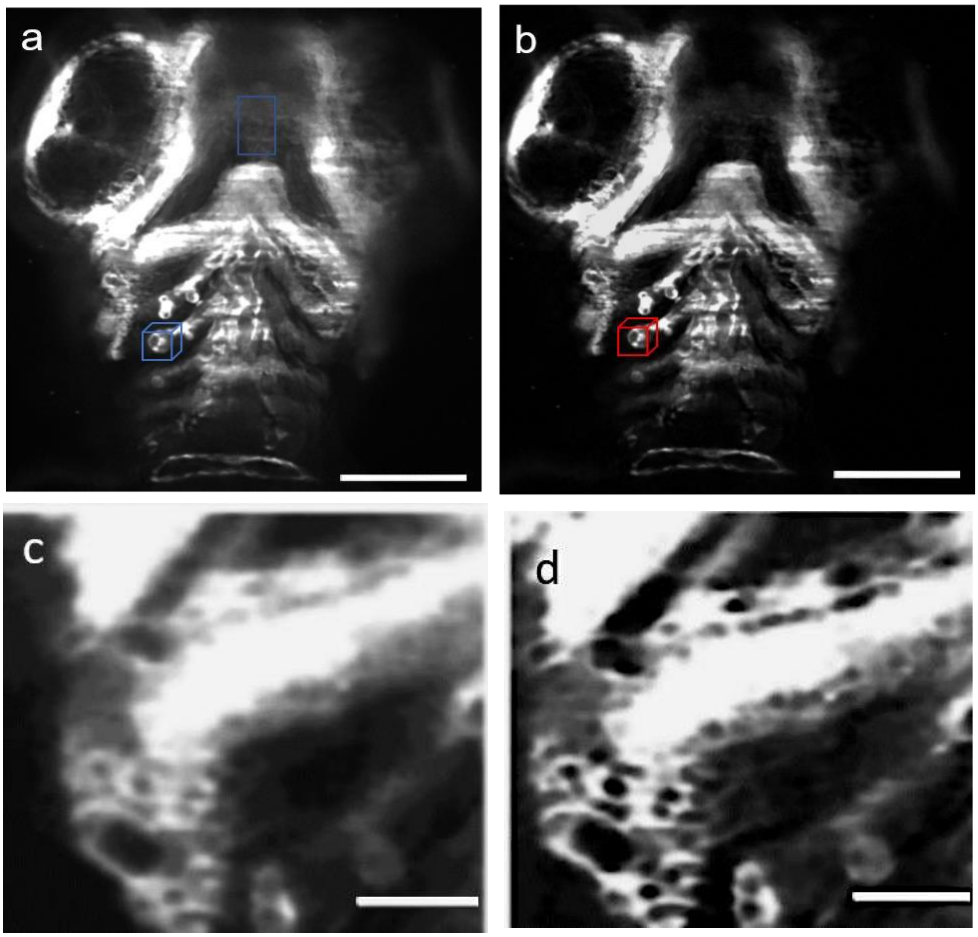

Figure 4.2. Image enhancement results for an attenuated light-sheet illumination. **(a)** Single side illumination LSM 2D image (b) To negate effects of endogenous autofluorescence, we implemented dehazing algorithm in conjunction with background subtraction. (c) Blurred and attenuated zebrafish pharyngeal/aortic arch due to non-homogenous propagation medium (d) Using dehazing algorithm, we were able to get rid of endogenous autofluorescence, (Scale bar for a and b = 200 um), (Scale bar for c and d = 30 μm)

4.3.2 USING ISOTROPIC STRUCTURING ELEMENT TO RESOLVE EDGE FEATURES

The final step in the post processing pipeline compromises top-hat and bottom-hat morphological transforms based on image opening and closing, to accurately resolve overlapping features and edge discontinuities. After obtaining the deconvolved image **(Figure S1c),** we applied the top-hat transform to the dehazed image **(Figure S3.1).** The top-hat transform is based on image erosion, which is utilized to remove weakly connected regions of interest (ROI), and image dilation to emphasize and fill-in image boundaries, in that order. Top-hat transform assists by removing any pixel discontinuities induced by background subtraction and effectively isolates foreground objects in the image plane. The bottom-hat transform is based on image closing to reinforce depth details which are blurred-out and out-of-focus due to autofluorescence affecting the axial resolution. The final image was reconstructed by adding the image subtraction of the top-hat and bottom-hat transform results to the dehazed image.

4.3.3 EVALUATION PARAMETER OF IMAGE RESTORATION

For quality assessment, calculated the peak signal to noise ratio (PSNR) to understand improvement in terms of noise reduction post processing **(Figure S3.3).** Mean PSNR for an entire 3d stack was calculated by summing the peak signal value of individual 2D slices. Due to noncompliance with normality ($p=0.01$, alpha value threshold = 0.05), independent T test assuming unequal variances was performed to check significance with alpha value

threshold at 0.05. **We** observed significant difference between PSNR for processed image and unprocessed image across n=10 zebrafish 3D volumes (**Figure S3.3)** ($p = 0.015$), with higher value reflecting less noise. Moreover, we also quantified similarity index (SSIM) using a histogram adjusted raw image as reference. The lower/upper 10 percent of intensity distribution was saturated to enhance under exposed structures. Using the reference image, we compared the loss/degradation by our proposed method using dehazing followed by background subtraction for comparison**.** We plotted the local SSIM maps, based on per-pixel value, and calculated the global SSIM value as well. The processed 3D volumes scored mean value of 0.78, while histogram normalized image scored 0.83 on the global SSIM value (No significant difference was observed in structural similarity index between both methods ($p = 0.07$).

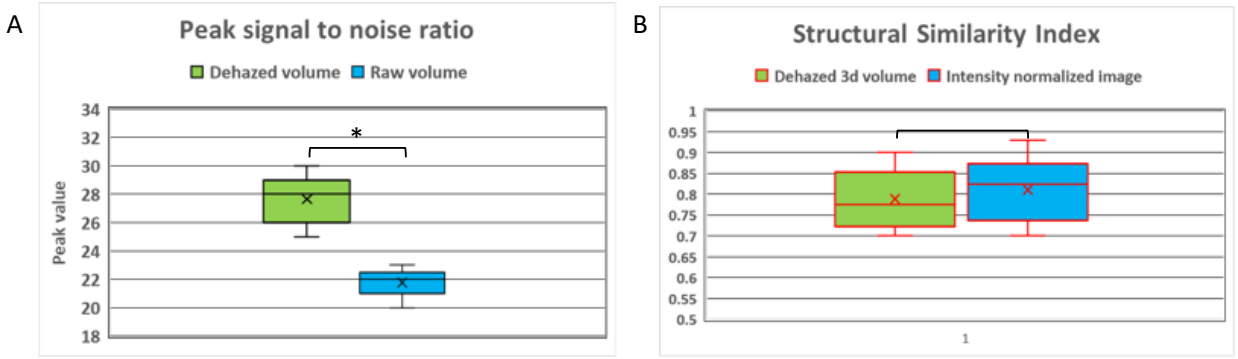

Figure 4.3. (A) Peak Signal to noise ratio in decibel (B) Structural similarity index is an image metric based on contrast, luminance, and structural information, with 1 representing highest score with reference to similarity with reference volume.

4.4 DISCUSSION

4.4.1 SIGNIFICANCE

We demonstrated the applicability of DCP algorithm for restoring isotropic intensity in the FOV and morphological operations for correcting diffraction-limited volumes with non-homogenous spatial homogeneity. We observed some intrinsic limitations in the single/dual side LSFM images acquired at the detection focal plane that affected isotropic reconstruction of the z stack[3]. The images composed of local pixel patches were innately high in photon count with reduced visibility**.** For this study, we assumed scattered wavelengths in these regions are longer than the excitation wavelengths as seen in Raman stokes scattering and are non-propagating[39]. This light scatter spreads laterally across the tissue but does not participate in the far field image formation. It decays evanescently in a direction perpendicular to the surface with the intensity distribution being amplified by an order of 10-100 in the evanescent field region. Coupled with a laser intensity beyond a certain threshold, it can cause optical distortions for any particulates that are less than half the input wavelength. As a result, out of focus tissue planes in the evanescent light field are illuminated[40], [41]. Due to this limitation, dull/low light patches with relatively uniform colocalized zero intensity crossings appear saturated due to over estimation of haze thickness.

The capability of an interrogating light sheet to illuminate the sample and the ability of the emitted light to escape the sample and reach the detection camera, constitute important factors for determining image resolution**.** Using a low NA focusing objective can compromise the excitation efficiency of the focused beam waist. As LSFM involves light

propagation through media with differing refractive indices, it is also necessary to develop or select intensity correction algorithms that account for these changes in optical properties of the media. Even when refractive index mismatch between the FEP tube and mounting media is neglected, light scattering occurs due to variation in tissue refractive indices. Tissue birefringence due to tissue refractive index, is a function of the density resulting in a gradient refractive index.

Tissue transparency in animals is a function of surface irregularities at the cellular/molecular level that affect the potential of tissue to reflect light. Using the Weber formula for defining contrast (Cd) of a transparent animal [4]

$$Cd = ((Ld - Lb)/ Lb); \quad -(17)$$

where *Ld* is the radiance of the object viewed at a distance in the underwater medium, and *Lb* is the background radiance.

$$Ld = (Lo e^{-cd} + Lb(1-e^{-cd})); \quad -(18)$$

where *Lo* is the inherent radiance at zero viewing distance, *c* is the beam attenuation coefficient (wavelength is a function of the depth), and *d* is the distance of the object to the viewer. Here, the detected object radiance (*Ld*) depends on object irradiance at the point of focus and the effect of atmospheric light scatter along the LOS. As we are using along working distance air lens with low NA, we can infer from the above equation that as the viewing distance is increased, inherent object radiance will decrease, and the scattered light (*Lb*) will dominate.

For a transparent animal, the inherent radiance consists of two parts: namely the background radiance that is transmitted through the animal, and the light scattered towards the viewer; and hence.

$$\mathrm{Ld} = (\mathrm{LbT}e^{-cd} + \mathrm{LdS}e^{-cd} + \mathrm{Lb}(1\text{-}e^{-cd}))^{28}; \quad \text{-(19)}$$

Where *T* represents transmission through the animal and *S* is a fraction of the environmental light scattered to the observer.

Comparing Weber formula equation with the Dehazing equation (13),

$$I(x) = J(x).t(x) + A\big(1 - t(x)\big), \quad \text{-(20)}$$

Where I(x) is the hazy image which is a 3D RGB vector of dimension (mxnxl); J(x) is the original scene of irradiance captured by the camera over LOS propagation which is a 3D RGB vector of dimension (mxnxl); A is the ambient light represented by 3D RGB vector of dimension (mxnxl); and t(x) is the light transmission that is unaffected by interference by the ambient surroundings whereby t(x) is a scalar in [0,1] where t(x) = 0 means hazy and t(x) = 1 means haze free image. Therefore, we infer the DCP method does not consider the background radiance, *Lb*, that is transmitted through the illuminated portion, *T*, of the object. To counter this problem, we performed the background subtraction operation on the dehazed image to remove innately present autofluorescence in the surrounding tissue. Fluorescent images captured at higher frame rates suffer from poor distinction between the fluorescently tagged marker and background noise. To further elucidate depth details and separate overlapping edges, we used top-hat and bottom-hat morphological transforms

based on flat structuring elements. As morphological operations are non-linear operations based on spatial ordering of the pixel coordinates and not the pixel intensity values, these methods can be applied efficaciously to greyscale turbid media images. To maintain isotropic kernel convolution values in all directions, we used a sphere-shaped structuring element that was greater than the smallest region-of-interest (ROI) for all the morphological operations.

As the PSF of diffraction-limited microscopy is depth and space invariant with respect to the detection optic axis, we applied the dehazing algorithm as a PSF intensity correction model. An intensity correction of the recorded emission intensity for a fixed dipole, or fluorescent bead, was implemented by assuming that the intensity will vary according to the random orientation of the bead**.** Assuming anisotropic photon collection efficiency, the intensity will experience a higher degree of exponential decay for long working distance objective lenses.

4.4.2 CONCLUSION AND LIMITATIONS

In summary, with the help of our image processing we were able to overcome intrinsic LSFM limitations and significantly improve anisotropic intensity across turbid Field-of-view. The dehazing model was used to enhance subdued intensity peaks and thus restore attenuation caused due to propagation through an opaque medium or light sheet skew. Using morphological operators, we were able to localize peaks and valleys in the local image structure to resolve diffraction limited structures affected by light scatter or stripe artefacts. At the same time, we were able to capitalize on the advantages provided by the LSFM modality, namely the wide FOV provided by the low NA infinity corrected objective lens and acquire zebrafish z-stacks with short acquisition time. This research will benefit *in vivo* developmental biology studies, visualized using fluorescence modalities that require accurate volumetric reconstruction for further analysis. However, dehazing algorithm is prone to bleaching pixel spots that are inherently saturated by the laser. Moreover, it is susceptible amplify tissue refractive index mismatch as quantified in the peak signal-noise ratio plot.

\

4.5 SUPPLMENTARY FIGURES

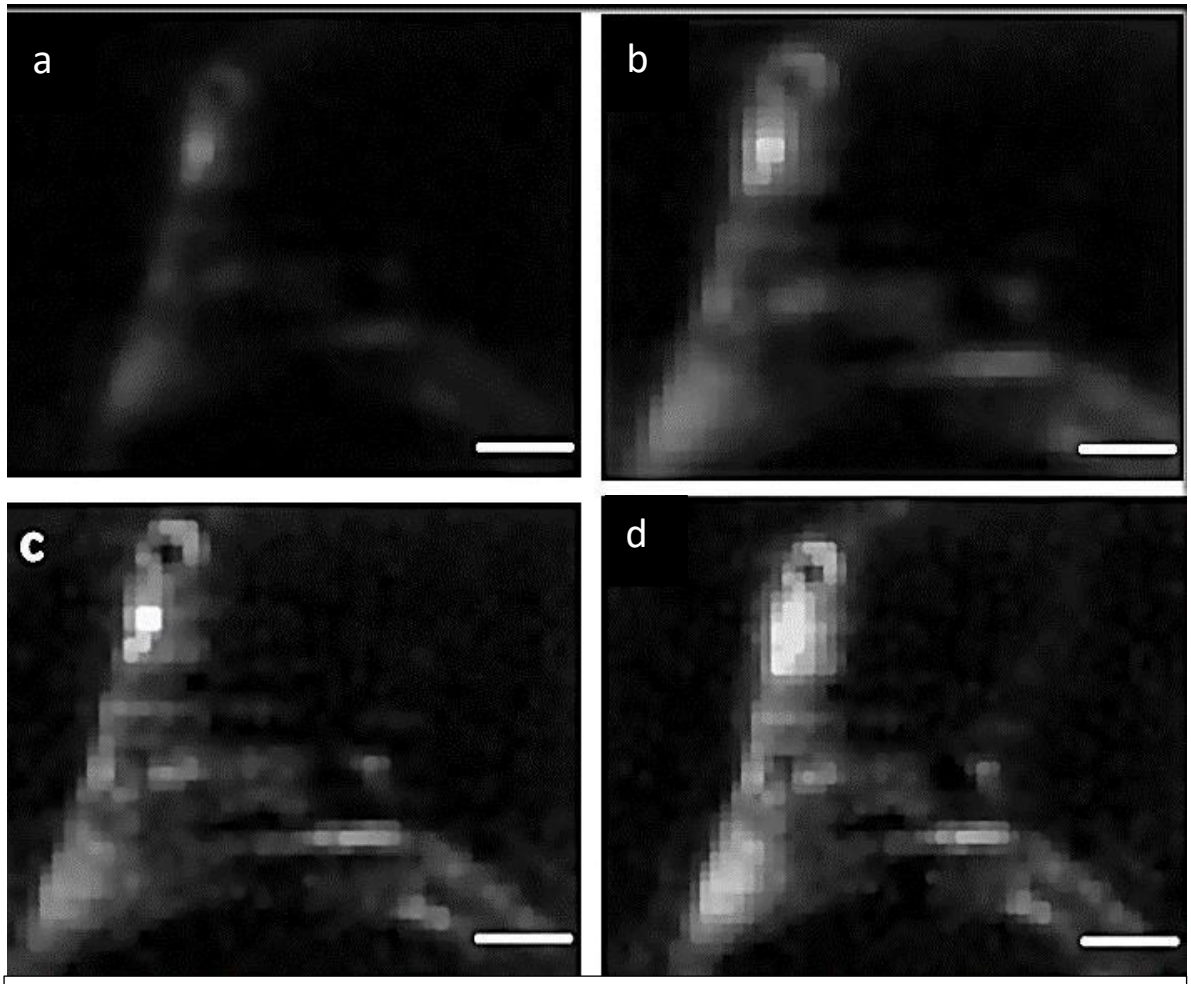

Figure S4.1. Restoring contrast uniformity in zebrafish trunk vasculature (a) Raw image. (b) Background subtracted dehazed image. (c) Dehazed image after bead deconvolution, (d). Top-hat and bottom-hat filtering performed on the image (c). (Scale bar = 20 μm.)

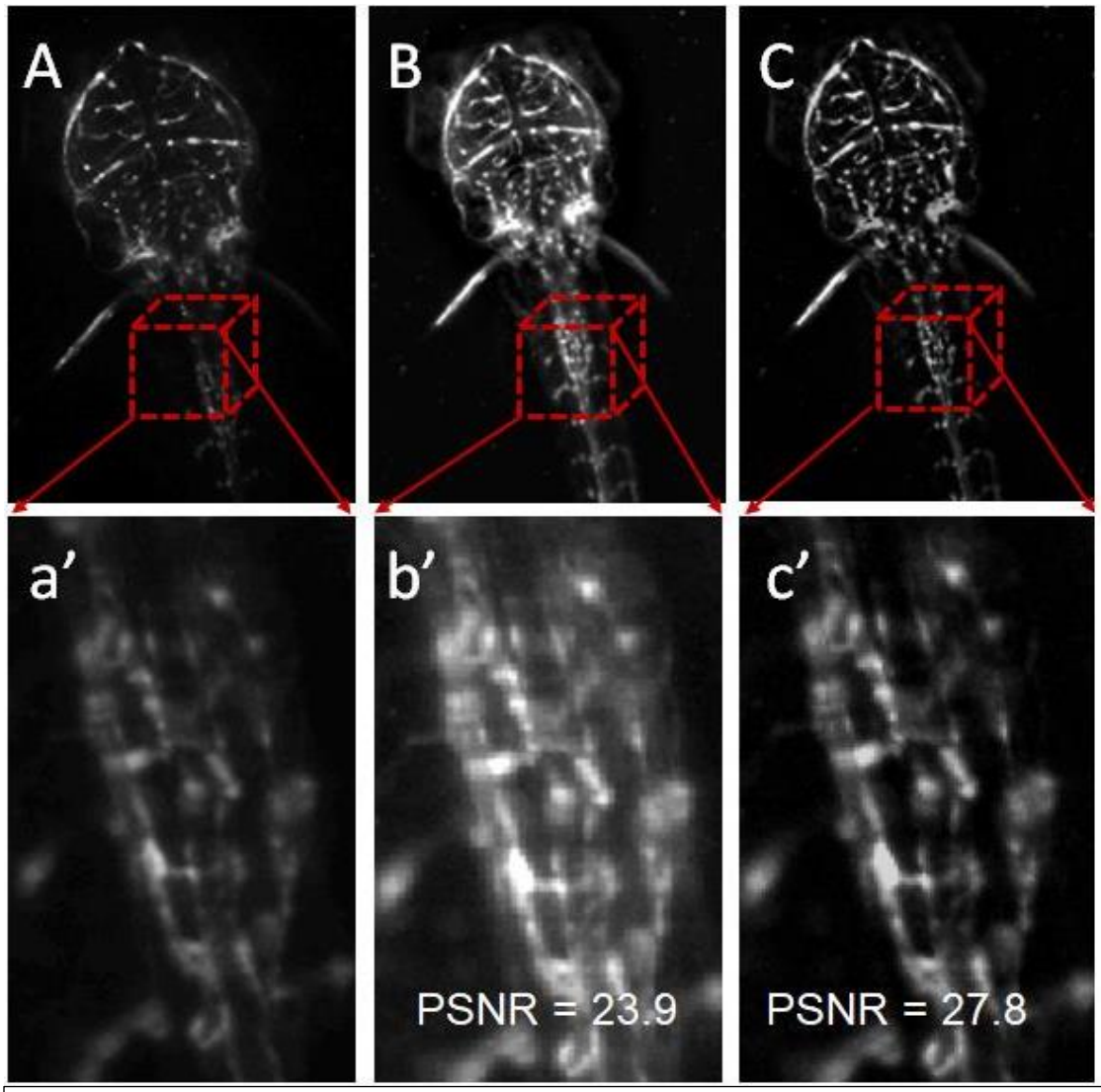

Figure S4.2. Peak Signal-to-Noise (SNR) evaluation. (a) Raw image and (a') is the magnified region in the red box. (b) Dehazed image without background subtraction and (b') is the magnified perspective of the tail. (c) Background subtracted dehazed image and (c') is the magnified region of the red box. Using the raw oblique scanned image(a) for reference, we quantified the PSNR for (b, b'), (c, c') and observed that the dehazed image after background subtraction (C, c') has a higher PSNR.

CHAPTER 5

DEVELOPMENT OF 3D+TIME LIGHT SHEET IMAGING PIPELINE TO RECONSTRUCT AND ANALYZE DYANAMIC NUCLEI IN EMBRYONIC ZEBRAFISH

5.1 INTRODUCTION

The evolution of optical microscopy has resulted in a high volume of image attributes with differing degrees of complexities[42]. The consequence is a grueling effort to validate the interpretation and reliability of a biomarker-based study[29], [43], [44]. Moreover, manual analysis often leads to inconsistencies in the generalization of biomarker studies due to the incredible number of target features compared to sampling size in clinical images. In this regard, feature detection methods help refine data dimensionality by discarding dispensable attributes, thereby producing a more compact feature space[45], [46].

In biomedical research, endogenous fluorescent signals are commonly used to study *in vivo* spatiotemporal organogenesis. However, optical microscopy inherently suffers from anisotropic illumination in the optical image plane[4]. This anisotropy is due to aberrations caused by photon propagation through heterogeneous tissue morphology or significantly varied sample size; hence, optimization of image acquisition parameters is a challenging task. Precise orchestration of any volumetric reconstruction analysis requires high feature detection sensitivity with respect to tissue protrusions and changes in illumination, rotation, local scaling changes, and motion translation. These optical aberrations are prone to induce redundancy in image features, rendering the task of manual feature extraction intrinsically subjective and laborious[7]. Hence, feature detection has gained popularity for augmenting performance of downstream classifiers or regression estimators to improve their interpretability and accuracy[16], [45], [46].

Quantitative zebrafish cardiomyocyte proliferation studies involving embryonic heart volumetric reconstruction, have reported strict regulation of cell size and proliferation rate for normal heart maturation and chamber formation[47]–[49]. Moreover, previous studies have shown hypertrophy in cell size due to older cell differentiation or migration into smaller-sized cardiomyocytes[50]. With recent progress in Light Sheet Fluorescence Microscopy (LSFM), it is possible to perform *in vivo* 4D (3D + time) cardiac cell tracking and perform mechano-transduction studies[8], [51]–[53]. When this method is employed using transgenic zebrafish, optical sections at different tissue depths are acquired to understand the cardiac architecture. However, quantifying *in vivo* cardiac biomechanics remains a challenging task due to improper focus induced by sample movement or sampling artifacts.

Currently, many studies use manual boundary demarcation due to the limited availability of binary classification methods impervious to heterogenous contrast resolution. Traditionally intensity-based segmentation methods such as the Otsu's method, adaptive thresholding, iso data thresholding, and entropy-based thresholding have been used for automated cell tracking for their simplicity and speed[54]. However, these methods are infamous for poor performance in the presence of noise and hence incapable of separating objects in proximity into meaningful biological regions. Consequently, all the thresholding techniques mentioned above suffer in cell detection performance and cannot perceive separate events at different scales, arising from separate biological processes. Additionally, noise due to optical aberrations, short exposure time, cells entering and leaving the field of

view and insufficient contrast between adjacent cells may all diminish the technique's performance.

Another conventionally favored approach for cell isolation involves the watershed algorithm[55], [56]. However, the technique is fraught with over-segmentation or false detection of non-existent objects in the presence of noise or complex cell morphology. Hence, to suppress noise and reduce the number of false positives with respect to detected cell count after binarization, we used the difference of Gaussian (DoG) scale-space as a pre-processing strategy before contour detection by the Hessian difference of Gaussian (HDoG) operation[57]–[61]. However, the DoG band-pass operation can induce under-detection of features due to suppression of high frequency noise. Consequently, we performed local curvature evaluation from the Hessian matrix in conjunction with DoG detector, for precise cardiomyocyte nuclei boundary analysis and localizing individual nuclei volumes[62].

Using the Hessian Difference of Gaussian scale space detector in conjunction with the watershed algorithm, we were able to quantify a statistically significant increase in cardiomyocyte nuclei count across distinct developmental stages.
This study focuses on the merits of scale space feature detection framework and demonstrates its efficacy for cell tracking and multidimensional volume deformation[14], [63].

5.2 MATERIALS AND METHODS

5.2.1 LIGHT SHEET MICROSCOPE (LSFM) IMPLEMENTATION [44]

Our home built light sheet microscope consists of a single-side excitation pathway and a custom water dipping lens (20x/0.5 NA UMPlanFL N, Olympus, Tokyo, Japan) detection. In the illumination pathway, a cylindrical lens (LJ1695RM, Thorlabs) coupled with a 4x objective lens (4X Plan Apochromat Plan N, Olympus, Tokyo, Japan), are used to collimate a cylindrical light-sheet with ~4-5-micron thickness. Furthermore, a mechanical slit aperture (VA100C, Thorlabs) is modulated across distinct developmental stages (48-,72-,96- and 120 hpf), to accommodate ventricular circumferential extent across the light sheet confocal regiN. A DC servo motor actuator (Z825B, Thorlabs) is used for sample translation in the axial direction (z-step velocity and acceleration = 0.005 mm/s). The optical detection pathway consisting of the water lens, infinity corrected tube lens (TTL 180-A, Thorlabs) and sCMOS camera (ORCA flash 4.0, Hamamatsu, Japan, camera pixel size = [6.5 (um)^2] = [6.5/20x = 0.325 um], camera exposure time = 30–50 ms), is used for non-gated 4D (3D + time) cardiac volume acquisition.

As the zebrafish ventricle undergoes periodic deformation during peak systole to end diastole, optical sections were acquired at varying depths in the sample, covering 4–5 cardiac cycles. Since triggering of image slices is not synchronized to a particular phase in the cardiac cycle, we performed volumetric reconstruction a posteriori to ensure alignment of adjacent optical sections. For this purpose, we estimated the period of each individual

cycle by minimization of the least squares intensity difference criterion and calculated the relative period shift to ensure synchronization between independent cardiac cycles.

5.2.2 PREPARATION OF ZEBRAFISH FOR ASSESSING CARDIAC FUNCTION [44]

The animal experiments were performed in agreement with the UT Arlington Institutional Animal Care and Use Committee (IACUC) protocol (#A17.014). The transgenic zebrafish line used in this particular study is the *Tg*(*cmlc2*:*nucGFP*), with the cardiomyocyte nuclei labeled with GFP (Green Fluorescent Protein). The zebrafish embryos were maintained at 28.5°C in system water at the UT Arlington Aquatic Animal Core Facility. 0.0025% 1-phenyl 2-thoiurea was added to the embryo medium starting at 20–24 hpf to suppress pigmentation. Prior to imaging, embryos were anesthetized in 0.05% tricaine (MS 222, E10521, Sigma-Aldrich, St-Louis, MO) to avoid sample movement. Upon administering the anesthetic, alive embryos were embedded in 0.5% low-melt agarose gel inside a fluorinated ethylene propylene (FEP) tube (1677L, IDEX, Chicago,IL). Furthermore, the FEP tube was suspended in water within a custom 3days printed ABS (Acrylonitrile Butadiene Styrene) cuvette (designed using solid works) housing the water dipping lens, to ensure near isotropic refractive index between the water dipping lens and sample inside the tube. (Refractive index of water = 1.33, refractive index of agarose and FEP tube = 1.34). Refractive index matching is necessary to avoid distortions and intensity attenuation in the optical sections.

5.2.3 IMAGE PROCESSING FRAMEWORK [7]

Haze removal using the dark channel prior (DCP) method.

Introduction of haze by the ambient medium or scattering due to particulate matter, degrades the performance of computer vision task. A haze free image can be retrieved by using the image degradation model based on the Dark Channel Prior (DCP) algorithm.

$$I(x) = J(x).t(x)+A(1-t(x)) \quad \text{-(21)}$$

Where I(x) is the hazy image which is a 3D RGB vector of dimension (mxnxl); J(x) is the original scene of irradiance captured by the camera over LOS propagation which is a 3D RGB vector of dimension (mxnxl); A is the ambient light represented by 3D RGB vector of dimension (mxnxl); and t(x) is the light transmission that is unaffected by interference by the ambient surroundings whereby t(x) is a scalar in [0,1] where t(x) = 0 means hazy and t(x) = 1 means haze free image. Using the dehazing algorithm, we estimated the intensity transmission map t(x) using the imreducehaze() MATLAB function.

$$t(x) = e-\beta d(x) \quad \text{-(22)}$$

where β represents the scattering coefficient and d represents the scene depth. t(x) is a 2D scalar in [0,1]. We used the estimated intensity transmission map as a preprocessing step before performing the DoG operation. By estimating the contrast attenuation with respect to distance, we were able to emphasize edges. All processing was performed with respect to 2D slices.

Precise contour delineation using the hessian scale space representation and watershed algorithm.

The hessian scale space representation can be obtained by

$$H_m(x,y) = \begin{pmatrix} \frac{\partial^2 IM}{\partial x^2} & \frac{\partial^2 IM}{\partial xy} \\ \frac{\partial^2 IM}{\partial xy} & \frac{\partial^2 IM}{\partial y^2} \end{pmatrix}. \quad \text{-(23)}$$

$$H(x,y) = \begin{cases} \det H_m(x,y) & \det H_m < 0 \\ 0 & \det H_m \geq 0 \end{cases}. \quad \text{-(24)}$$

Where H(x,y) denotes the saddle point of the image, IM(x,y) demotes 2D position of pixels.

The workflow involved for the hessian blob involves

1) Computing the absolute magnitude of the intensity gradient image obtained by convolving the DoG bandpass image with the derivative of Gaussian filter.

2) Computing the double derivative of the absolute magnitude image calculated in the previous step

3) Imposing boundary conditions on the hessian determinant value [det D(x,y,t) < 0] at every pixel, for indicating saddle points.

4)The image arithmetic operation (OR – operation) results in the union of the DoG localized intensity maxima and contour information from the Hessian blob, aiding the successful splitting of nuclei.

Preprocessing strategies

Images corrupted by noise or tissue scatter, were filtered by using a Gaussian kernel with an appropriate SD followed by the background subtract operation in ImageJ.

5.2.4 CELL COUNTING

After converting raw optical images to binary images, we performed cardiomyocyte nuclei counting and their area analysis by using the 3D object counter plugin in ImageJ. The plugin can be accessed by: ImageJ – Analyze – 3D Object Counter. After cropping the ROI (ventricle in this case), we used the plugin to quantify number of 3D nuclei objects in the ventricular stack. The plugin can also be used to retrieve the centroid geometric coordinates of object volumes. The user is required configure 2 important parameters namely, (a) intensity threshold to separate background and foreground pixel populations and (b) size threshold to exclude smaller objects from the analysis. The plugin allows user to configure object counting based on the presence or absence of touching edges.

5.2.5 STATISTICAL TREATMENT

For nuclei count analysis, we performed pairwise comparisons of n = 10 3D zebrafish volumes sampled from systole to diastole, for distinct stages of heart maturation (p value = 0.05). Additionally, we cleaned the data in excel utilizing Chauvenet's criterion to determine which values were outliers and should be removed. After removing outliers and cleaning the datasets in excel to reduce the chance of error due to our sampling technique, we compared the data with one-way ANOVA. If we detected a statistically significant

difference for any comparison, we performed Tukey's test for multiple comparison of means. For segmentation accuracy evaluation, t test assuming unequal variances was performed with alpha value = 0.05. To test segmentation accuracy, we considered significant difference in major axis (longest axis) of nuclei ellipsoid shape, (surrogate for smallest nuclei to be detected in XY plane) for hessian vs manually segmented datasets as reference. Areas of n = 15 nuclei 3D volumes from 3 days post fertilization dataset were quantified from outer portion and inner portion of zebrafish ventricle respectively. All values herein are reported as mean +/− standard deviation in the figures and respective figure legends.

5.3. RESULTS

5.3.1 APPLYING HESSIAN DIFFERENCE OF GAUSSIAN (HDOG) TO SEGMENT CARDIOMYOCYTE NUCLEI FROM DENSE ENVIRONMENT

Compared to pinhole-based microscopy techniques, a potential cause of concern for LSFM modality manifests in the form of background contrast between adjacent cardiomyocytes **(Figure 5.1(B-C)).** As nuclei move dynamically across the field of view (FOV), undesired fluorescence emitted from fluorophore-binding sites outside the optical section beam waist affects accurate volumetric reconstruction **(Figure 5.1A)**. Furthermore, intensity attenuation caused by low numerical aperture (NA) objectives aggravates poor signal-to-noise ratio (SNR), causing merged nuclei.

To combat this, we applied the Hessian difference of Gaussian detector (HDoG) in combination with the watershed algorithm, for accurate contour separation and assessing the morphology of wild-type myocardial nuclei *in vivo* **(Figure 5.1 (D-E)).** The hessian determinant was used to localize saddle points. Saddle points can be defined as neither an intensity maximum nor minimum, that represent connecting nuclei edges. This approach improved detection sensitivity in the presence of multiple intensity peaks for a single biomarker, and segmented nuclei were further quantified across distinct developmental stages **(Figure S5.1)**.

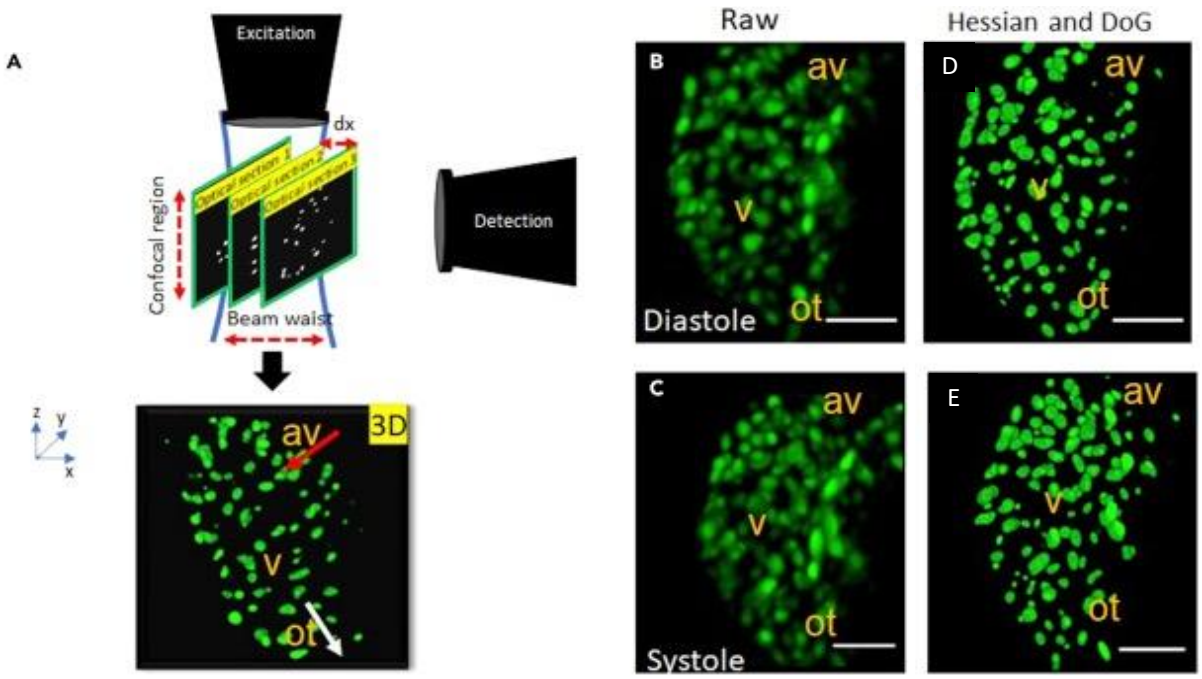

Figure 5.1(A) Illustration depicting zebrafish ventricular myocardial nuclei sections, scanned by a Gaussian light sheet (blue solid line). Samples are scanned through the static optical section at discrete increments (dx) using mechanical transducers, to reconstruct complete *in vivo* 3days + time volumes from individual sections. Red arrow represents the blood flow direction of zebrafish heart. (B and C) Raw systolic and diastolic nuclei reconstruction at 96 h (about 4 days) post fertilization, consisted of closely packed nuclei blobs as compared to 48 h postfertilization. Inaccurate nuclei localization is further exacerbated by dynamic contraction and relaxation. (D and E) Hessian DoG feature detector exhibits improved sensitivity to local affine transformations experienced by nuclei pixel neighborhoods during image acquisition. (scale bar = 50 micron), av: atrioventricular canal, v: ventricle, ot: outflow tract.

5.3.2 NUCLEI COUNTING FOR MATURING HEART AND SEGMENTATION ACCURACY EVALUATION

The average values for number of nuclei in a developing zebrafish heart were quantified as 159 ± 13, 222 ± 17, 260 ± 13, and 284 ± 10 for 48, 72, 96, and 120 hours post birth, suggesting heart maturation with significant increase in nuclei count at distinct stages **(Figure 5.2, Figure S5.3, Table 5.1) (n = 50 nuclei across 2 zebrafish samples per day).** This is in accordance with previously established results for cardiomyocyte count in embryonic zebrafish using confocal microscopy and other multi-dimensional modalities[28], [64]. More importantly, this study validates our multi-dimensional imaging and cell tracking pipeline. To evaluate the accuracy of our segmentation results, we calculated major axes areas for nuclei ellipsoids in the outer ventricular bulge and inner ventricular bulge respectively. At 3 days post fertilization, we started observing distinct rod and circular shapes of nuclei localized in these outer and inner ventricular curvature regions respectively **(Figure 5.2)**. Hence, to test the structural integrity of our binarized labels and accuracy of nuclei count, we decided to test segmentation performance for these different nuclei shapes. We did not observe any significant differences for major axes of nuclei in inner curvature ($p = 0.17$, $n = 15$, standard deviation = +/- 0.2 um) and outer curvature ($p = 0.2$, $n = 15$, standard deviation = +/- 0.11 um), between our auto segmented and manually segmented labels respectively **(Figure 5.2A(iii), B(iii))**. Thereby indicating our feature detection framework did not produce spurious results, resulting in over estimation or underestimation of nuclei **(Figure S5.1).**

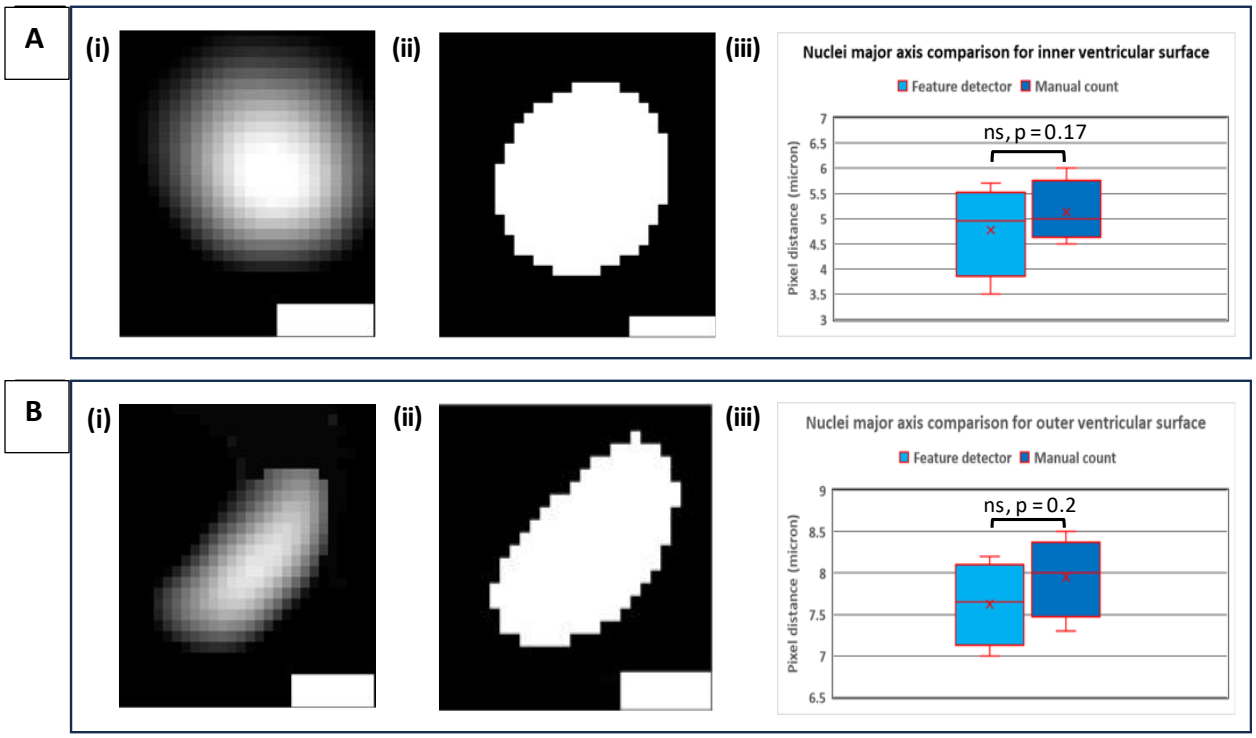

Figure 5.2. Nuclei segmentation accuracy evaluation. (A) (i) represents the manually segmented 2D nuclei slice from inner curvature, (ii) represents hessian segmented nuclei binarized label slice from inner curvature (iii) We tested major axis of nuclei ellipsoid shape (length of longest axis) for both using t – test. X represents mean in box & whiskers plot. (B) (i) represents rod shaped manually segmented 2d slice in outer ventricular bulge and (ii) represents the segmented label. (iii) We tested the major axes of both (i) and (ii) respectively across the cardiac cycle to test under/over segmentation.

5.4 DISCUSSION

5.4.1 SIGNIFICANCE

In this study, we evaluated a novel approach based on well-established methods for robust biomarker edge detection. We successfully quantified the zebrafish ventricular myocardial contractility using the segmented nuclei at distinct developmental phases **(Figure S5.2).** Moreover, our improved HDoG edge detection framework provides direct access to surface area and volume measurements of fluorescently labeled cardiac nuclei to report accurate cell morphology characteristics **(Figure 5.2)**. Although we induced transparency in the zebrafish embryos, tissue birefringence causes heterogeneous refractive index affecting incoming light sheet's tissue penetration ability. Taking this into consideration, we sought to design a feature detector that would provide robust performance for cardiomyocyte nuclei detection accuracy with respect to 1) dynamic volume contraction, 2) single local maxima generation for a true biomarker by Hessian, and 3) localization of segment to the nuclei center by DoG. Other framework design constraints involved consistency in feature detection with respect to illumination, scale (nuclei area heterogeneity) and rotation invariance. Previously conducted studies have reported the use of Laplacian of Gaussian (LoG) and Difference of Gaussian (DoG) feature detectors for efficiently separating individual cell proliferation from a dense environment[58]. Thus, we successfully implemented the computationally inexpensive DoG as a Gaussian filter based tunable bandpass operation in conjunction with the hessian DoG algorithm. Moreover, the DoG filter also functions as a greyscale edge enhancement algorithm, that is useful for images

experiencing refocus. From our analysis, the blob detection framework can handle the varying nuclei orientation and heterogenous nuclei sizes. Our binary thresholding method used for separating touching nuclei will prove beneficial not only for counting the varying number of cardiomyocytes, but also quantifying geometrical shape characteristics of cells that are often required to validate cell studies. Additionally, analyzing the distinct cardiomyocyte motion in 3D will enable quantification of biomechanics such as local deformation to understand mechanotransduction during cardio genesis.

In summary, we have presented a blob detection approach for segmenting a dense nuclear network, with individual nuclei exhibiting distinct morphological characteristics. DoG blob detection followed by boundary segmentation using the watershed algorithm is insufficient for precise contour description of the touching cardiac myocyte nuclei edges. Undesirable computational inconsistencies are induced due to inability of filter response to localize multiple intensity peaks in the same ROI. Hence, to avoid nuclei undercount and inaccurate volume measurement, we combined the DoG and Hessian scale space representation prior to intensity thresholding. Our blob detection framework provided robust performance for images corrupted with noise with insufficient depth detail. Furthermore, the study highlights application of LSM as a bona – fide multi-dimensional, preclinical imaging pipeline with high spatio-temporal resolution, as we were able to sample dynamic cells as small as 5-6 microns at frame rates of 20- 30 ms. However, cells moving outside the confocal region or optical section thickness, during dynamic heart movement were susceptible to being merged even after blob detection.

5.5 SUPPLEMENTARY FIGURES

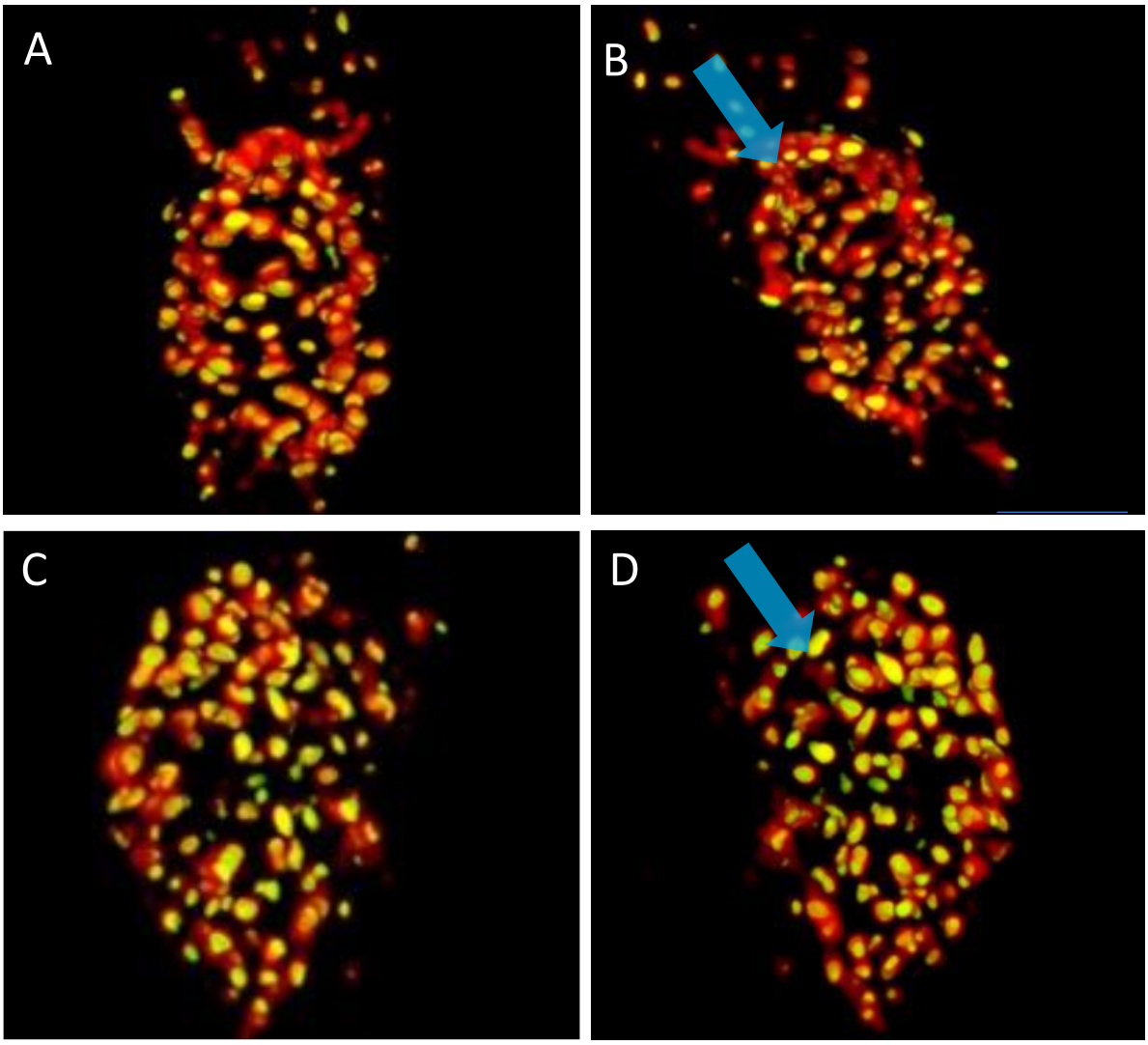

Figure S5.1. Raw nuclei volumes (red, including auto fluorescent tissue) and Hessian DoG segmented nuclei (green) overlay, related to Figure 3. Yellow represents the common pixel coverage between the two volumes. (A) and (B) represent the 3 days post fertilization ventricular outer curvature and inner curvature respectively (C) and (D) represent the 4 days post fertilization ventricular outer curvature and inner curvature respectively. Blue arrows represent inflow region.

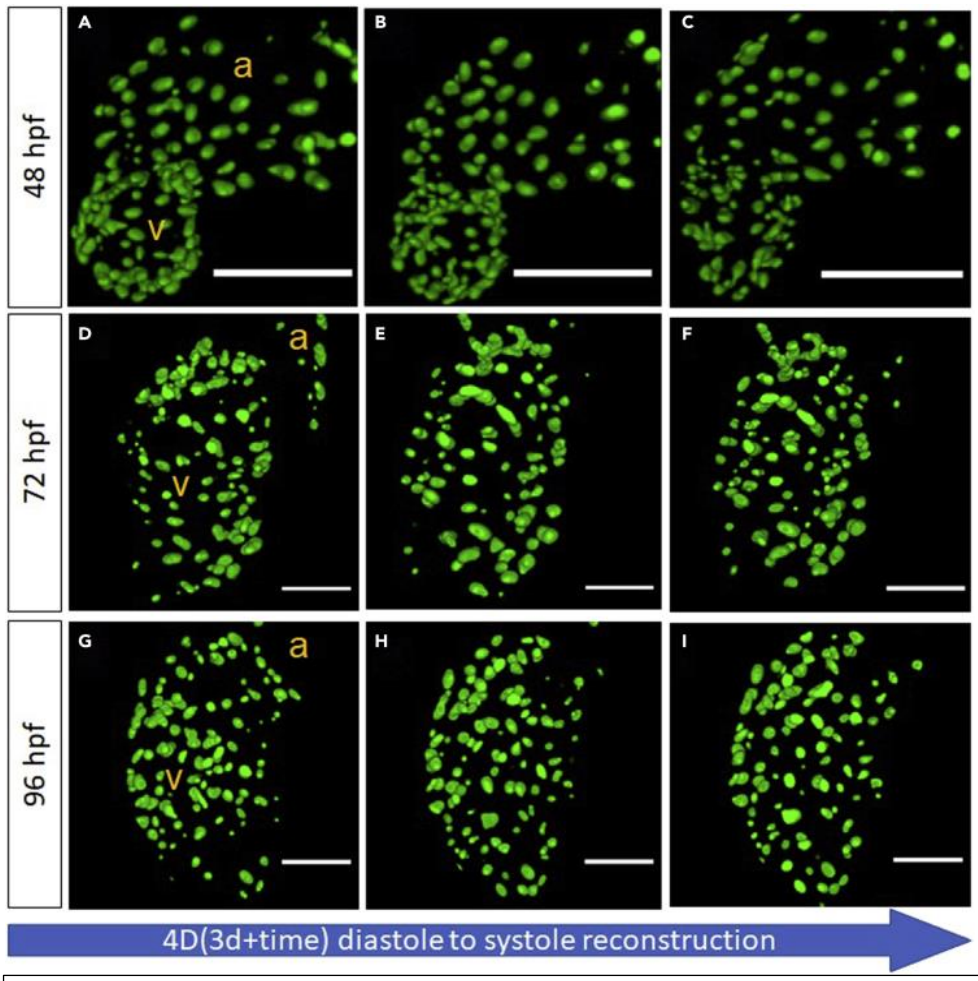

Figure S5.2. Visualizing cmlc:GFPnuc zebrafish ventricular nuclei deformation at distinct developmental stages (48 – 96 h postfertilization), across the cardiac contraction cycle (A–I). The Hessian DoG scale space representation was used for localizing cardiomyocyte nuclei ranging from different sizes, as a result of which we were able to assess ventricular contractility and complex nuclei morphology *in vivo* (scale bar for A-C = 100-micron, scale bar for D-I = 50 micron). A:atrium, v:ventricle.

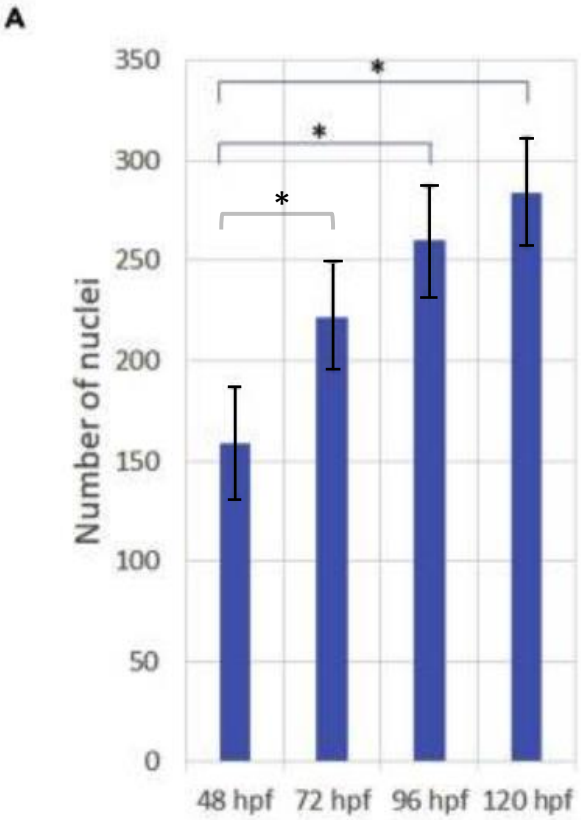

Figure S5.3. Nuclei counting across developmental stages of embryonic zebrafish (A) Nuclei count was observed to rise significantly across valve formation to complete heart maturation, for wild-type transgenic cmlc:GFPnuc zebrafish. Asterisk indicates significant difference with 48 hours post birth stage

Comparison	P – value
48 vs 72 days post fertilization	0.01
48 vs 96 days post fertilization	0.0061
48 vs 120 days post fertilization	<0.0001
72 vs 96 days post fertilization	0.03
72 vs 120 days post fertilization	0.01
96 vs 120 days post fertilization	0.04

Table 5.1. Significance testing values for nuclei counting.

CHAPTER 6

APPLICATION OF 4D LIGHT SHEET IMAGING PIPELINE TO QUANTIFY NUCLEI MORPHOGENESIS AND MECHANICAL DEFORMATION IN EMBRYONIC ZEBRAFISH MYOCARDIUM

6.1 INTRODUCTION

Zebrafish (Danio rero) are emerging as potent vertebrate models for modeling human congenital heart disorders (CHD)[27], [65]–[68]. This is due to numerous attractive traits such as embryonic optical transparency, high fecundity, and ease in genetic or biomechanical modulation for mimicking the human CHD pathophysiology[10]. As a result, zebrafish enable access to phenotypic screening of dynamic biomechanical stimuli such as contractility and blood flow, responsible for modulating heart maturation.

Previously conducted zebrafish studies have observed conserved cardiomyocyte count proportional to atrial/ventricular mass or volume per developmental stage[50], [69]–[71]. Moreover, recent studies suggest cardiomyocyte shape hypertrophy across three distinct ventricular regions—atrioventricular (AV) canal, outer curvature (OC), and inner curvature (IC) regions—apart from distinct atrial cardiomyocyte morphology. In addition, biologists have questioned the implications of cardiac mechano-transduction on enlarged cardiomyocyte morphology in the OC region in front of AV canal, with respect to spherical (isotropic) cardiomyocytes in the IC[64], [69], [72]. However, the ability to observe cardiomyocyte morphogenesis *in vivo* is adversely affected by tissue birefringence, hindering characterization of beforementioned cardiovascular phenotypes. In this regard, automated feature detectors are proving to be an indispensable tool for segmenting cellular volumes without human intervention to avoid gross inconsistencies and produce refined datasets.

Conventionally, invasive sectioning procedures have offered revolutionary insights into aberrant tissue up to the cellular scale. However, histopathological analysis currently suffers from severe limitations, primarily disruption to tissue homeostasis. With respect to these drawbacks, the optical sectioning modality light sheet fluorescence microscopy (LSFM) has proved instrumental in probing dynamic organogenesis several millimeters inside tissue. LSFM has tremendously benefitted embryologists to become cognizant of dynamic phenomena such as mechano-transduction and undifferentiated precursor cell signaling pathways.

However, acquisition of dynamic organogenesis reported by endogenous fluorophores is a challenging task owing to anisotropic contrast across the field of view (FOV). This is due to photon propagation through heterogeneous tissue. Hence, precise orchestration of *in vivo* volumes requires high sensitivity with respect to dynamic tissue motion and differing scales. As a result, optical aberrations often induce redundancy in the imaging sample space, affecting interpretability of feature attributes.

In this study, we have applied scale space feature detector developed in chapter 5 in conjunction with 4D imaging pipeline, to characterize wild-type zebrafish ventricular local deformation and structural phenotypes such as cell surface area.

6.2 MATERIALS AND METHODS

6.2.1 PREPARATION OF ZEBRAFISH

Transgenic zebrafish embryos, specifically Tg(cmlc2:nuc-eGFP) at 3-, 4-, and 5-day post-fertilization (dpf) groups, were employed in this study. These zebrafish embryos express nuclear-enhanced green fluorescent protein (eGFP) under the control of the cardiac myosin light chain 2 promoter, enabling visualization of all differentiated cardiomyocytes. This promoter ensures that the nuclear eGFP serves as a marker for measuring regional cardiac wall deformations. During the early developmental stage examined, typically 3 to 5 dpf, the zebrafish heart consists of only two or three cardiac layers, rendering the cardiac wall relatively thin-walled. The cardiomyocytes themselves act as markers for assessing wall deformations. To inhibit pigmentation, 0.003% w/v phenylthiourea in E3 medium (comprising 10% Hank's solution with full-strength calcium and magnesium) was introduced at 20 hours post-fertilization (hpf). All chemicals utilized in the experiments were obtained from Sigma-Aldrich, and solutions were freshly prepared before each session. For imaging the heart, embryos were anesthetized in 0.05% tricaine and embedded in 0.5% low melting point agarose, chosen for its refractive index similarity to water and biological tissue. Before the agarose solidified, the embryos were carefully transferred to a fluorinated ethylene propylene (FEP) tube and vertically mounted on a stage, ensuring that the heart was aligned with the imaging light path. All zebrafish embryos utilized in the study were bred in the animal care facility and maintained at a temperature of 28°C. The experimental procedures adhered to ethical guidelines and were conducted in compliance

with the UT Arlington Institutional Animal Care & Use Committee (IACUC) guidelines, specifically protocols A17.014 and A17.016.

6.2.2 MULTIDIMENSIONAL LIGHT SHEET SETUP

To capture dynamic images of pulsating zebrafish hearts, 4D LSM setup from chapter 5 was utilized, following methodologies outlined in prior research. Utilizing a 20X water dipping objective with a high numerical aperture (NA = 0.5) helped mitigate spherical aberrations by minimizing differences in refractive indices. Recording was performed using a Hamamatsu ORCA Flash 4.0 sCMOS camera, capturing 150 to 280 overlapping z-slices with a 10 ms exposure time, at fixed 0.65 μm step size. The entire process was orchestrated through customized LABVIEW code from National Instruments. Subsequent processing of the image sequences was carried out using previously established MATLAB code to minimize cardiac phase errors across layers and time steps. Post-acquisition synchronization allowed for the reconstruction of four-dimensional (4D) images, ensuring temporal coherence.

6.2.3 CONTRACTILITY METHODOLOGY [14]

We utilized the segmented, processed, and time synchronized images to reconstruct three-dimensional volumes through time for a cardiac cycle to perform this tracking. We then passed these images through a custom MATLAB (Mathworks) code **(Figure 6**.1) to perform key steps.

The MATLAB code performed following 4 steps.

1.The code compiles images into easily searchable 4D matrices.

2.The code resolves the 4D matrices of segmented images into centers of mass based on high pixel concentration areas for each time step.

3.The user selects three markers to represent our plane for stretch calculations.

4.The code searches through the 4D stack of centers of mass to determine the closest center of mass in the next time step and stores these points in a matrix of position values.

Each stored triplet value is the x, y, and z position of a particular nucleus at a particular time. This format is easily searchable and allows for a multitude of calculations. This code assumes that there can be no erratic motion of the nucleus with a high enough sampling frequency. The location at each time step depends on the prior location. Imaging with a high sampling frequency supply data that meets this assumption requirement. Other works have utilized similar works, including Meijerling et AL. Drawbacks of this method include the requirement for user interaction. To verify that the cell tracking occurs appropriately, the user must analyze each vector to ensure the vector does not violate the small motion assumption. This process can become time-consuming and increases the chance of human error. Subsequent work can expand and refine this cell tracking method to include other parameters, including a probability net for machine learning applications and size and orientation to decrease ambiguity and reduce the user input requirement.

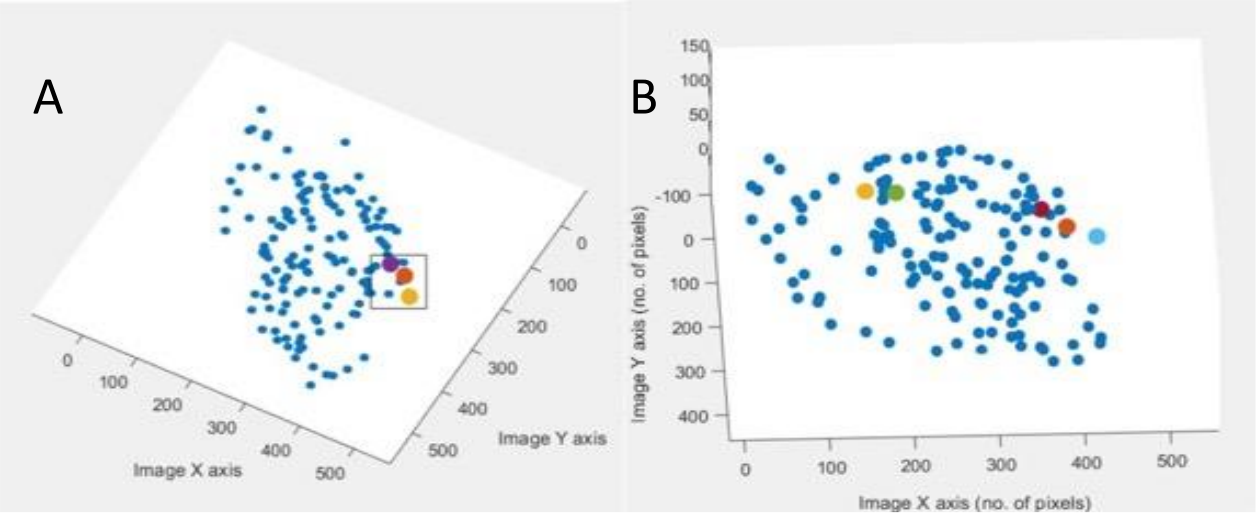

Figure 6.1. Snapshot of 4D nuclei tracking performed using MATLAB (A) 3 dpf ventricular myocardial nuclei volumetric stack reconstructed using MATLAB. Yellow, orange, and purple blobs highlight centers of mass localized for nuclei tracking in the outer curvature (B) 4 dpf ventricle volumetric stack reconstructed using MATLAB. Yellow, green, and purple centers of mass localized for nuclei tracking in the inner curvature. Red, orange, and blue centers of mass localized for nuclei tracking in the outer curvature. A= atrium, V = ventricle (C)) Individual nuclei used for tracking.

6.2.4 STATISTICAL TESTING

For statistical analysis, we performed pairwise comparisons for morphological parameters such surface area and eccentricity to characterize the maturity of the heart (p value = 0.05). We estimated each of these parameters using built in functions in ImageJ (NIH, Bethesda, MD) with n = 15. Additionally, we cleaned the data in excel utilizing Chauvenet's criterion to determine which values were outliers and should be removed. After removing outliers and cleaning the datasets in excel to reduce the chance of error due to our sampling

technique, we compared the data with one-way ANOVA. If we detected a statistically significant difference for any comparison, we performed Tukey's test for multiple comparison of means. Regional differences in area ratio were tested by a one-way ANOVA, with the normality of data tested and confirmed. Tukey's multiple post hoc comparisons was performed when significant differences were detected. Statistical testing was performed in R, with $P < 0.05$ considered as statistically significant.

6.2.5 NUERAL NET ARCHITECTURE

The neural architecture operates on grayscale images through two pathways: the contracting path, which employs convolutions, ReLU activation, and pooling to condense features, and the expansive path, which upscales features using convolution operations. It utilizes a binary cross-entropy loss function and the stochastic gradient descent optimizer for training, executed mainly on an Intel Xeon E5 CPU and NVIDIA Quadro P5000 GPU[73], [74]. Training time per slice is approximately 500 seconds per epoch, with prediction taking about 60 ms per slice.

6.3. RESULTS

6.3.1 ISOLATING INDIVIDUAL CARDIOMYOCYTE NUCLEI IN DYNAMIC ZEBRAFISH VENTRICULAR VOLUMES

Distinguishing fused nuclei boundaries by manual contour segmentation or determining the intensity threshold for distorted nuclei outside the light sheet confocal parameter (focus region) is a complex task due to varying pixel intensities of overlapping nuclei **(Figure 6.2).** Furthermore, autofluorescence and dynamic cardiac motion convolutes lateral and axial imaging planes **(Figure 6.2(i-j)).** To separate nuclei clusters into disjoint regions, we implemented the Hessian Difference of Gaussian (DoG) filter to enhance cell boundaries followed by the watershed algorithm to separate merged boundaries affected by anisotropic contrast. As a result, we were able to successfully quantify nuclei across different scales in a moderately dense cell environment at 48 h postfertilization (hpf**) (Figure 6.2e).** More importantly, integration of the DoG scale space detector with the watershed algorithm enabled us to split longitudinally merged nuclei (Figure 6.1). In this regard, photon travel through heterogeneous tissue and restrictions imposed on resolvable sample depth are prone to induce sample de-focus.

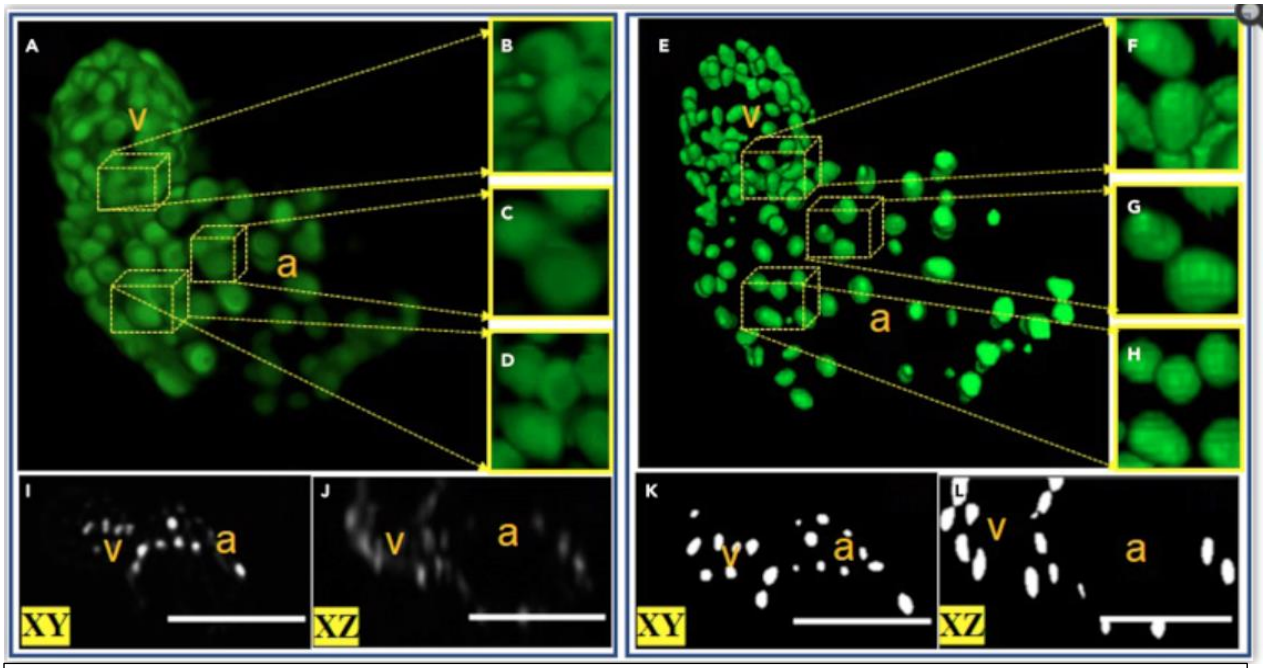

Figure 6.2. (A) 48 h postfertilization zebrafish ventricular volume was reconstructed using light sheet microscopy, (B–D) Zoomed in regions demonstrate fused contours of nuclei, adversely affecting individual nuclei analysis (E) Ventricular volume was processed using the difference of Gaussian (DoG) edge detector in conjunction with the watershed algorithm (I–J) 2D lateral and axial views illustrate tissue birefringence resulting in merging of nuclei longitudinally (K-L) Segmented lateral and axial views. (scale bar for I,J,K,L = 100 microns), (scale bar for D,H = 15 microns), a: atrium, v: ventricle.

6.3.2 QUANTIFICATION OF LOCAL DEFORMATION VIA TRACKING CARDIOMYOCYTE NUCLEI

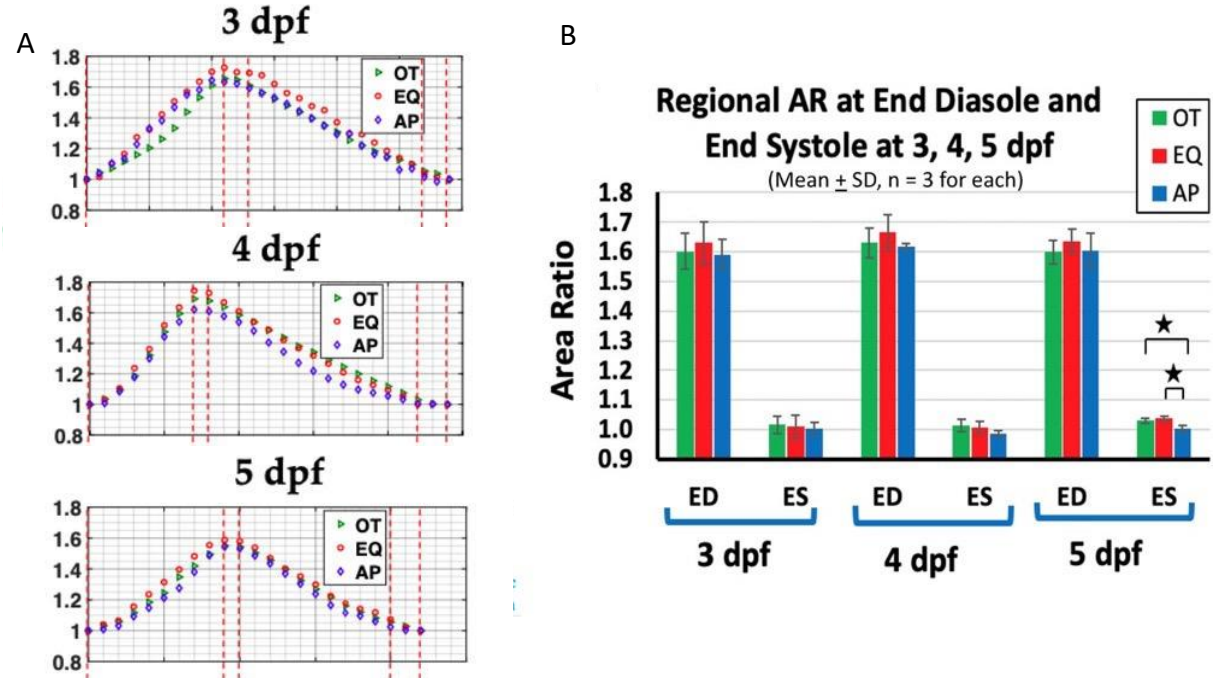

Figure (6.3). Area ratio index calculated by tracking 4D nuclei motion (A) Representative time courses for area ratio (AR) for one cardiac cycle at the outflow (OT), equatorial (EQ), and apex (AP) regions **(Figure S6.1).** The four cardiac cycle phases are indicated with red vertical dashed lines. (B) No statistically significant differences were found among regions and in different dpf groups, except between AP vs EQ and AP vs OT in the 5-dpf group. Statistically significant differences ($P < 0.05$) are denoted by asterisk.

The investigation involved selecting three neighboring nuclei within a triangular region, each with a side length ranging from 15 to 25 μm, from the EQ, AP, and OT regions. The deformation of each triangular region across a cardiac cycle was characterized by tracking the relative movement of markers. (**(Figure (6.1), Figure 6.3a))** illustrates representative

time courses for calculated area ratios (AR) in the three regions at 3-, 4-, and 5-days post-fertilization (dpf). The cardiac cycle phases (filling, isovolumic contraction, ejection, and isovolumic relaxation) are marked by red vertical dashed lines.

(Figure 6.3b) summarizes the results of regional AR at the end-diastolic (ED) and end-systolic (ES) states for the OT, EQ, and AP regions at each timepoint. No significant regional differences in AR were observed for the ED state at 3, 4, and 5 dpf. Analysis of regional AR during the ES state revealed no significant differences, except for a lower value in the AP region at 5 dpf ($P < 0.05$). Furthermore, comparison of AR from the OT region at the ED state among the three dpf groups showed no significant differences. Similarly, no statistical differences were found during the ES state. The values for the EQ and AP regions did not exhibit any significant differences in their respective regional AR during both the ED and ES states across the three dpf time points.

6.3.3 QUANTIFYING ZEBRAFISH VENTRICULAR NUCLEI MORPHOGENESIS ACROSS DEVELOPMENTAL STAGES

For quantifying nuclei surface area, we sampled n = 50 dynamic nuclei from 2 zebrafish samples per day (48-,72-,96 and 120 days post birth) across cardiac cycle. Due to distinct nuclei shapes in localized ventricular regions (smaller, circular nuclei in inner ventricular region near inflow and larger, rod shaped in equatorial. region), we decided to perform statistical testing for nuclei surface area in these two regions respectively, during heart maturation stages. We observed nuclei located near inflow show significantly different

surface areas between 72 vs 96 days post birth stage ($p<0.001$), while there was no significant difference between 48 vs 72 - & 96 vs 120 days post birth. On the other hand, for larger nuclei in the outer ventricular region, we observed significant difference in surface area each day of development from 48 – 96 days post birth (48 vs 72: p-value = 0.04, 72 vs 96: p value = 0.0014, 96 vs 120: p value = 0.3), with nuclei surface area plateauing at 120 days post birth.

A

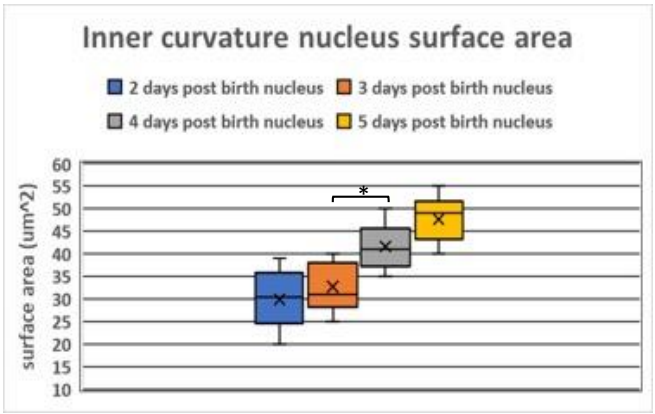

B

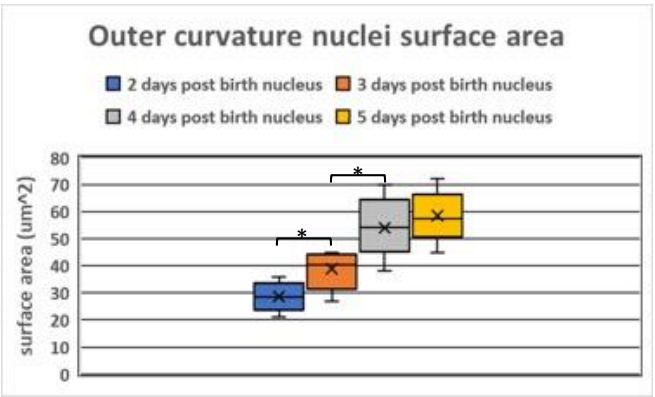

Figure 6.4. (A) Significance testing carried out for nuclei distributed in inner ventricular region near inflow (B) Significance testing carried out for nuclei distributed in outer ventricular region, near equatorial region.

6.3.4 APPLICATION OF HESSIAN FEATURE DETECTOR AS GROUND TRUTH SEGMENTATION PIPELINE FOR NEURAL NET TRAINING

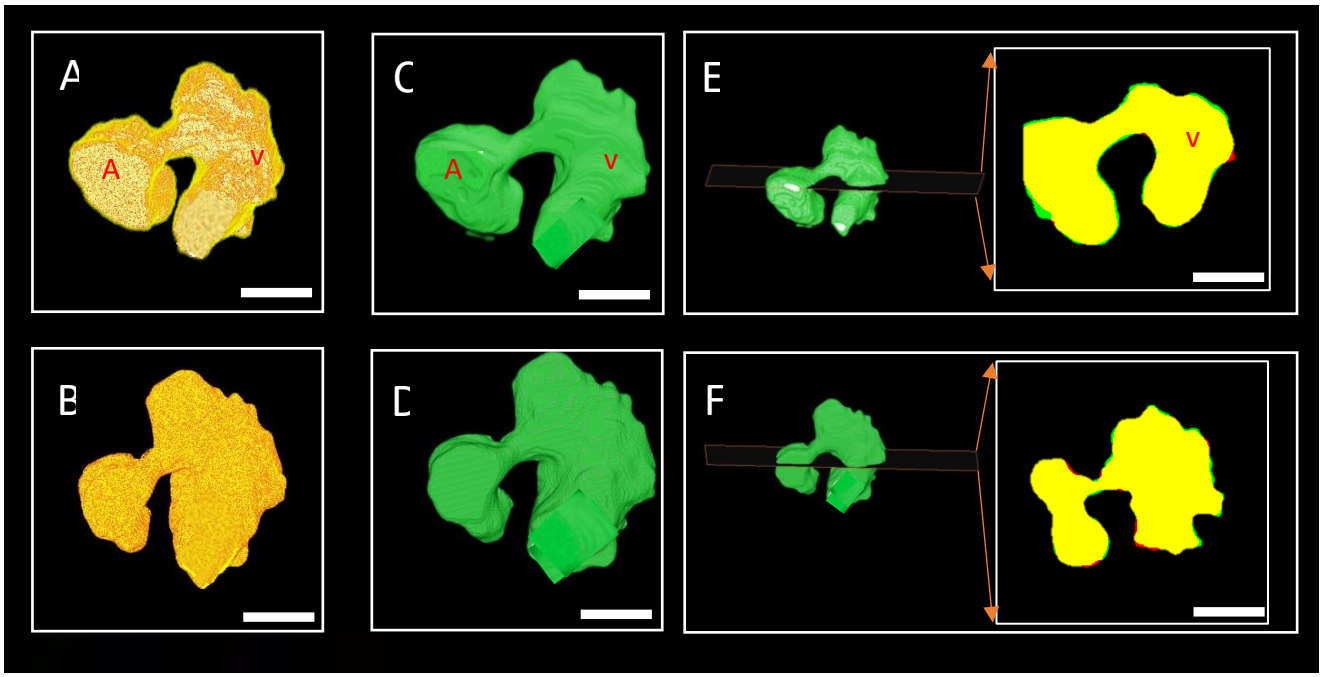

Figure 6.5. Automated three-dimensional volume segmentation using nnU-net. (A) & (B) represent ventricular end systolic and diastolic volumes, delineated by segmenting myocardial muscle fibers in transgenic (cmlc:GFP) zebrafish using Hessian Difference of Gaussian feature detector (C) & (D) represent ventricular end systolic and diastolic volumes produced by neural net, using (A) & (B) as training data. (E&F) represent cross section overlap of ground truth ventricular volume (green) and neural net segmented volume (yellow). Ventricle is denoted by red V, while atrium is denoted by red A. (scale bar = 50 micron)

Although Hessian Difference of Gaussian Feature detector was implemented for automated feature segmentation, the feature detector exhibited drawbacks in the form of need for

adjustment of gaussian blurring kernel weights for objects of difference scales. To overcome this bottleneck, we used the HDoG feature detector to produce training data for a semantic segmentation based neural net (nnU-Net) **(Figure 6.5)**. For this study, we used transgenic zebrafish with green fluorescent protein expressed in ventricular myocardium to segment ventricular lumen. Hence, this enabled us to quantify ventricular volumes in cubic micrometer or nL (Volume was estimated by multiplying total number of slices with voxel step size). Consequently, we observed no significant difference between end systolic volume of (1.5 +/- 0.25) x10^{-1} nL for HDoG volume and (1.45 +/- 0.1) x 10^{-1} nL for the neural net segmented volume (n = 10 ventricles, alpha value = = 0.05) **(Figure 6.6A).** In addition, we observed no significant difference in end diastolic volume of (3 +/- 0.2) x 10^{-1} nL for HDoG segmented volume and (2.9 +/- 0.1) X 10^{-1} nL for neural net segmented volume (**Figure 6.6B)** (n = 10 ventricles, alpha value = = 0.05)**.** Consequently, we were able to establish an automated multidimensional cell acquisition and segmentation pipeline, to quantify discrete cellular phenotypes.

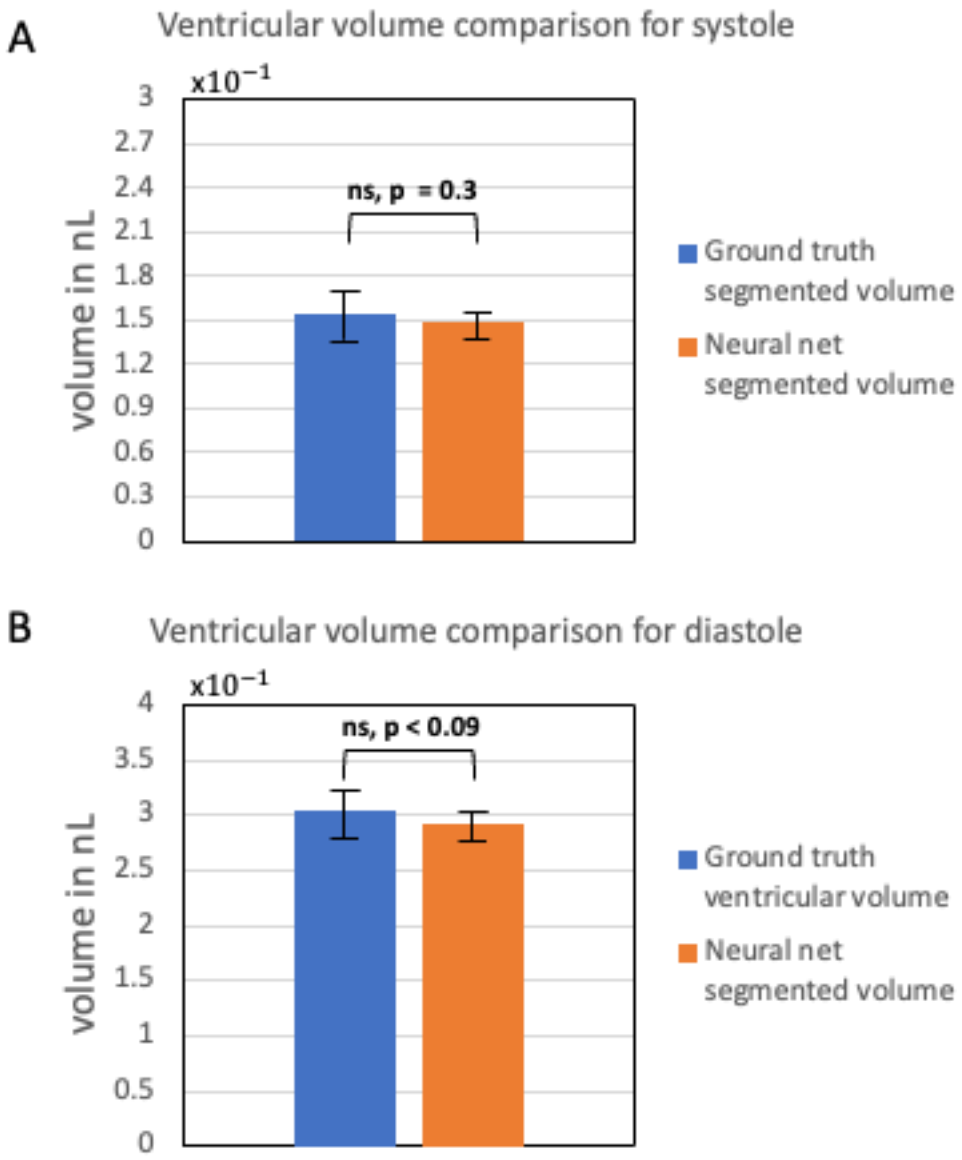

Figure 6.6. Segmentation accuracy evaluation (A) Significance testing carried out for end systolic volume comparison (B) Significance testing carried out for end diastolic volume comparison

6.4 DISCUSSION

Wild-type Tg(*cmlc2:egfp*) zebrafish have been observed to exhibit cuboidal cardiomyocyte morphology in linear heart tube (24 hpf) and IC ventricular myocardium, with respect to elongated cardiomyocytes in the OC. Studies indicate regionally distinct cardiomyocyte phenotypes such as cell count, area, or sphericity are regulated by mechanical stimuli such as contractility or blood flow during heart maturation. This has been validated through the mutation phenotype *half-hearted (haf)* mutation lacking ventricular contractility[28]. The *haf*mutant exhibited elongated cardiomyocytes with increased surface area across different parts of the ventricle including IC, resulting in a distended ventricle. Interestingly, cardiomyocyte count was observed to be consistent between the *haf* mutant and wild-type zebrafish ventricle, suggesting contractility is responsible for moderating the aberrant elongation of cardiomyocytes and not anomalous proliferation. Furthermore, previously performed studies indicate cardiomyocyte number reflects a sigmoidal growth trend, subsequently plateauing at later stages (>96 hpf) thereby signaling specification into the myocardium. In this regard, the proposed feature detector and cell tracking algorithm can prove extremely beneficial for gaining insights into the effects of cardiac contraction on reducing proliferation and its secondary effects on cardiomyocyte morphology.

Our study has the potential to elucidate ventricular development in zebrafish orthologs, and aid cardiac pathophysiology diagnosis or clinical translational of cardiac regeneration for pediatric population. In this regard, nuclear morphology observed in cardiomyocytes isolated from neonatal rat ventricles reports similar cell shape findings, regarding systolic

and diastolic heterogeneous cross-sectional surface areas of nuclei (Bray et al., 2010). Hence, our novel, preclinical study provides exciting avenues to characterize cell count, morphology, and intercellular biomechanical forces in transgenic zebrafish, that are responsible for cardiomyopathy in humans.

6.5 SUPPLEMENTARY FIGURES

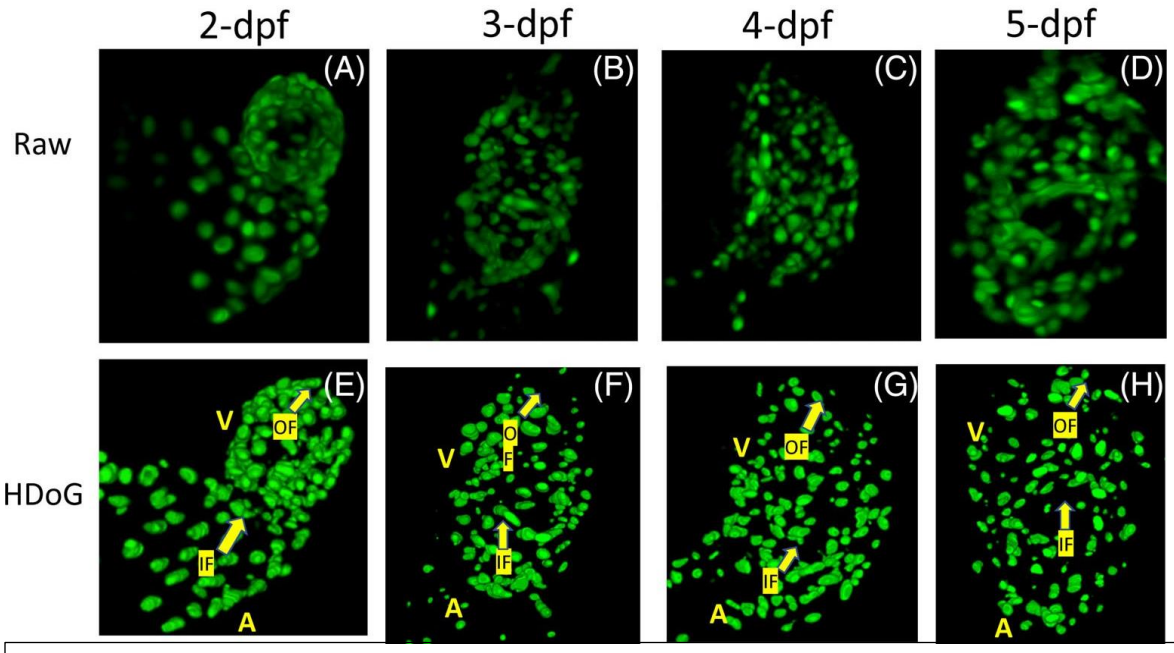

Figure S6.1. Visualizing spatiotemporal dynamics of myocardial cardiomyocyte nuclei from zebrafish at 2, 3, 4, 5 dpf. (A, B, C, D) Volumetric reconstruction of myocardial cardiomyocyte architecture acquired using high magnification water objective lens, enabling higher spatial resolution albeit with tradeoff in field of view. (E, F, G, H) Segmented nuclei volumes using Hessian Difference of Gaussian (HDoG) filter in conjunction with watershed algorithm. A, atrium, IF: inflow through AV valve, OF: outflow through VB valve; V, ventricle. Arrow heads point to the direction of the flow.

CHAPTER 7

CONCLUSION AND FUTURE PROGRESS

7.1.CONCLUSION

Evaluating structural and functional biomarkers in preclinical research models is crucial for comprehending the pathophysiology of human disorders and discovering new treatments. While examining fixed tissue sections and histology has provided groundbreaking insights into tissue architecture, the destructive nature of the technique and thickness of physical sections restricts investigation of cellular dynamics. Moreover, commercial upright or inverted microscopes are inherently unable to acquire multidimensional volumes of histology sections due to tissue opaqueness. Consequently**,** the dynamic interplay of molecular signaling pathways leading to diverse clinical pathologies necessitate robust *in vivo* modeling platforms to identify dynamic biomarkers. Hence, precise mutagenesis models in conjunction with *in vivo* imaging platforms are pivotal for effective clinical translation of pharmaceutical compounds.

Traditionally larger animals like canines, pigs, or sheep have been instrumental in studying human disease tissue remodeling and drug screening due to their molecular and biomechanical similarities. However, their use presents challenges, including high costs, lengthy breeding cycles, and the need for specialized surgical skills, hindering study throughput and clinical reproducibility. In addition, the absence of robust gene editing tools limits their utility in understanding developmental signaling pathways. However, more importantly, these animal models require physical tissue sections to probe cellular mutagenesis.

On the other hand, zebrafish have emerged as highly efficient and genetically manipulable models to replicate developmental disease progression. Zebrafish possess genes analogous to mammals, allowing for mutagenesis studies. Their high breeding capacity, ease in genetic modification, and similar drug responses to humans make them advantageous as non-invasive preclinical animal models. In this regard, Optical sectioning tomography has significantly advanced the non-invasive, quantitative modeling of tissue mutagenesis and embryonic zebrafish development. Fluorescence imaging, particularly Light Sheet Microscopy has met the biologist's fundamental need to explore anatomical irregularities or metabolic disruptions directly in living organisms. However, Light Sheet Microscopes are highly reliant on high NA/magnification optics for micrometer scale resolution, thereby intrinsically suffering from low penetration depth and limiting modulation of light sheet thickness.

To overcome unmet limitations, AIM 1 covers development of a new generation of LSM by integration of maximum likelihood estimation (MLE) based sub voxel LSM and Axially Sweeping LSM modalities. Consequently, we achieved *in toto* sampling of large animal organs (up to 1 cm) while maintaining micron scale resolution using a very low magnification (2x) lens. In addition, we quantified isotropic micron scale 3D pixel resolution across 4.5-millimeter field-of-view, thereby decoupling fundamental limitations of lens configuration on resolution and penetration depth. Hence, we hypothesize Maximum Likelihood Estimation (MLE) based Axially Sweeping Light Sheet Microscopy (AS-LSM) is a bona-fide milli-meter penetration depth, cellular resolution capable, three-

dimensional imaging toolbox. Moreover, we integrated optical tissue clearing with MLE based Axially Sweeping Light Sheet Microscopy to overcome destructive physical tissue sectioning, enabling a non-invasive, preclinical in *situ/toto* imaging platform for meso scale (millimeters) specimens.

With respect to multidimensional tracking of cellular scale objects at millisecond camera frame rates for specimens less than 1 millimeter, we have also implemented a non-gated, 4D (3D+time) Light Sheet microscope in AIM 2. In addition, a feature detector was integrated with the imaging pipeline, to enable automated cell localization and tracking in AIM 2. Consequently, the 4D (3D+time) Light Sheet Microscope in conjunction with feature detector developed in AIM 2, were used to successfully localize individual cardiomyocyte nuclei (5-10 microns) undergoing rapid translation at camera frame rates ~ 30-50 milliseconds. Consequently, we successfully characterized dynamic zebrafish ventricular contractility, along with cardiomyocyte cell count and surface areas from heart valve formation to heart maturation stages in AIM 3. Thus, creating a multidimensional imaging pipeline in conjunction with transgenic zebrafish fills niche in translational cardiac research, for an *in vivo* preclinical, cell analysis platform. In this regard, transgenic zebrafish with our imaging platform can be used for evaluating drug candidates during preclinical pharmaceutical toxicity screening or phenotype-/genotyping of molecular disease disruptors with high specificity.

7.2. POTENTIAL RESEARCH TOPICS FOR FUTURE STUDIES

We successfully demonstrated tissue optical transparency for whole mice organs, using Benzyl Benzoate refractive index matching protocol. However future progress outside scope of this thesis revolves around integration of cell specific staining while rendering whole organs transparent, to enable non-invasive, cellular scale phenotyping of meso scale specimens. In addition, we successfully achieved micron scale resolution across millimeter penetration depth using MLE based Axially Sweeping Microscopy using a very low NA (0.2 NA). Integration of higher NA (>0.5 NA) optics in the MLE based Axially sweeping microscope, demonstrates potential to achieve sub-micron spatial resolution while maintaining centimeter distance light sheet refocus. Lastly, we successfully implemented an *in vivo* Light Sheet imaging platform to track dynamic heart volume and micron scale cells undergoing movement at millisecond frame rates in wild-type (non-aberrant) zebrafish, at discrete time points of heart development. Consequently, the *in vivo* imaging platform demonstrates potential to enable multidimensional quantification of disease specific mutagenesis in transgenic zebrafish, from single cell developmental stage to complete heart development.

REFERENCES

[1] S. Daetwyler and J. Huisken, “Fast Fluorescence Microscopy with Light Sheets,” *The Biological Bulletin*, vol. 231, no. 1, pp. 14–25, 2016, doi: 10.1086/689588.

[2] O. E. Olarte, J. Andilla, E. J. Gualda, and P. Loza-Alvarez, “Light-sheet microscopy: a tutorial,” *Adv. Opt. Photon.*, vol. 10, no. 1, pp. 111–179, Mar. 2018, doi: 10.1364/AOP.10.000111.

[3] T. Teranikar, J. Lim, T. Ijaseun, and J. Lee, “Development of Planar Illumination Strategies for Solving Mysteries in the Sub-Cellular Realm,” *International Journal of Molecular Sciences*, vol. 23, no. 3, 2022, doi: 10.3390/ijms23031643.

[4] T. Teranikar *et al.*, “Correcting anisotropic intensity in light sheet images using dehazing and image morphology,” *APL Bioeng*, vol. 4, no. 3, pp. 036103–036103, Jul. 2020, doi: 10.1063/1.5144613.

[5] Y. Rivenson, K. de Haan, W. D. Wallace, and A. Ozcan, “Emerging Advances to Transform Histopathology Using Virtual Staining,” *BME Frontiers*, vol. 2020, p. 9647163, Aug. 2020, doi: 10.34133/2020/9647163.

[6] A. Lahiani, E. Klaiman, and O. Grimm, “Enabling Histopathological Annotations on Immunofluorescent Images through Virtualization of Hematoxylin and Eosin,” *J Pathol Inform*, vol. 9, pp. 1–1, Feb. 2018, doi: 10.4103/jpi.jpi_61_17.

[7] T. Teranikar *et al.*, “Scale space detector for analyzing spatiotemporal ventricular contractility and nuclear morphogenesis in zebrafish,” *iScience*, vol. 25, no. 9, p. 104876, Sep. 2022, doi: 10.1016/j.isci.2022.104876.

[8] P. Fei *et al.*, “Cardiac Light-Sheet Fluorescent Microscopy for Multi-Scale and Rapid Imaging of Architecture and Function,” *Scientific Reports*, vol. 6, no. 1, p. 22489, Mar. 2016, doi: 10.1038/srep22489.

[9] C. P. Choe *et al.*, “Transgenic fluorescent zebrafish lines that have revolutionized biomedical research,” *Laboratory Animal Research*, vol. 37, no. 1, p. 26, Sep. 2021, doi: 10.1186/s42826-021-00103-2.

[10] T. Teranikar, P. Nguyen, and J. Lee, “Biomechanics of cardiac development in zebrafish model,” *Current Opinion in Biomedical Engineering*, vol. 27, p. 100459, Sep. 2023, doi: 10.1016/j.cobme.2023.100459.

[11] K. M. Dean, P. Roudot, E. S. Welf, G. Danuser, and R. Fiolka, “Deconvolution-free Subcellular Imaging with Axially Swept Light Sheet Microscopy,” *Biophys J*, vol. 108, no. 12, pp. 2807–2815, Jun. 2015, doi: 10.1016/j.bpj.2015.05.013.

[12] K. Chatterjee, F. W. Pratiwi, F. C. M. Wu, P. Chen, and B.-C. Chen, “Recent Progress in Light Sheet Microscopy for Biological Applications,” *Appl Spectrosc*, vol. 72, no. 8, pp. 1137–1169, Aug. 2018, doi: 10.1177/0003702818778851.

[13] S. Daetwyler and R. P. Fiolka, “Light-sheets and smart microscopy, an exciting future is dawning,” *Communications Biology*, vol. 6, no. 1, p. 502, May 2023, doi: 10.1038/s42003-023-04857-4.

[14] N. Salehin, T. Teranikar, J. Lee, and C.-J. Chuong, “Ventricular anisotropic deformation and contractile function of the developing heart of zebrafish in vivo,” *Developmental Dynamics*, vol. n/a, no. n/a, doi: https://doi.org/10.1002/dvdy.536.

[15] N. Salehin, C. Villarreal, T. Teranikar, B. Dubansky, J. Lee, and C.-J. Chuong, “Assessing Pressure–Volume Relationship in Developing Heart of Zebrafish In-Vivo,” *Annals of Biomedical Engineering*, vol. 49, no. 9, pp. 2080–2093, Sep. 2021, doi: 10.1007/s10439-021-02731-0.

[16] T. Teranikar *et al.*, “Feature Detection to Segment Cardiomyocyte Nuclei for Investigating Cardiac Contractility,” *bioRxiv*, p. 2021.03.03.433810, Jan. 2021, doi: 10.1101/2021.03.03.433810.

[17] T. Chakraborty *et al.*, “Light-sheet microscopy of cleared tissues with isotropic, subcellular resolution,” *Nature Methods*, vol. 16, no. 11, pp. 1109–1113, Nov. 2019, doi: 10.1038/s41592-019-0615-4.

[18] K. M. Dean, P. Roudot, C. R. Reis, E. S. Welf, M. Mettlen, and R. Fiolka, “Diagonally Scanned Light-Sheet Microscopy for Fast Volumetric Imaging of Adherent Cells,” *Biophysical Journal*, vol. 110, no. 6, pp. 1456–1465, Mar. 2016, doi: 10.1016/j.bpj.2016.01.029.

[19] Huisken Jan, Swoger Jim, Del Bene Filippo, Wittbrodt Joachim, and Stelzer Ernst H. K., “Optical Sectioning Deep Inside Live Embryos by Selective Plane Illumination Microscopy,” *Science*, vol. 305, no. 5686, pp. 1007–1009, Aug. 2004, doi: 10.1126/science.1100035.

[20] T. Yu, J. Zhu, D. Li, and D. Zhu, “Physical and chemical mechanisms of tissue optical clearing,” *iScience*, vol. 24, no. 3, p. 102178, Mar. 2021, doi: 10.1016/j.isci.2021.102178.

[21] D. Jing *et al.*, “Tissue clearing of both hard and soft tissue organs with the PEGASOS method,” *Cell Research*, vol. 28, no. 8, pp. 803–818, Aug. 2018, doi: 10.1038/s41422-018-0049-z.

[22] E. H. K. Stelzer *et al.*, “Light sheet fluorescence microscopy,” *Nature Reviews Methods Primers*, vol. 1, no. 1, p. 73, Nov. 2021, doi: 10.1038/s43586-021-00069-4.

[23] B.-J. Chang, K. M. Dean, and R. Fiolka, “Systematic and quantitative comparison of lattice and Gaussian light-sheets,” *Opt. Express*, vol. 28, no. 18, pp. 27052–27077, Aug. 2020, doi: 10.1364/OE.400164.

[24] Peng Fei *et al.*, “Subvoxel light-sheet microscopy for high-resolution high-throughput volumetric imaging of large biomedical specimens,” *Advanced Photonics*, vol. 1, no. 1, p. 016002, Jan. 2019, doi: 10.1117/1.AP.1.1.016002.

[25] O. Graydon, “Subvoxel light-sheet microscopy,” *Nature Photonics*, vol. 13, no. 3, pp. 139–139, Mar. 2019, doi: 10.1038/s41566-019-0384-8.

[26] G. Bowley *et al.*, “Zebrafish as a tractable model of human cardiovascular disease,” *British Journal of Pharmacology*, vol. 179, no. 5, pp. 900–917, Mar. 2022, doi: 10.1111/bph.15473.

[27] M. Adhish and I. Manjubala, “Effectiveness of zebrafish models in understanding human diseases—A review of models,” *Heliyon*, 2023.

[28] D. Kula-Alwar, M. S. Marber, S. M. Hughes, and Y. Hinits, “Mef2c factors are required for early but not late addition of cardiomyocytes to the ventricle,” *Developmental Biology*, vol. 470, pp. 95–107, Feb. 2021, doi: 10.1016/j.ydbio.2020.11.008.

[29] T. A. Teranikar, N. Salehin, C.-J. Chuong, and J. Lee, “Automated 4-D myocardial nuclei segmentation method to quantify cardiac contractility for understanding Notch signaling during development (Conference Presentation),” presented at the Imaging, Manipulation, and Analysis of Biomolecules, Cells, and Tissues XVIII, SPIE, 2020, p. 112431M.

[30] R. M. Power and J. Huisken, “A guide to light-sheet fluorescence microscopy for multiscale imaging,” *Nature Methods*, vol. 14, no. 4, pp. 360–373, Apr. 2017, doi: 10.1038/nmeth.4224.

[31] E. J. Botcherby, R. Juskaitis, M. J. Booth, and T. Wilson, “Aberration-free optical refocusing in high numerical aperture microscopy,” *Opt. Lett.*, vol. 32, no. 14, pp. 2007–2009, Jul. 2007, doi: 10.1364/OL.32.002007.

[32] S. V. Avilov, “Navigating across multi-dimensional space of tissue clearing parameters,” *Methods and Applications in Fluorescence*, vol. 9, no. 2, p. 022001, Mar. 2021, doi: 10.1088/2050-6120/abe6fb.

[33] S. Lee, S. Yun, J.-H. Nam, C. S. Won, and S.-W. Jung, “A review on dark channel prior based image dehazing algorithms,” *EURASIP Journal on Image and Video Processing*, vol. 2016, no. 1, p. 4, Jan. 2016, doi: 10.1186/s13640-016-0104-y.

[34] K. He, J. Sun, and X. Tang, “Single Image Haze Removal Using Dark Channel Prior,” *IEEE Transactions on Pattern Analysis and Machine Intelligence*, vol. 33, no. 12, pp. 2341–2353, 2011, doi: 10.1109/TPAMI.2010.168.

[35] S. Johnsen, “Hide and Seek in the Open Sea: Pelagic Camouflage and Visual Countermeasures,” *Annu. Rev. Mar. Sci.*, vol. 6, no. 1, pp. 369–392, Jan. 2014, doi: 10.1146/annurev-marine-010213-135018.

[36] S. Johnsen and E. Widder, “Ultraviolet absorption in transparent zooplankton and its implications for depth distribution and visual predation,” *Marine Biology*, vol. 138, pp. 717–730, 2001.

[37] S. Johnsen and E. A. Widder, “The Physical Basis of Transparency in Biological Tissue: Ultrastructure and the Minimization of Light Scattering,” *Journal of Theoretical Biology*, vol. 199, no. 2, pp. 181–198, Jul. 1999, doi: 10.1006/jtbi.1999.0948.

[38] X. Xie *et al.*, “Extended depth-resolved imaging through a thin scattering medium with PSF manipulation,” *Scientific Reports*, vol. 8, no. 1, p. 4585, Mar. 2018, doi: 10.1038/s41598-018-22966-7.

[39] R. R. Jones, D. C. Hooper, L. Zhang, D. Wolverson, and V. K. Valev, “Raman Techniques: Fundamentals and Frontiers,” *Nanoscale Research Letters*, vol. 14, no. 1, p. 231, Jul. 2019, doi: 10.1186/s11671-019-3039-2.

[40] N. T. M, K. Seemakurthy, A. N. Rajagopalan, N. Vedachalam, and R. Raju, “Color Restoration in Turbid Medium,” in *Proceedings of the Tenth Indian Conference on*

Computer Vision, Graphics and Image Processing, in ICVGIP '16. New York, NY, USA: Association for Computing Machinery, 2016. doi: 10.1145/3009977.3010028.
[41] M. Bass *et al.*, *Handbook of Optics, 5 Volumes*. 2010.
[42] V. Bolón-Canedo, N. Sánchez-Maroño, and A. Alonso-Betanzos, "A review of feature selection methods on synthetic data," *Knowledge and Information Systems*, vol. 34, no. 3, pp. 483–519, Mar. 2013, doi: 10.1007/s10115-012-0487-8.
[43] R. Torres and R. L. Judson-Torres, "Research Techniques Made Simple: Feature Selection for Biomarker Discovery," *Journal of Investigative Dermatology*, vol. 139, no. 10, pp. 2068-2074.e1, Oct. 2019, doi: 10.1016/j.jid.2019.07.682.
[44] T. Teranikar *et al.*, "Feature Detection to Segment Cardiomyocyte Nuclei for Investigating Cardiac Contractility," *bioRxiv*, 2021, doi: 10.1101/2021.03.03.433810.
[45] M. M. El-gayar, H. Soliman, and N. meky, "A comparative study of image low level feature extraction algorithms," *Egyptian Informatics Journal*, vol. 14, no. 2, pp. 175–181, Jul. 2013, doi: 10.1016/j.eij.2013.06.003.
[46] M. M. Sahu, "Application of Feature Extraction Technique : A Review," 2015. [Online]. Available: https://api.semanticscholar.org/CorpusID:8572688
[47] E. de Pater *et al.*, "Distinct phases of cardiomyocyte differentiation regulate growth of the zebrafish heart," *Development*, vol. 136, no. 10, pp. 1633–1641, May 2009, doi: 10.1242/dev.030924.
[48] J. Bakkers, "Zebrafish as a model to study cardiac development and human cardiac disease," *Cardiovascular Research*, vol. 91, no. 2, pp. 279–288, Jul. 2011, doi: 10.1093/cvr/cvr098.
[49] J. M. González-Rosa *et al.*, "Myocardial Polyploidization Creates a Barrier to Heart Regeneration in Zebrafish," *Developmental Cell*, vol. 44, no. 4, pp. 433-446.e7, Feb. 2018, doi: 10.1016/j.devcel.2018.01.021.
[50] J. G. Bensley, R. De Matteo, R. Harding, and M. J. Black, "Three-dimensional direct measurement of cardiomyocyte volume, nuclearity, and ploidy in thick histological sections," *Scientific Reports*, vol. 6, no. 1, p. 23756, Apr. 2016, doi: 10.1038/srep23756.
[51] J. J. Hsu *et al.*, "Contractile and hemodynamic forces coordinate Notch1b-mediated outflow tract valve formation," *JCI Insight*, vol. 5, no. 10, p. e124460, Apr. 2019, doi: 10.1172/jci.insight.124460.
[52] V. Vedula, J. Lee, H. Xu, C.-C. J. Kuo, T. K. Hsiai, and A. L. Marsden, "A method to quantify mechanobiologic forces during zebrafish cardiac development using 4-D light sheet imaging and computational modeling," *PLOS Computational Biology*, vol. 13, no. 10, p. e1005828, Oct. 2017, doi: 10.1371/journal.pcbi.1005828.
[53] M. Mickoleit *et al.*, "High-resolution reconstruction of the beating zebrafish heart," *Nature Methods*, vol. 11, no. 9, pp. 919–922, Sep. 2014, doi: 10.1038/nmeth.3037.
[54] Q. Cao, L. Qingge, and P. Yang, "Performance Analysis of Otsu-Based Thresholding Algorithms: A Comparative Study," *Journal of Sensors*, vol. 2021, p. 4896853, Oct. 2021, doi: 10.1155/2021/4896853.
[55] S. Beucher and C. Mathmatique, "The Watershed Transformation Applied To Image Segmentation," *Scanning. Microsc.*, vol. 6, Jul. 2000.

[56] C. F. Koyuncu, S. Arslan, I. Durmaz, R. Cetin-Atalay, and C. Gunduz-Demir, "Smart Markers for Watershed-Based Cell Segmentation," *PLOS ONE*, vol. 7, no. 11, p. e48664, Nov. 2012, doi: 10.1371/journal.pone.0048664.

[57] B. P. Marsh, N. Chada, R. R. Sanganna Gari, K. P. Sigdel, and G. M. King, "The Hessian Blob Algorithm: Precise Particle Detection in Atomic Force Microscopy Imagery," *Scientific Reports*, vol. 8, no. 1, p. 978, Jan. 2018, doi: 10.1038/s41598-018-19379-x.

[58] R. Bhavna, K. Uriu, G. Valentin, J.-Y. Tinevez, and A. C. Oates, "Correction: Object Segmentation and Ground Truth in 3D Embryonic Imaging," *PLOS ONE*, vol. 11, no. 8, p. e0161550, Aug. 2016, doi: 10.1371/journal.pone.0161550.

[59] T. Lindeberg, "Scale Selection Properties of Generalized Scale-Space Interest Point Detectors," *Journal of Mathematical Imaging and Vision*, vol. 46, no. 2, pp. 177–210, Jun. 2013, doi: 10.1007/s10851-012-0378-3.

[60] T. Lindeberg, "Detecting salient blob-like image structures and their scales with a scale-space primal sketch: A method for focus-of-attention," *International Journal of Computer Vision*, vol. 11, no. 3, pp. 283–318, Dec. 1993, doi: 10.1007/BF01469346.

[61] A. P. Witkin, "Scale-Space Filtering," in *International Joint Conference on Artificial Intelligence*, 1983. [Online]. Available: https://api.semanticscholar.org/CorpusID:7096897

[62] X. Yin, B. W.-H. Ng, J. He, Y. Zhang, and D. Abbott, "Accurate Image Analysis of the Retina Using Hessian Matrix and Binarisation of Thresholded Entropy with Application of Texture Mapping," *PLOS ONE*, vol. 9, no. 4, p. e95943, Apr. 2014, doi: 10.1371/journal.pone.0095943.

[63] C. J. Chuong, M. S. Sacks, G. Templeton, F. Schwiep, and R. L. Johnson, "Regional deformation and contractile function in canine right ventricular free wall," *American Journal of Physiology-Heart and Circulatory Physiology*, vol. 260, no. 4, pp. H1224–H1235, Apr. 1991, doi: 10.1152/ajpheart.1991.260.4.H1224.

[64] G. I. Miura and D. Yelon, "Chapter 7 - A Guide to Analysis of Cardiac Phenotypes in the Zebrafish Embryo," in *Methods in Cell Biology*, vol. 101, H. W. Detrich, M. Westerfield, and L. I. Zon, Eds., Academic Press, 2011, pp. 161–180. doi: 10.1016/B978-0-12-387036-0.00007-4.

[65] Y. Ding, H. Bu, and X. Xu, "Modeling Inherited Cardiomyopathies in Adult Zebrafish for Precision Medicine," *Front Physiol*, vol. 11, pp. 599244–599244, Nov. 2020, doi: 10.3389/fphys.2020.599244.

[66] P. Giardoglou and D. Beis, "On Zebrafish Disease Models and Matters of the Heart," *Biomedicines*, vol. 7, no. 1, 2019, doi: 10.3390/biomedicines7010015.

[67] P. Gut, S. Reischauer, D. Y. R. Stainier, and R. Arnaout, "Little Fish, Big Data: Zebrafish as a Model for Cardiovascular and Metabolic Disease," *Physiological Reviews*, vol. 97, no. 3, pp. 889–938, 2017, doi: 10.1152/physrev.00038.2016.

[68] C. Rödel and S. Abdelilah-Seyfried, "A zebrafish toolbox for biomechanical signaling in cardiovascular development and disease," *Current Opinion in Hematology*, vol. Publish Ahead of Print, Mar. 2021, doi: 10.1097/MOH.0000000000000648.

[69] H. J. Auman, H. Coleman, H. E. Riley, F. Olale, H.-J. Tsai, and D. Yelon, "Functional Modulation of Cardiac Form through Regionally Confined Cell Shape Changes," *PLOS Biology*, vol. 5, no. 3, p. e53, Feb. 2007, doi: 10.1371/journal.pbio.0050053.

[70] M.-A. P. Bray, W. J. Adams, N. A. Geisse, A. W. Feinberg, S. P. Sheehy, and K. K. Parker, "Nuclear morphology and deformation in engineered cardiac myocytes and tissues," *Biomaterials*, vol. 31, no. 19, pp. 5143–5150, Jul. 2010, doi: 10.1016/j.biomaterials.2010.03.028.

[71] W.-Y. Choi *et al.*, "In vivo monitoring of cardiomyocyte proliferation to identify chemical modifiers of heart regeneration," *Development*, vol. 140, no. 3, pp. 660–666, Feb. 2013, doi: 10.1242/dev.088526.

[72] S. A. Rafferty and T. A. Quinn, "A beginner's guide to understanding and implementing the genetic modification of zebrafish," *Progress in Biophysics and Molecular Biology*, vol. 138, pp. 3–19, Oct. 2018, doi: 10.1016/j.pbiomolbio.2018.07.005.

[73] B. Zhang, K. E. Pas, T. Ijaseun, H. Cao, P. Fei, and J. Lee, "Automatic segmentation and cardiac mechanics analysis of evolving zebrafish using deep learning," *Frontiers in cardiovascular medicine*, vol. 8, p. 675291, 2021.

[74] F. Isensee, P. F. Jaeger, S. A. A. Kohl, J. Petersen, and K. H. Maier-Hein, "nnU-Net: a self-configuring method for deep learning-based biomedical image segmentation," *Nature Methods*, vol. 18, no. 2, pp. 203–211, Feb. 2021, doi: 10.1038/s41592-020-01008-z.